AFRL-SN-HS-TR- 2002-020

SELECTED AREA EPITAXY APPLIED TO OPTICAL CROSS POINT SWITCH TECHNOLOGY

University of Southern California
Professor P. Daniel Dapkus
Department of EE-EP
University Park – VHE 310
Los Angeles CA 90089-0243

FINAL REPORT: December 1996 – October 2000

APPROVED FOR PUBLIC RELEASE

AIR FORCE RESEARCH LABORATORY
Sensors Directorate
80 Scott Dr
Hanscom AFB MA 01731-2909

20020905 037

TECHNICAL REPORT

Title: Selected Area Epitaxy Applied to Optical Cross Point Switch Technology

PUBLICATION REVIEW

This report has been reviewed and is approved for publication:

APPROVED:

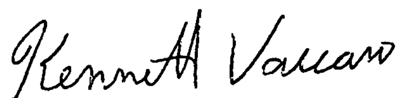

KENNETH VACCARO
AFRL/SNHC
Optoelectronic Technology Branch
Electromagnetics Technology Division

APPROVED:

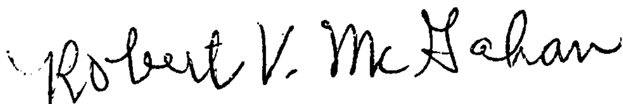

ROBERT V. McGAHAN
Technical Advisor
Electromagnetics Technology Division

REPORT DOCUMENTATION PAGE

Form Approved
OMB No. 0704-0188

Public reporting burden for this collection of information is estimated to average 1 hour per response, including the time for reviewing instructions, searching existing data sources, gathering and maintaining the data needed, and completing and reviewing the collection of information. Send comments regarding this burden estimate or any other aspect of this collection of information, including suggestions for reducing this burden, to Washington Headquarters Services, Directorate for Information Operations and Reports, 1215 Jefferson Davis Highway, Suite 1204, Arlington, VA 22202-4302, and to the Office of Management and Budget, Paperwork Reduction Project (0704-0188), Washington, DC 20503.

1. AGENCY USE ONLY *(Leave blank)*	2. REPORT DATE	3. REPORT TYPE AND DATES COVERED
	16 Nov 2001	FINAL 19 Dec 1996 - 20 Oct 2000

4. TITLE AND SUBTITLE
Selected Area Epitaxy Applied to Optical Cross Point Switch Technology

5. FUNDING NUMBERS
C - F19628-97-C-0012
PE - 62702F
PR - E-7-7032
PROJ - C512
TA - AR WU - 07
ACCESSION NO. - DF479943

6. AUTHOR(S)
P. Daniel Dapkus

7. PERFORMING ORGANIZATION NAME(S) AND ADDRESS(ES)
University of Southern California
Department of Contracts and Grants
837 West 36th Place, STO-330
University Park
Los Angeles, CA 90089-1147

8. PERFORMING ORGANIZATION REPORT NUMBER

9. SPONSORING/MONITORING AGENCY NAME(S) AND ADDRESS(ES)
Kenneth Vaccaro
AFRL/SNHC
80 Scott Drive
Hanscom AFB, MA 01731-2909

10. SPONSORING/MONITORING AGENCY REPORT NUMBER

11. SUPPLEMENTARY NOTES

12a. DISTRIBUTION AVAILABILITY STATEMENT
Approved for public release; distribution unlimited.

12b. DISTRIBUTION CODE
a

13. ABSTRACT *(Maximum 200 words)*
A program of research to develop technology for WDM switching technology is described. The initial approach was to involve the use of selective area epitaxy to fabricate an amplifier based monolithic switching platform. Significant progress was made towards that goal. During the course of the program, however, an opportunity to exploit new approaches with improved characteristics was conceived and the program goals shifted in that direction. The research involves the exploration of heterogeneous integration techniques for the realization of microresonator-based switches. The basic technology approach was demonstrated in passive microresonator filters and then applied to the demonstration of an active switch. High contrast (>10:1) switches were demonstrated. A path to the creation of VLSI WDM photonic switch fabricated was demonstrated.

14. SUBJECT TERMS
photonics, optical switching, microresonators, selective area epitaxy

15. NUMBER OF PAGES
138

16. PRICE CODE

17. SECURITY CLASSIFICATION OF REPORT	18. SECURITY CLASSIFICATION OF THIS PAGE	19. SECURITY CLASSIFICATION OF ABSTRACT	20. LIMITATION OF ABSTRACT
UNCLASSIFIED	UNCLASSIFIED	UNCLASSIFIED	SAR

Abstract

This work discusses the details of design, characteristics and fabrication of novel elements for dense wavelength division/multiplexing (DWDM) systems. Semiconductor optical amplifiers operating at 1.3μm center wavelength and μ-resonators for filters and switches at 1.55μm are also demonstrated.

Tensile and compressive strain quantum wells were used to create polarization insensitive amplifiers with built-in mode transformer sections. Mode transformer regions monolithically integrated with the amplifier waveguide provide mode coupling from the tightly confined elliptical mode inside the semiconductor waveguide to the circular mode in the input/output fiber. We were able to improve butt coupling to a single mode fiber by 3-4 dB compared to losses in an un-tapered device. Alignment tolerances were also improved in both directions.

Our lateral taper design was shown to preserve polarization of the propagating light and does not limit chip gain. Gain for devices with mode transformers was found to be 18dB for both polarizations with polarization dependence less that 1 dB. The saturation power was measured to be 10dBm for both input light polarizations, indicating that the taper does not limit saturation power. The gain bandwidth was found to be 30 nm at –3dB level from the peak. A low reflectivity single layer coating was developed to fabricate this amplifier. Active monitoring allows us to achieve reproducible devices with residual reflectivity as low as 10^{-4}-10^{-5}.

Active and passive μ-resonator elements were developed as add/drop filters and switches. Structures with both passive and active elements were demonstrated. A novel vertical integration approach was proposed and implemented to create completely new device geometry. Vertical coupling provides precise control over device performance and enables novel photonic integrated circuits. Wafer bonding was used to enable the 3-dimensional processing employed with vertical waveguide interaction. Micro cavities, with a quality factor as high as 1500, were denomstrated. Switches based on active cavity resonators were also demonstrated.

Contents

1 *Introduction* *1*
1.1Semiconductro Lasers 3
1.2 Semiconductor Optical Amplifier 5
1.2 Wavelength Selective Elements 7
1.2 Conclusions 10

2 *Semiconductor Laser Processing* *13*
2.1 Introduction 13
2.2 Overview 13
2.3 Material Growth 14
2.4 Broad Area Devices 16
2.5 Ridge Waveguide Lasers 19
2.6 Buried Heterostructure Lasers 20
2.7 Buried Heterostructure Devices with Current Blocking Layers 25
2.8 Laser Testing 33
2.9 Conclusion 37

3 *1.3μm Polarization Insensitive Amplifiers with Integrated Mode Transformers* *39*
3.1 Introduction 39
3.2 Fabrication 43
3.3 Antireflection Coating 47
3.4 Low Reflectivity Coating 49
3.5 Single Layer AR Coating, Fabrication 53
3.6 Results and Discussion 62
3.7 Conclusions 66

4 *Vertical Resonant Couplers with Precise Coupling Efficiency Control Fabricated by Wafer Bonding* ***69***
4.1 Introduction 69
4.2 Device with Vertical Coupling Region 71
4.3 Waveguide Approximation 75
4.3 Numerical Analysis 81
4.5 Device Testing Results 89
4.6 Conclusion 95

5 *μ-Disc Processing* ***97***
5.1 Introduction 97
5.2 Device Structure 98
5.3 Processing Overview 99
5.4 Waveguide Etching 101
5.5 Wafer Bonding 105
5.5.1 Temperature Calibration 106
5.5.2 Bonding Procedure 110
5.6 μ-Disc Definition 111
5.7 Active μ-Disc 113

6 *Conclusions and Future Research Direction* ***116***
6.1Conclusion 116
6.1.1 Semiconductor Optical Amplifier 116
6.1.2 μ-Resonator Devices 118
6.2 Future Research Direction 119

6 *Appendix A:ECR calibration* ***122***
A.1 InP Etching 122
A.2 Etching with Chlorine 126

List of Figures

Figure 1.1 Typical WDM System Configurations 2
Figure 1.2 Typical Semiconductor Laser Diode 3
Figure 1.3 Cross-sections of RWG and BH Lasers 4
Figure 1.4 SOA = Laser without Feedback 6
Figure 1.5 Mode Transformations within a Semiconductor Waveguide 7
Figure 1.6 Add/Drop Node Extract/Add Single Channel 8
Figure 1.7 Novel Vertical Coupler, Proposed and Implemented 9

Figure 2.1 Schematic of Double-Heterostructure Laser 13
Figure 2.2 Typical RWG and BAL laser structure used in our study. 15
Figure 2.3 Cross section of the Etched Channel for a Broad Area Laser, Distance between the Trenches is 60 μm 17
Figure 2.4 Broad -Area Laser, P Contact 18
Figure 2.5 Ridge Waveguide Laser with Photoresist (Cross-section) 19
Figure 2.6 Wet Etched Laser with Near Field Pattern 21
Figure 2.7 Initial Structure Grown for BH Processing 21
Figure 2.8 SEM Picture of Etched Sample 22
Figure2.9 Buried Heterostructure Laser with Submicron Waveguide Region 23
Figure 2.10 Sample Structure Before ECR Etching, Notice no SiNx Mask Layer 24
Figure 2.11 Layer Structure After an ECR Etching 24
Figure2.12 Final Profile of the Buried Waveguide Laser 25
Figure2.13 Structure, Composition and Thickness of the CBL Sample 26
Figure 2.14 Current Blocking Layer Used in This Study 27
Figure 2.15 Leakage Current 28
Figure 2.16 Profile and Structure of Tested Samples 29
Figure 2.17 Buried Heterostructure Fabricated by Wet Etching on the Right and Device Made with Dry Etching On the Left. 30
Figure 2.18 IV Data for Both Samples (Wet and Dry Etched) 30
Figure 2.19 SEM Picture of CBL Layers with Two Different Thicknesses 32
Figure 2.20 Characteristic for Thick CBL Compare to the Usual Thickness 32
Figure 2.21 Cross-section for Optimized and Unoptimized Devices 33
Figure 2.22 Typical Light-Current Data for Broad Area Lasers 34
Figure 2.23 Threshold Current Density for Four Quantum Compressively Strain Well BAL 34
Figure 2.24 Typical Near Field Pattern from Broad Area Laser, Below Threshold (left) and above Threshold (right) 35
Figure 2.25 Far Field Measurements for RWG Device 36
Figure 2.26 Near Field Data for the Same Device as the One Used for Far Field (Figure 2.24) 37

Figure 3.1 Coupling Loss vs. Diameter of the Guiding Core 40
Figure 3.2 Selectively Grown Structure with Mode Transformer Region 41

Figure 3.3 Schematic Diagram for Mode Transformation Done with Passive Waveguide 41
Figure 3.4 Lateral Taper Waveguide with Mixed Quantum Well Structure 42
Figure 3.5 Far Field Divergence angle vs. Waveguide Width for 0.3μm Thick Waveguide 43
Figure 3.6 Optical Momentum Matrix Element for the Electron is Overlap with Light Electric Field Vector for Different Directions 44
Figure 3.7 Light vs. Current for Different Polarization in Broad Area Laser with Mixed Quantum Well; Right Picture Presents TE and TM Spectrums for the Same Laser 45
Figure 3.8 Waveguide Structure for the Amplifier Sample 46
Figure 3.9 Angle Facet Amplifier Structure 47
Figure 3.10 Window Facet Structure Principal Design 48
Figure 3.11 Effective Reflectivity as a Function of Buried Region Length 49
Figure 3.12 Single Layer Antireflection Coating 50
Figure 3.13 Model for Multilayer Laser Diode, Used in Analysis $z<0$-waveguide and $z>0$ AR coating layers 51
Figure 3.15 Calculation for Single Layer AR Coating, Results for Plane Wave Approximation and Guided Wave Calculation on the Same Graph 53
Figure 3.16 Index as a Function of Background Oxygen Pressure 54
Figure 3.17 Index as a Function of Initial Pressure with Additional Oxygen Filled to $2*10^{-5}$ level 55
Figure 3.18 Schematic Diagram for a Circuit Used for Active Reflectivity Monitoring 56
Figure 3.19 Trace Recorded form First Facer Deposition 57
Figure 3.20 Light-Current Data for 6 Lasers Coated Together on the Same Bar 58
Figure 3.21 Spontaneous Emission Spectra for Laser before and after AR Coating 59
Figure 3.22 Theoretical Fitting of the Experimental Data to Calculate a Reflectivity 60
Figure 3.23 Amplitude and Phase of Induce Voltage Generated on the Chip as a Result of Input Light Modulation Light 61
Figure 3.24 Alignment Tolerance to Single Mode (9μm Core Diameter) Fiber 62
Figure 3.25 Chip Gain versus Pumping Current for TE and TM Input Light Polarization 63
Figure 3.26 TE and TM Gain versus Output Power .The 3dB Saturation Power is Measured to be ~10 dBm Independent of Polarization 64
Figure 3.27 Chip Gain and Intensity of Spontaneous Emission vs. Wavelength for Mixed Strain Amplifier with Integrated Mode Coupler 65

Figure 4.1 Schematic Diagram for Add/Drop Note with
Single μ-Disc Coupled to 2 Waveguides 70
Figure 4.2 μ-Disc Laterally Coupled to Waveguides 71
Figure 4.3 Design of the Vertical Coupler 72
Figure 4.4 Picture of Final Structure; μ-Disk is
Suspended on Input/Output Waveguides with an Air Gap Below 74
Figure 4.5 Cross Section for 40 μm Suspended μ-Disk 74
Figure 4.6 Geometry and Index Profiles of 2 Coupled Waveguides 76
Figure 4.7 Coupling Estimation for 10-40 μm Ring (Solid
Lines) with Semiconductor Spacer Layer and with Air
(Broken Line) Spacer for 40 μm Ring 78
Figure 4.8 Q-factor for Loaded Cavity vs. Separation 80
Figure 4.9 Bandwidth as a Function of Separation for 20μm Ring 81
Figure 4.10 Structure Prepared for Simulation with Imbedded Waveguide
and Boundary Layers 82
Figure 4.11 Electro-Magnetic Field Plotted on the Top of
μ-Ring Waveguide with Absorbing/AR Coating Surrounding Regions . 84
Figure 4.12 Signal vs. Time for the μ-Ring Resonator 84
Figure 4.13 Resonance Frequencies fro μ-Ring/μ-Disc with
the Same Diameter 85
Figure 4.14 Energy Distribution in a μ-Ring for 2 Adjacent Modes 86
Figure 4.15 Initial Guess Field for μ-Resonator Coupled to
Input/Output Waveguides 87
Figure 4.16 Resonance Mode Filtered for a μ-Disc
Coupled to Input/Output Waveguides 87
Figure 4.17 Initial field for 3D Vertical Coupler
Gray Line Represents AlOx Regions, Used to Confine Cavity Mode ... 88
Figure 4.18 Resonance Mode for vertically Coupled Structure 89
Figure 4.19 Testing Setup Used for Wavelength
Selective Measurements 90
Figure 4.20 Transmission Spectra for 40 μm μ-Disk 90
Figure 4.21 Output Light for 2 Waveguides 92
Figure 4.22 PL data for Active μ-Disc Device 93
Figure 4.23 Gold Contact on the Top of the μ-Ring 94
Figure 4.24 Transmission Data for an Active μ-Disc Device 94

Figure 5.1 Schematic Drawing for Resonator Vertically
Coupled to the Waveguides 97
Figure 5.2 Device Structure Used for Vertical Coupler 99
Figure 5.3 Vertical Coupler Processing Overview
a) As-Grown Structure with Coupled Waveguide Layers
b) I / O waveguide Formation
c) Wafer Bonding to Transfer Substrate
d) Growth Substrate Removal and Disk Formation 100
Figure 5.4 Mode Number vs. Waveguide Thickness 102
Figure 5.5 Effective Index for an Air Confined Waveguide vs. Thickness 103

Figure 5.6 Mode Number for RWG 103
Figure 5.7 Effective Index as a Function of Waveguide
Thickness for RWG and ASA Structures 104
Figure 5.8 Cross-Section of an Etched Sample 105
Figure 5.9 Testing Sample Layer Structure and SEM Photograph
or Bonded Interface 106
Figure 5.10 PL data for InP Bonded Samples 107
Figure 5.11 Current-Voltage Characteristic and Resistance
Data for Bonded Samples 108
Figure 5.12 LI Data for InP Broad Area Lasers 109
Figure 5.13 Bonding Fixture Used for Samples Bonding 110
Figure 5.14 Top View of the Bonded Sample without Voids 111
Figure 5.15 Top View for a μ-Disc Etched on the Top of Waveguides 112
Figure 5.16 Cross-section SEM Image for Bonded μ-Disc Device 113
Figure 5.17 μ-Ring with P-contact on top, Fabricated by Using
Self-alignment Technique 114

Figure A.1 Schematic Drawing for an ECR System 122
Figure A.2 Etching Rate vs. Methane/N2 Ratio 124
Figure A.3 ECR Etched Surface 100V Self Induced DC Bias with
Polymer Already Removed 125
Figure A.4 Top View and Cross-Section on the Sample With Polymer
Like Deposition 126
Figure A.5 InP Sample Etched in $BCl_3$and Ar Gas Combination 127
Figure A.6 InP Sample Etched with BCl_3 and O_2 Gas Combination 127
Figure A.7 Reflectivity Monitoring Data for GaAs Waveguide 128
Figure A.8 Calculated Reflectivity vs. Etching Depth 128

Chapter 1

Introduction

Fiber optic communication systems are the backbone of today's information society. The rapid increase in the volume of information used today creates a strong demand for faster and more reliable connections. The emergence of the Internet in the last few years has completely changed the way we communicate. Beginning in the 1980s, the optical fiber proved to be the supreme transmission medium for long and medium distance networks due to its unique properties: 1) The total bandwidth for a single mode fiber is potentially up to 30 Thz [1] (10 thousand times that of coaxial cable). 2) The loss at the 1550 nm window is as low as 0.2 dB/km [1], which is at least an order of magnitude smaller than that of other transmission media. 3) Zero dispersion can be achieved around 1310 nm. Dispersion is less that 2ps/nm/km across the entire transmission window [2]. 4) Signals with different wavelengths can propagate in the same fiber without interaction. 5) Low cost, reliable optical fiber backbone networks make possible fast, high volume communication systems. Examples of such systems include Electronic mail and the World Wide Web (WWW), which are casual and useful tools used in every day life.

In the past, research efforts in optical communications were essentially made towards transmission technologies by improving fiber properties. Now, the major problems in optical transmission are basically solved. For future communication networks, efforts will be made to fully utilize the potential bandwidth of optical fiber. Today the most popular solution is to simultaneously propagate many wavelengths on the

same fiber and utilize as much fiber transmission bandwidth as possible. In this case all electronic devices require no more bandwidth that that associated with a single channel, while the bandwidth of the whole system is equal to *number of channels* x *single channel bandwidth.* This is known as wavelength division multiplexing (WDM), or, as the number of channels increased, dense wavelength division multiplexing (DWDM). Figure 1.1 shows one way how this can be realized:

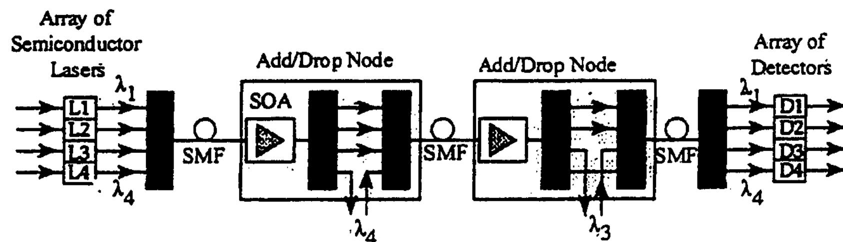

Figure 1.1 Typical WDM System Configurations

DWDM is currently the main technique used in realization of optical networks. It is also important in that it is easy to implement multiple-access in this way. That is, a large number of users can share the same fiber line. To implement this we would be able to add or remove any channel without distorting the others.

Key questions for WDM systems are how many wavelengths can be used and what is the minimum channel separation? The power in the fiber should be high enough so that after extraction any single channel is definitely detected. Separation between channels should be large enough to make single wavelength extraction possible. Semiconductor devices play a pivotal role in the elements for amplification and channel extraction. Semiconductor optical amplifiers are used as power boosters, while high Q cavities made from semiconductor materials are used to implement multiplexing/de-multiplexing elements. Lasers and detectors used to converse between electrical and optical parts of the network.

1.1 Semiconductor Lasers

This section briefly discussed the important features of semiconductor lasers. The performance of the chip is governed by a large number of emission characteristics related to the static, dynamic and spectral behavior of the light output. We are going to study factors affecting final device characteristic performance. Details and results of these studies are presented in Chapter 2.

In general terms, a laser is an externally pumped, self-sustained oscillator and consists of a gain medium that is placed inside an optical cavity to provide the necessary feedback. In semiconductor lasers a semiconductor material is electrically pumped using a forward-biased p-n diode structure, and charge carriers injected into a thin active layer (quantum well) provide the optical gain.

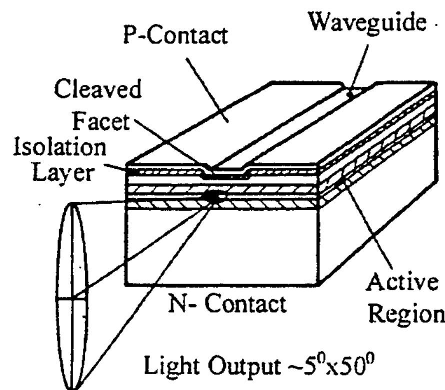

Figure 1.2 Typical Semiconductor Laser Diode

No external cavity is required since cleaved facets of the semiconductor gain medium itself can provide sufficient optical feedback. The laser reaches threshold when the gain is sufficient to overcome the cavity losses. Any further increase in current leads to light emission by stimulated emission.

We typically want to reduce threshold current to improve laser performance. To do this we have to limit the spread of the carriers and confined optical mode inside the laser waveguide. In a double heterostructure laser (which will be the subject in this research) the optical mode is confined perpendicular to the junction plane because the cladding layers have a lower index of refraction compared with that of the active region. For stable fundamental mode operation with a low threshold current additional confinement of the optical mode along the junction plane is required. In the absence of this lateral mode confinement (which may be induced by a region of well-defined optical gain or a refractive index step) the laser behaves as a broad area laser with a high threshold current. Such high threshold current would limit possible applications for this design. Typically broad area devices are used for material characterization only and have a threshold current in order of 300-500 mA.

The laser structures described in this thesis are index-guided lasers, where a narrow central region of relatively higher refractive index in the junction plane confines the lasing mode to that region. We used different lateral-mode confinement mechanisms to limit the spread of carriers and spread of laser mode in a junction plane. The index-guided lasers can be divided into two general subgroups, weakly index guided (such as a ridge waveguide) and strongly index-guided lasers (buried heterostructure).

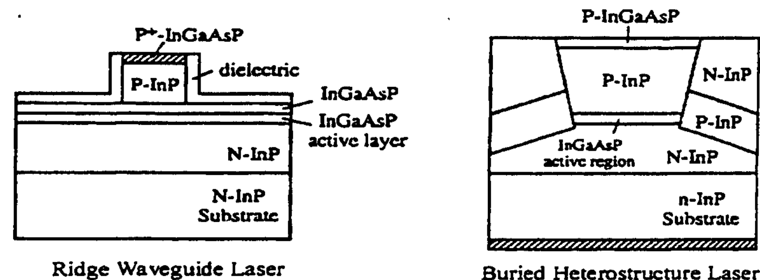

Figure 1.3 Cross-sections of RWG and BH Lasers

In weakly index-guided lasers, the active region is continuous and a cladding layer of varying thickness provides the effective index discontinuity. In buried heterostructure lasers, the active region is bounded by low-index, epitaxially grown layers both along and normal to the junction plane. The lateral index difference is 0.01 for weakly index-guided lasers and 0.2 for strongly index-guided, buried-heterostructure lasers. The final goal of this research is to obtain a laser structure with a low threshold current that can operate in the fundamental lateral mode up to high powers. State-of-the-art InGaAsP lasers emitting near 1.3 μm generally have threshold currents in the range 10-15mA.

1.1 Semiconductor Optical Amplifier

Semiconductor optical amplifiers (SOAs) allow the direct amplification of light, without the need for optical to electrical conversion. They provide the amplification necessary to overcome the attenuation associated with fiber and other optical components. In point-to-point systems they can be used as power boosters, repeaters, or receiver preamplifiers, although the exact requirements for each application are different [10,11]. One of the main advantages of SOAs are that they provide amplification for all the channels and can replace a whole system of opto-electronic regenerators: demultiplexing /amplification/multiplexing

SOAs are especially important at 1.3mm range where no other optical amplifiers are available. The importance of the amplifier is that it provides high gain (up to 30 dB) over wide bandwidths (approximately 4 THz) [12], and this performance is unmatched by any electronic component. The wide optical bandwidth of the amplifier matches

reasonably well with that available from the fiber itself. Their small size, high gain and high saturation power make them very attractive.

Figure 1.4 is a schematic diagram of an SOA, which is essentially a semi-conductor laser without feedback.

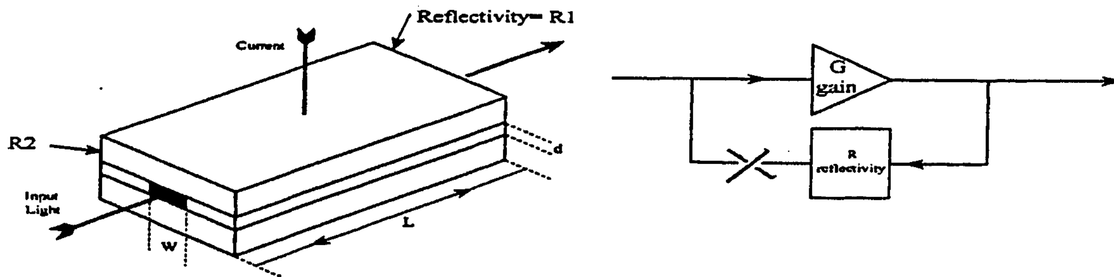

Figure 1.4 SOA = Laser without Feedback

The end facets of the amplifier must have a reflectivity, *R*, much smaller than in the case of a standard laser. *R* is roughly 0.3, due to the difference in refractive indices between the laser material and air. If we call *G* a single pass gain than lasing occurs when $G*R\sim1$, so we must reduce *R* go get high gain. Special facet coatings can be used to reduce reflectivity down to 10^{-4}-10^{-5}, which lets us make high gain devices.

Polarization insensitivity is one of major requirements for an SOA [13]. Most of the fiber networks today use single mode fiber without any support for maintaining polarization, so light propagating in such a fiber changes polarization as a function of temperature, bending, stress and almost any other factor. Variation in input light polarizations will result in amplitude modulation if we have polarization sensitive gain, creating amplitude noise. Another inherent problem of all semiconductor devices is the mode mismatch between the circular fiber mode (8-9μm. in diameter) and the highly confined, elliptical mode inside semiconductor waveguide with typical dimensions

around 1 μm [14,23]. Small mode sizes tightly confined in semiconductor waveguides result in a high divergence angle, which exceeds the fiber acceptance angle. The divergence angle and mode mismatch results in high coupling losses, typically around 8-10dB. Sophisticated optics could be used to improve the coupling, but it makes packaging very expensive and increases final device cost.

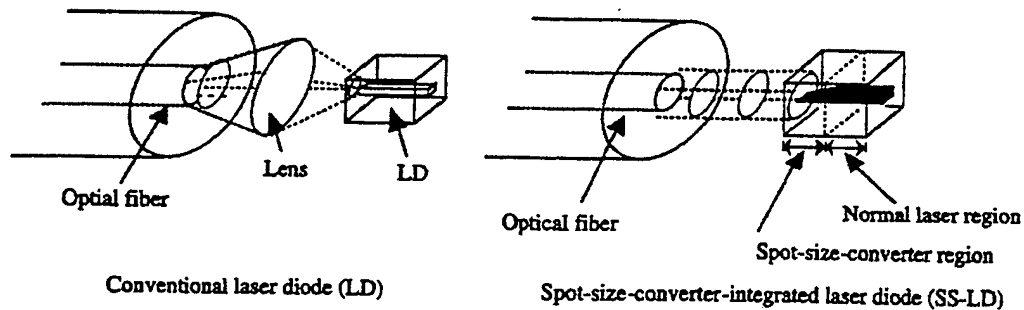

Figure 1.5 Mode Transformations within a Semiconductor Waveguide

An alternative approach is to modify the mode within the device, by changing the guiding properties. We can expand a guided mode by modifying the optical confiment and still preserve polarization to create a useful device.

Chapter 3 will describe the design and realization of a polarization insensitive SOA with monolithically integrated mode transformer region. A Polarization insensitive amplifier with spot size converter was tested and studied for the first time, and the results will be discussed.

1.2 Wavelength Selective Elements

Many wavelengths can propagate simultaneously inside a single mode fiber to cover the full fiber bandwidth. To completely utilize the fiber's capacity, wavelength selective elements are necessary to multiplex/demultiplex signals with specific wavelengths

propagating within the fiber. We should be able to add or to extract a channel without distorting the other ones [24-27]. High Q-cavities have to be used for such purposes.

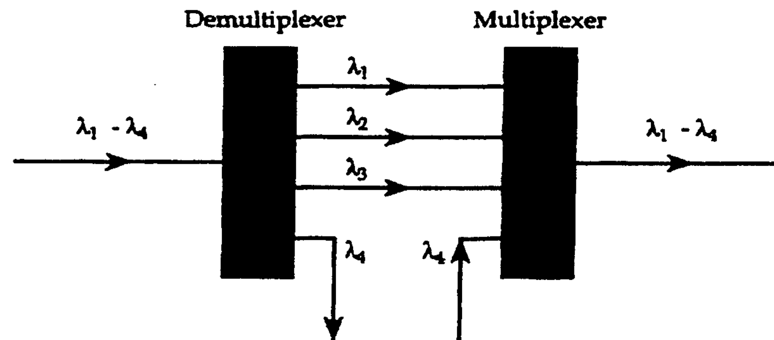

Figure 1.6 Add/Drop Node Extract/Add Single Channel

Wavelength separation used in today network is 0.3nm. It is defined by the standards of current DWDM systems. A cavity has to have a Q-factor of at least 3000-5000 to be able to add/drop each channel. A particularly ambitious goal is to drop just one channel. Free spectral range in resonators is inversely proportional to cavity size, so extremely small resonator devices should provide an ideal solution.

μ-Cavity devices are usually extremely small ring/disk resonators, where optical waves evanescently propagate near the outer edge of the ring/disc. This resonating ring - analogous to resonators used in electronics and microwave devices - could be used as a filter for WDM and as an integrated optical switch or modulator. High index step between the semiconductor inside the disk and air outside supports resonant disk modes even for small diameter disks. Typical sizes for these devices are 10 –100μm.

Experimentally, μ-cavity devices have been demonstrated in many material systems [26, 28], but III-V semiconductor materials are especially interesting. First of all III-V is a basis of present optoelectronics systems. Therefore, new microelements can be

easily integrated with present devices. Second, InP based material can easily be made active (have gain or absorption) inside a μ-cavity; hence, we could implement switches, modulators and other wavelength selective active devices.

Two other groups of researchers have recently been working on the integration between μ-rings/disks and waveguides [25,27]. In both their structures, light is propagated in a strained, thin waveguide. A ring/disk of the same material if formed closed to waveguide, so light at a certain wavelength couples into the ring from the first waveguide. At the resonant wavelength the ring structure can couple most of the light from the first waveguide to the μ-cavity and out to the second waveguide (see Fig. 1.7).

The main problem for this configuration was control over coupling. Optical modes decay exponentially fast in air so it was extremely difficult to make this kind of device. Here at USC we proposed to integrate the μ-disk on the top of waveguide (see Figure 1.7). We used material growth (instead of the lithography employed before) to control waveguide separation. This gives us precise control over coupling, as is explained in Chapter 4 and 5. Novel processing was developed to implement this structure. Wafer bonding was used to process multilayer devices.

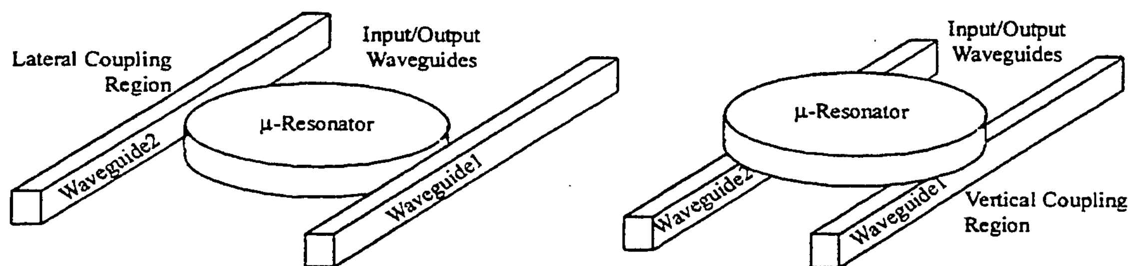

Figure 1.7 Novel Vertical Coupler, Proposed and Implemented

Chapter 4 and 5 in this thesis present numerical calculations, experimental results and processing for the μ-ring device. Small size, high Q-factor, and large free space range make this novel, vertically coupled resonator an ideal add/drop filter for WDM

A particularly ambitious goal is building a fully integrated optical circuit on one chip. μ-Resonators have emerged in recent years to become a promising element in integrated optical circuits. Current integrated optical circuits require large areas on a chip, owing to the need to use adiabatic bending and splitting elements to avoid waveguide losses. This limits the number of elements that can be placed on the chip and increases "real estate" required to create a circuit. All of this limits the current complexity of optical circuits. μ-Resonators are extremely small elements and are versatile elements for integrated optics. Micro-cavities with high quality factor are ideal candidates for large-scale optical integration with device density on the order of 10^4-10^6 elements/cm^2 (compare with typical values of 10-100 devices/cm^2). By combining several resonators appropriately it is possible to achieve sophisticated control over wavelength routing and device response. Semiconductor optical amplifiers could be also integrated in photonic circuits to compensate losses. Input /output taper structures can also be used to optimize coupling to fiber lines.

1.3 Conclusions

This dissertation is dedicated to a building block development for the optical integrated circuit. Therefore positive results obtained in this research hold a lot of significance and may create a big impact on future developments in integrated photonics.

References

1. J. P. Hirtz, M.Razeghi, M.Bonnet and J.P.Duchemin, in GaInAsP Alloy Semiconductors, edited by T.P Pearsall, Wiley, 1982

2. V. Swaminathan and A.T.Macrander, Materials Aspects of GaAs and InP Based Structures, Prentice-Hall, 1991

3. S. Adachi, "Material parameters of InGaAsP and related binaries,"J. Appl. Phys. ,vol. 53, number 12, pp 8775-8792, Dec. 1982

4. O.Madelung, Semiconductors - Group IV Elements and III-V Compounds, Springer-Verlag, 1991

5. Atul Mathur, Ph.D. Dissertation, University of Southern California, 1995

6. Atul Mathur, Julian Osinski, Piotr Grodzinski and P.D.Dapkus, "Comparative Study of Low-Threshold 1.3μm Strained and Lattice-Matched Quantum-Well Lasers," IEEE Phot. Tech. Lett., vol. 5, no. 7, pp. 753-755, July 1993

7. Brakett " DDWM network, principals and application"IEEE J. Select. Areas Communication, vol 9,pp. 948-964 1990

8. Midwinter , "Photonics in swithching, background and components" Academic Press, Inc., San Diego, CA 1993

9. T.Miya, Y.Terunuma, T.Hosaka and T.Miyoshita, Eleec. Lett. 15, (1979) 106

10. A.Sugimura, K.Daikoku, N.Imoto and T.Miya, IEEE J.Quan. Elec., 16, (1980) 215

11. G.P.Agrawal and N.K.Dutta, "Long Wavelength Semiconductor Lasers", Van Nostrand Reinhold, 1993

12. S. Dubovitsky, A. Mathur, W. Steier and P. D. Dapkus: "Gain Saturation Property of a Polarization Insensitive Semiconductor Amplifier Implemented with Tensile and Compressive Strain Quantum Wells." IEEE Phot. Tech. Letters 6, 176-178 (1994)

13. D. Tishinin, K. Uppal, I. Kim and P. D. Dapkus, "1.3μm Polarization Insensitive Amplifiers with Integrated Mode Transformers" PTL, vol. 9,No 10, October 1997 pp.1337-1339

14. S. Dubovitsky Ph.D dissertation, USC 1994

15. L.C.Su, I.H.Ho and G.B.Stringfellow, J.Cryst. Growth, 146, (1995) 558

16. H. Zhao, M.H. MacDougal, K. Uppal, Y. Cheng, G.M. Yang, and P.D. Dapkus, Journal of Quantum Electronics 1, (1994) 196

17. J.Diaz, I.Eliashevich, K.Mobarhan, E.Kolev, L.J.Wang, D.Z.Garbuzov and M.Razeghi, IEEE Photon. Tech. Lett., 6, (1994) 132

18. G.Zhang, J.Nappi, H.Asonen and M.Pessa, IEEE Photon. Tech. Lett., 6, (1994)1

19. J.Diaz, I.Eliashevich, X.He, H.Yi, L.Wang, E.Kolev, D.Garbuzov and M.Razeghi, Appl. Phys. Lett., 65, (1994) 1004

20. H.Tanaka, Electron.Lett., 29, (1993) 1611

21. A.Mathur, J.S.Osinski, P.Grodzinski and P.D.Dapkus, IEEE Photon. Tech. Lett., 5, (1993) 753

22. D.Coblentz, T.Tanbun-Ek, R.A.Logan, A.M.Sergent, S.N.G.Chu and P.S.Davisson, Appl. Phys. Lett., 59, (1991) 405

23. E.S.Koteles, D.A.Owens, D.C.Bertolet, J.Hsu and K.M.Lau, Surface Science 228, (1990) 314

24. R.Bhat, Semicond. Sci. Technol., pp. 984-993, 8, 1993

25.D. Rafizadeh, J.P.Zhang, S.C. Hagness, A. Taflone, K.A.Stair, and S.T.Ho: "Waveguide Coupled AlGaAs/GaAs Microcavity Ring an Disk Resonators with High Finesse and 21.6-nm Free spectral Range" Optical Letters vol. 22, No16, August 1997, pp.1244-1246

26. J. Foresi,B. Little, G, Steinmeyer, E. Thoen, S.Chu, H. Haus E. Ippen, L. Kimerling, and W. Greene: "Si/SiO_2 Micro-Ring Resonator Optical Add/Drop Filters"LEOS1996 CPD22-2

27. B.E. Little, S.T. Chu, H.A.Haus, J. Forresi, and J.P.Laine: "Microring Resonator Channel Dropping Filters" Journal of Lightwave Technology, vol 15 no 6, June 1997, pp.998-1005

28 S.T. Chu, J. Forresi, and J.P.Laine and B.E. Little "Wavelength Trimming of a μ-Resonator filter be means of a UV sensitive polymer overlay" PLT, vol 7 1998 pp 484-487

Semiconductor Laser Processing

2.1 Introduction

The optical fiber has zero dispersion near the 1.3μm wavelength and has lowest losses near the 1.55μm window. Thus semiconductor lasers emitting in these regions are of interest for fiber-optic transmission applications. The InGaAsP material system is used to fabricate devices working in this range of wavelengths. Construction of semiconductor lasers is the first step in building an SOA. The laser is a very convenient tool to obtain optimized performance. We easily can adjust material parameters in all layers. Proper waveguide design can also be easily tested and modified.

2.2 Overview

A schematic of a typical double-heterostructure used for laser fabrication is presented on the next figure:

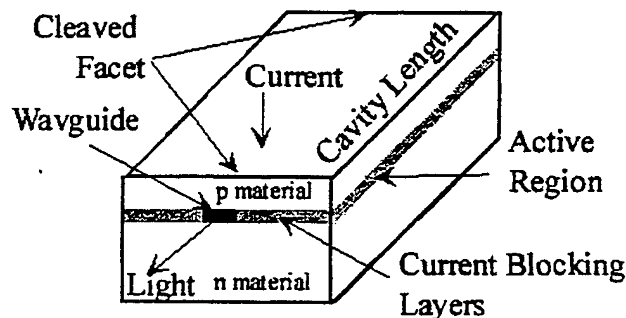

Figure 2.1 Schematic of Double-Heterostructure Laser

It consists of a thin stripe, high index waveguide surrounded (buried) by lower index cladding material. Optical modes propagating in this waveguide get amplified due to spontaneous emission. Cleaved facets on the ends of the waveguide provide the feedback necessary for supporting lasing.

The purpose of the current chapter is to give a brief overview of the process flow for semiconductor laser processing. First, material growth has to be performed to form the waveguide and all other layers. Thereafter there are a considerable number of steps necessary for the fabrication of semiconductor lasers. Lateral current constrictions and index steps in the junction plane have to be defined by later processing. We can use different combinations of etching and regrowth to create lateral index steps. Metal contacts are then deposited on the active device. Last, lapping and cleaving are used to define the laser output facets. All of these steps will be discussed in detail in this chapter.

2.3 Material Growth

In today's world the most popular tool for laser growth is Metal Organic Vapor Pressure Deposition (MOCVD). Samples in this study were grown using the Tomas Swan MOCVD system. We used reactors that employed both horizontal and vertical flow geometries. The latter allows us to deposit material layers on wafers and to achieve better uniformity across the sample. The vertical reactor was equipped with a closed-spaced showerhead. In this head, gases were mixed near the entrance of the reactor chamber to prevent possible pre-reaction.

The sources for InP growth were trimethylgallium(TMG), tertiarybutylarsine(TBA), tertiarybutylphosphine(TBP). Disilane(DS) and dimethylzinc(DMZn) were used for n and p dopants, respectively. For all sources hydrogen was used as a carrier gas. We diffused the hydrogen through a heated palladium membrane for purification. Then it was bubbled through the metal-organic sources to pick up the reactants and transported to the growth chamber. All flow rates and dilution ratios were set by computer-controlled mass flow controllers. Material growth was done at 640^0C at 76 Torr, except for the InGaAs contact layer, which was grown at 590^0C to achieve higher doping and lower contact resistance. To provide a closed feedback loop to the heater power supply a thermocouple was placed into a graphite susceptor.

The following picture presents a typical sample structure for a laser device:

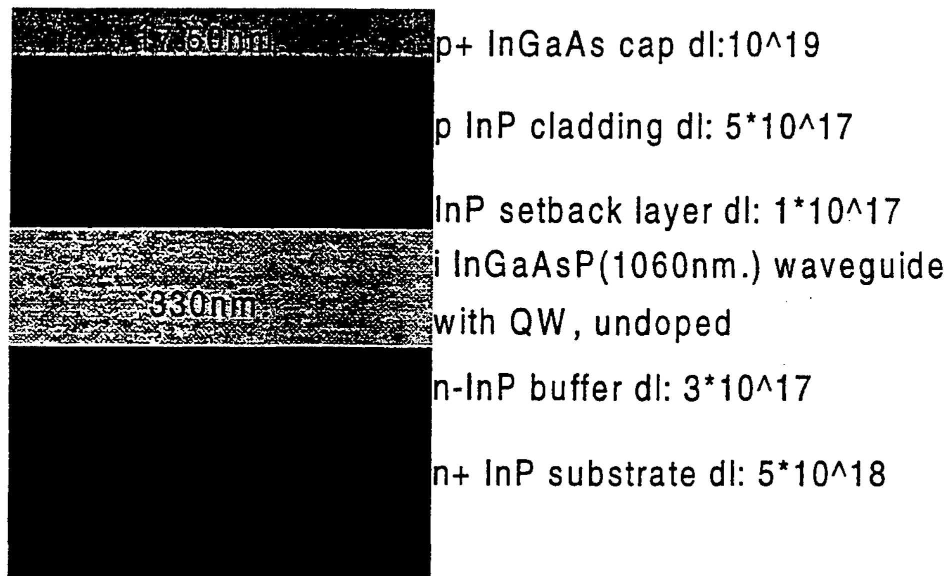

Figure 2.2 Typical RWG and BAL laser structure used in our study.

We also show doping levels and thickness for every layer except the waveguide. Number and composition of quantum wells (QW) was varied from sample to sample, so we will specify this for specific samples when discussed.

2.4 Broad Area Devices

To process lasers from the material structures, the sample first was cleaned with appropriate solvents to remove any traces of organic material. Hence, we started with tricloroethylene (TCE), acetone and methanol rinses. Buffered oxide enchant ($HF:H_2O$ 1:10) was used to remove the native oxide accumulated on the surface after growth. Usually we use a 30 second to 1 minute etch time. BOE does not attack InGaAsP material so this time is not crucial.

We used AZ 5214-EZ positive photoresist to define two channels, each 10μm wide. The laser waveguide is defined as the area between these two trenches. This is a planarized broad area laser and we can choose the width of the device. Broad area devices are usually made with a width around 60-65 μm and channel direction coincides with the [011] crystal plane. Wet etching was then used to transfer a pattern onto the semiconductor.

We selectively etched the InGaAs top contact layer with $H_2S0_4:H_2O_2:H_2O$ (1:1:5) for 6-9 seconds or more using photoresist as a mask. Etching was interrupted when an undercut was seen on a microscope, through the photoresist mask. The cladding layer was etched with HCl based selective enchants. If we use $HCl:H_2O$ (3:1) we get a 57^0 undercut angle and it takes around 25-30 seconds to etch the cladding layer. Photoresist

was removed with acetone after etching and the sample was cleaned using solvents again. To assure the absence of residue on the surface, we dry etched the sample for two minutes in oxygen plasma.

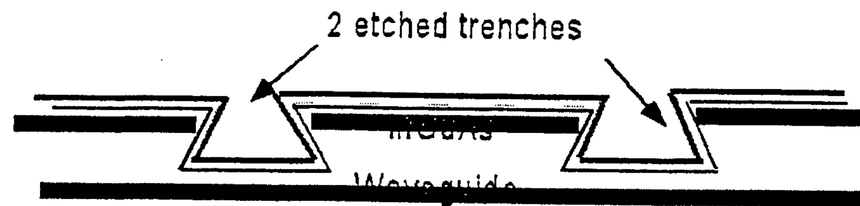

Figure 2.3 Cross section of the Etched Channel for a Broad Area Laser, Distance between the Trenches is 60 μm

A SiN_x layer was then deposited onto the whole surface using plasma enhanced chemical vapor deposition. To prevent evaporation of In from the top layer, we initially reduced the loading temperature to 275^0C. After loading and filling the chamber with SiH_4:NH_3:N_2 (20:60:40) gases, the temperature was increased to 325^0C. Deposition rate was around 100 Å/min, and with typical depositions of 1000Å thickness.

After deposition we washed the sample with methanol again to remove particles, which were accumulated during SiN_x deposition. Then using standard photolithography techniques we opened windows roughly 50μm between the two trenches on the top of the mesa. This opening was used to dry etch SiN_x with CF_4. The etching rate for our condition was around 1000 Å /min. These windows could have been used for lift off in a p-metal evaporation, or we could remove the photoresist and open a wider stripe (around 100μm) on the top of the mesa and SiN_x. This would ensure that the injected current did

not flow outside the mesa area. If we open a wider stripe it is helpful to use image-reversal photoresist, so lift off will be easier.

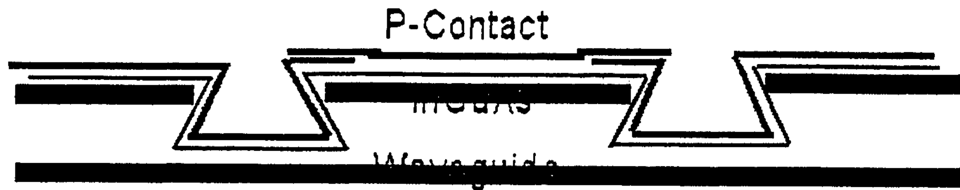

Figure 2.4 Broad –Area Laser, P Contact

We used Ti/Pt/Au (300 Å /1000 Å /1500 Å) as the P-contact metal. The titanium provides an ohmic contact and has good surface adhesion, therefore the contact does not peel off during annealing. Platinum is also used because it stops diffusion of any metal that could be on top of it. This is important for laser lifetime, otherwise diffusion of gold and particularly tin through the thin top cladding layer will significantly shorten its life expectancy. Gold is a good final layer, which is easy to use for wire bonding, probing and testing.

For lift off purposes, we place the sample in acetone after evaporation. Then the backside of the laser is lapped down to 100-150μm. We mainly used a Au-Sn electroplating solution to make an N-contact, but $Au_{0.88}Ge_{0.12}$/Ni/Au (300 Å /300 Å /2000 Å) evaporation is possible too. No mask was used and we have one common contact for all chips on the wafer. To make an ohmic contact we anneal samples in a rapid thermal annealing system (RTA) at 450^0C in a forming gas atmosphere. The sample is then cleaved into individual bars. To do this, we mount the sample with wax on a glass plate

and scribe in the [010] direction near the sample edge with a diamond tip whose separation is defined by the desired cavity length. Then, after removing the wax and cleaning the sample, we use a metal rod to "roll" the sample over and separate individual bars for further processing or testing.

2.5 Ridge Waveguide Laser

Processing of ridge waveguide lasers is very similar to that of broad area devices. However, due to the much smaller mesa size of ridge waveguide devices we use one mask with 2 predefined stripes. Predefined separations allow us to place 3-5 μm waveguides uniformly over the entire wafer. Wet etching was done exactly the same way as for the broad area lasers. We also deposited 1000Å of SiN_x over the entire surface and then used a stripe mask, which was wider than the waveguide, but smaller than the separation between plain regions on the side of the stripe. We adjusted the developing time so that the top of the stripe was clean, but at the bottom of the trenches we still had some photoresist.

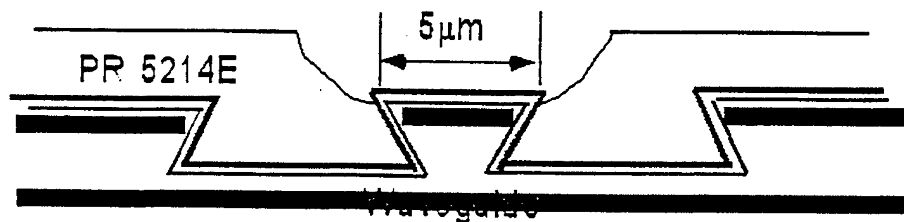

Figure 2.5 Ridge Waveguide Laser with Photoresist (Cross-section)

Standard exposure times were typically between six and nine seconds. Then, in order to open the top P-contact, the opening was used to remove the SiN_x. Double metal

deposition was used to make P-contact. First, we deposited Ti/Pt (300Å/750Å) at an angle. Then after rotating the sample 180^0, we evaporated Pt/Au (750Å/1500Å), so that the total metal thickness was compatible with that of the broad area devices. However, in this case, we were able to cover both sides of the side trench, and we could use the flat side area for probing. In these devices further processing was similar to the broad area devices. We lap the samples down to 100-125μm, electroplate or evaporate the N-contact, and cleave the devices into the single bars.

2.6 Buried Heterostructure Lasers

The buried heterostructure laser was fabricated as a base for devices with an integrated mode-transforming region. To make a good lateral taper section, which we used for mode transformation, we had to define a submicron waveguide. This is very difficult to do using conventional lithographic means, so we developed a way to define submicron stripes using a selective area etching/undercutting technique.

We tried different selective etchants [1], to achieve a near vertical profile in InP ($HCl:HNO_3$ 1:2 or HCL: CH_3COOH 1:1), but we could not obtain a vertical profile in the InGaAsP waveguide, which is an important condition for good, continuous mode transformation. If we have an undercut profile, the mode is forced to displace vertically, coupling to the higher order modes [2]. A wet etched profile causes an effective vertical displacement between the gain section and mode conversion section, resulting in higher order and/or radiation mode coupling.

This multimode behavior is crucial for the mode transformer region [3], because it reduces the overlap between the waveguide mode and the fiber mode, reducing coupling to a single mode fiber as a result. Thus the structure has an effective index variation only in the lateral direction. This is accomplished by changing the waveguide width without creating a vertical profile throughout the whole device, including the mode transformer section.

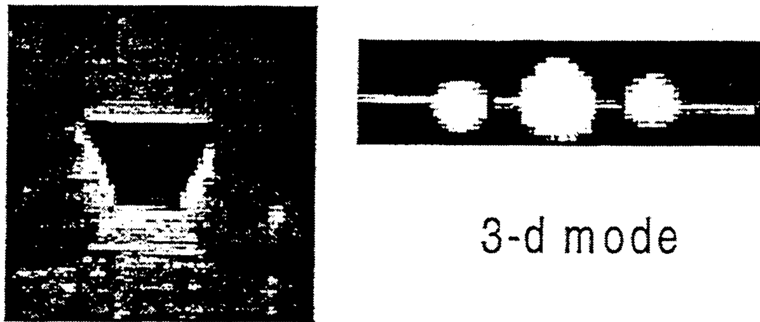

Figure 2.6 Wet Etched Laser with Near Field Pattern

We then attempted dry etching, but in this particular case it is almost impossible to get the undercut [4] needed to reduce the stripe dimension. Thus we had to combine wet and dry etching.

In this case we start with a grown sample with 2 sacrificial layers on top (InGaAs and InP as shown on Figure 2.6.

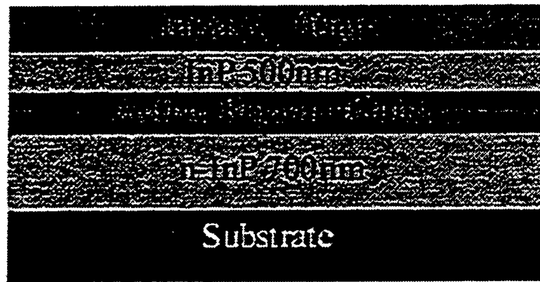

Figure 2.7 Initial Structure Grown for BH Processing.

First, we deposit a 1000 Å SiN_x layer on this surface at 325^0C, which gives us approximately 1000Å. Using standard photoresist technology we pattern two to four micrometer-wide stripes, which is relatively easy to do. These stripes are then transformed into SiN_x by using dry CF_4 etching under standard conditions. Then we use selective etching for InGaAs (H_2S0_4: H_2O_2:H_2O(1:1:10)) to selectively undercut the top layer. This particular etchant is very good because the etching rate almost linearly depends on dilution ratio. Thus, by reducing the etching rate we can increase controllability, which is critical when creating sub-micron stripes. By using a very diluted solution and getting very low etching rates, we were able to obtain reproducible stripes from 0.1 to 0.5 micron wide.

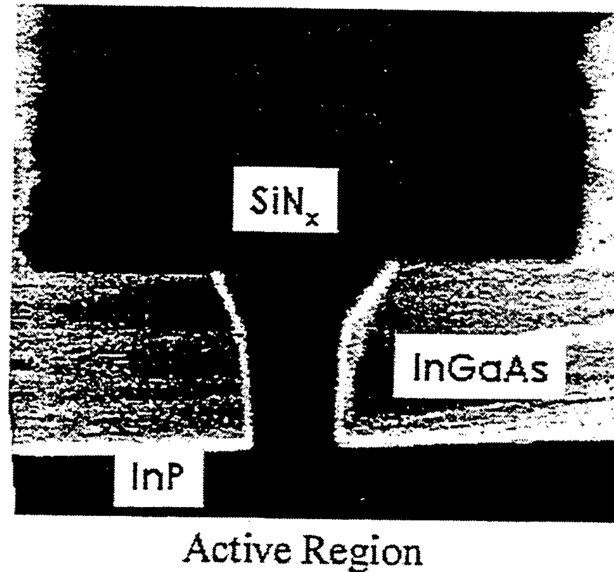

Figure 2.8 SEM Picture of Etched Sample

We then used HCL:CH_3HOOH(1:1), a selective etchant for InP, to etch through the second sacrificial layer up to the waveguide surface. Acetic acid was chosen because it gives us a very vertical profile in the [011] direction with no undercut. After etching with acetic acid, the SiN_x was removed and the sample was ready for dry etching in the ECR. The next picture shows an example of the completed waveguide. We can see that using our processing technique we were able to obtain a wide range of sub-micron waveguides with standard lithography.

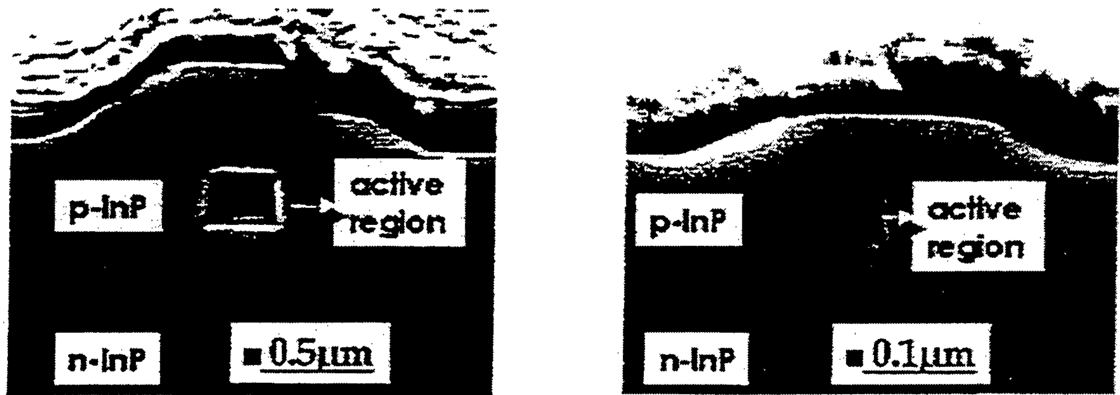

Figure2.9 Buried Heterostructure Laser with Submicron Waveguide Region

In our processing scheme we do not use any SiN_x masks on this set of samples. We only use the ECR to transfer the ridge that was prepared by wet etching through the waveguide layer (for details see Appendix A).

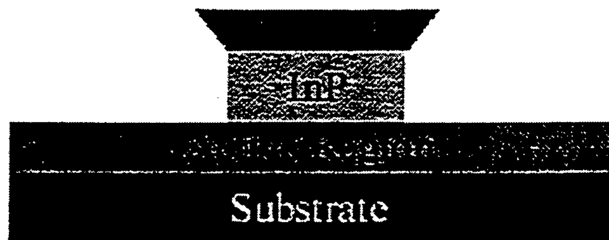

Figure 2.10 Sample Structure Before ECR Etching, Notice no SiN_x Mask Layer

We cannot grow a current blocking layer in this case so we perform an overgrowth over the whole device. To prepare a sample for regrowth we etch in O_2 plasma for 2-5 minutes and then do a standard pregrowth cleaning. During the growth, we add a p-InP top cladding and a p+-InGaAs contact layer.

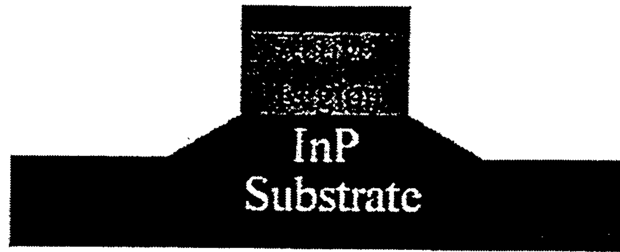

Figure 2.11 Layer Structure After an ECR Etching

After growth we define a 10 μm stripe around the waveguide and use wet selective etching (H_2SO_4:H_2O_2:H_2O, 1:1:5, 10 second) to remove the top contact layer. Then we define a stripe around the waveguide with approximately 4 microns left on each side and use wet etching (HCl:CH_3HOOH 1:1). This is done to reduce leakage currents because we do not have current blocking layers in our device. We deposit SiN_x on the sample in our next step. Then we open a 2 μm wide stripe on the top of the mesa through SiN_x to create a current pass. The rest of the process is exactly the same as that in the broad area or ridge waveguide devices.

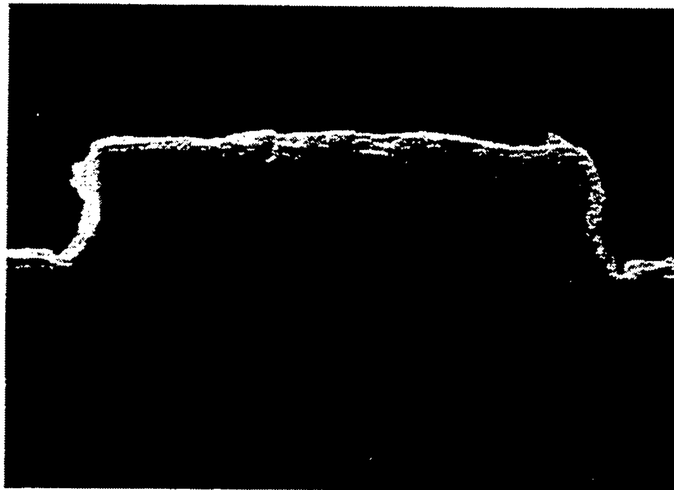

Figure2.12 Final Profile of the Buried Waveguide Laser

2.7 Buried Heterostructure Devices with Current Blocking Layers

Device designs without current blocking layers (CBL) always have some leakage current. This current does not contribute to pumping the active region, and therefore increases threshold, reduces efficiency, and eventually results in laser performance degradation [5,6]. One of the ways to reduce this waste of current is to grow a reverse biased pnpn junction outside the waveguide area, so that the current will not flow through this material. To do this, we must have a SiN_x layer on the top of the waveguide after ECR or wet etching, so that during the next growth, the semiconductor material will be added only to the plain area around waveguide region. This area around the waveguide region will then no longer conduct current.

Device leakage currents were still observed even with the CBL structure. There are three different sources for leakage current in devices with CBLs. First, we can have imperfect junctions. Hence, we can have some leakage through the reverse biased junctions. Second, defective interfaces between the current blocking layers and the waveguide can cause some leakage. Finally, leakage current can flow through the waveguide itself under reverse bias. The last cause does not contribute to an increase in the threshold current, but makes it harder to distinguish itself from first and second causes. This is because the most typical way of leakage current examination is done by looking at the current during reverse bias conditions. We cannot see it leakage under forward bias due to the high diode current, which completely masks any possible leakage.

In the following set of experiments we want to check the quality of our current blocking layers, and find our main source for leakage in our devices. To do so we first prepare a set of samples with different current blocking layers and vary the doping, thickness and number of layers. Each of these samples has a contact area of 100x100μm where we measure the leakage current. The structure for all samples was the same except for the current blocking layer design.

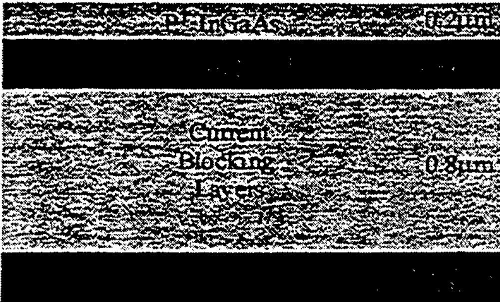

Figure2.13 Structure, Composition and Thickness of the CBL Sample

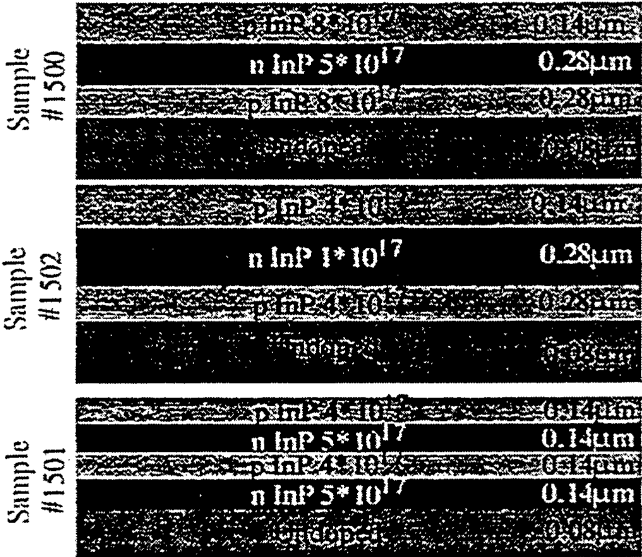

Figure 2.14 Current Blocking Layer Used in This Study

We changed the number of CBL layers from three on sample 1500 and 1502 to five on sample # 1501. Doping was changed between high levels (on 1500) and low levels (on sample 1502) as well. The specific doping concentration value may not be exact but sample 1502 definitely has a lower doping than sample 1500. All three samples have the same overall thickness for the CBL layers. The results show that only the sample with low doping and one reverse pn-junction shows no leakage current. It should be pointed on the graph that in this case both reverse and forward biases cause leakage current.

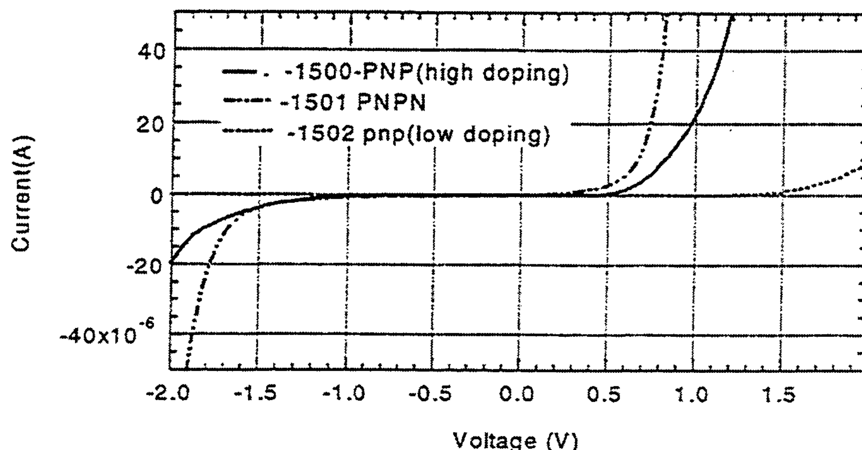

Figure 2.15 Leakage Current

We can see from these graphs that only the sample with low doping gives the minimal amount of leakage current through the CBL directly. Samples with high doping and an increased number of interfaces demonstrate degraded performance. We speculate that if we increase the doping level we increase the number of defects in the CBL, which causes a decrease in resistivity [9]. If we put two reverse biased pn junctions into the device (without increasing the thickness) we also degrade performance due to increases in defect number. Therefore we decided to put one reverse pn junction with low doping

in our devices. Even though we see some leakage, it is much smaller (2-3 orders of magnitude) than that seen in typical laser devices. Typical devices usually show roughly 1-2mA at -2V reverse bias (in our devices we have only 40 μA in the worst case.)

To check the source of the leakage current we decided to make two identical devices, located side-by-side, one with the waveguide and the other one with a current locking layer even inside a stripe. It is worth noting that in the previous set of experiments no etching had been done on the sample. We simply defined a contact on top. In the current case, we actually etched a stripe through the CBL structure and then overgrew it again with another CBL. Hence, in addition to leakage current through the CBL itself we could have a leakage through the growth interface. Since two identical stripes were defined on the sample (quaternary waveguide and CBL), we could separate the current leaking through waveguide (at reverse bias) from leakage current caused by an interface effect.

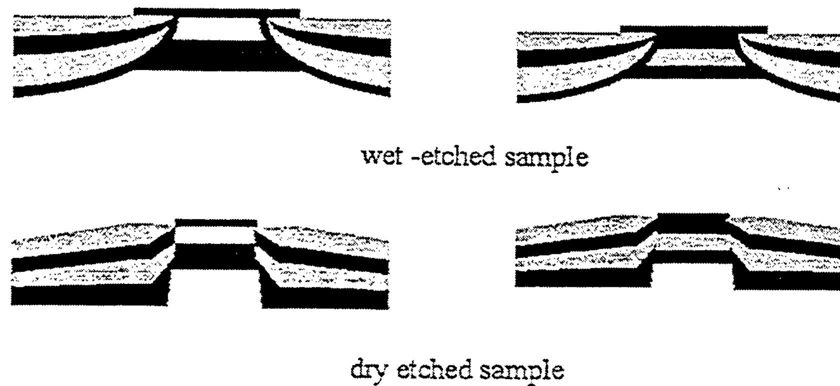

Figure 2.16 Profile and Structure of Tested Samples.

We used $HBr:H_2O_2:H_2O$(5:1:25) to etch the devices. This non-selective acid gives a nice, smooth profile, which is suitable for regrowth. ECR etching with $CH_4/N_2/Ar$ was used to make dry-etched devices. Comparing the right side of Fig. 2.16, showing the wet-etched sample, with the picture on the left, showing the dry-etched sample, we can see that due to the difference in profile, we have different current blocking layer structures near the etched edges.

Figure 2.17 Buried Heterostructure Fabricated by Wet Etching on the Right and Device Made with Dry Etching On the Left.

We performed the same regrowth on both these samples, then SiNx was removed and a second regrowth was done. We next grew p-type InP cladding and P+InGaAs contact layers together. Standard processing was then used to make the final devices [7]. The results of standard current-voltage measurements are presented on the next Figure:

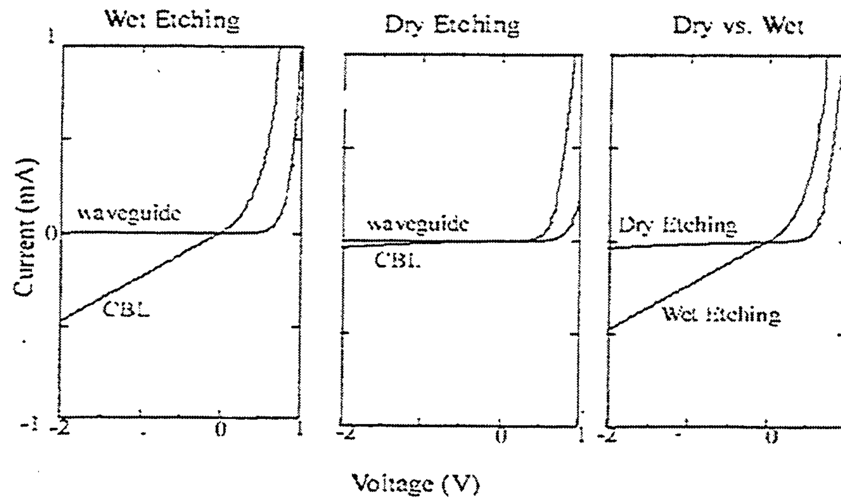

Figure 2.18 IV Data for Both Samples (Wet and Dry Etched)

We can see from the pictures that both CBLs have very low resistance, but conductivity in the stripe region is completely different. First we point out that leakage current is much higher in the sample with the stripe defined by wet etching. We believe that, in the wet etching case, we have a very smooth surface, so growth initially starts on the entire area of the sample. Therefore, the first current blocking layer, which has to be isolated from top surface, is actually in contact with a P-doped InP cladding layer near the stripe edge. Hence, current can spread through this high-doped layer and effectively increase the junction area. In the case of the ECR-etched sample, we have nearly vertical walls. It takes some time to overgrow these walls as well as the lower p-doped layer, and terminate growth before touching the top p cladding. Thus we have effective current blocking even near the stripe edge, and all current is channeled through an active region. On the other hand, in devices made by wet etching we can try to isolate the bottom p layer in the CBL from the top cladding by increasing the thickness of the whole CBL

structure. An SEM photo of the two structures is presented in Figure 2.21. On the right side, we have a sample where the regrowth thickness is equal to the etching depth, and on the left we can see a thicker regrowth.

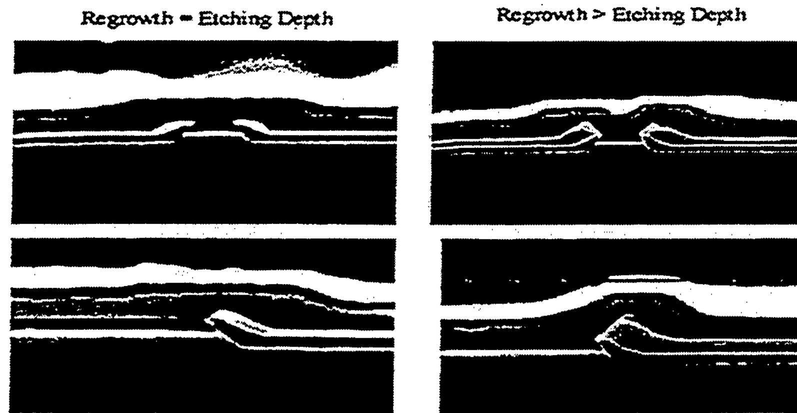

Figure 2.19 SEM Picture of CBL Layers with Two Different Thicknesses

We can see from this photo that an increase in CBL thickness actually does not help, because we still have fast sidewall coverage and all material merely creates a bump around the stripe. We checked the current-voltage characteristics for these samples and we found out that the sample with a thick CBL indeed has a higher leakage current than the one with thickness equal to etching depth. We show this data in Figure 2.22

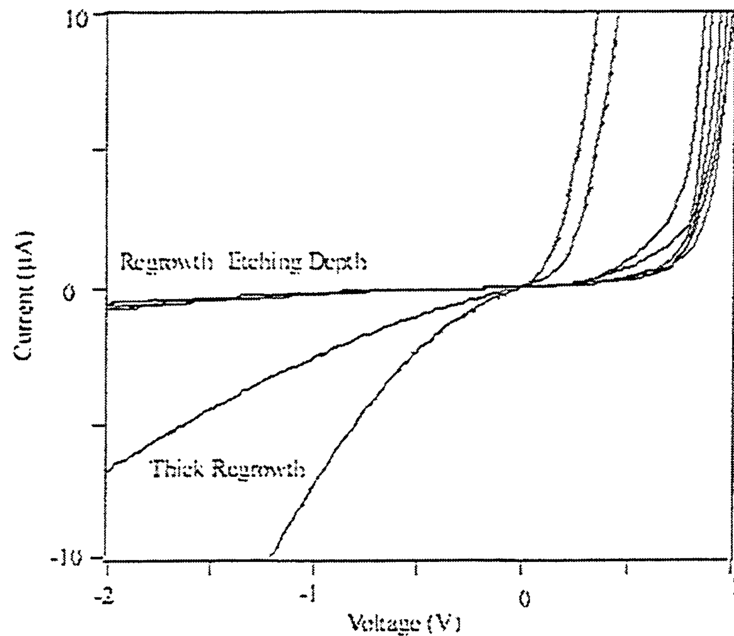

Figure 2.20 Characteristic for Thick CBL Compare to the Usual Thickness

We can see that we have to limit the thickness of the CBL to the etch depth and maintain low doping in one pn- junction to achieve low current. We do not demonstrate low (submilliampers) leakage current on devices made by wet etching, but very low currents are achieved with ECR etched samples [8]. In the next picture two sets of the Current-Voltage data for "unoptimized" and "optimized" devices are showed, so that we can clearly see difference. Usually we have less than 100µA leakage with only 4-10 Ohm resistance current for 1 mm long devices with the right CBL structures.

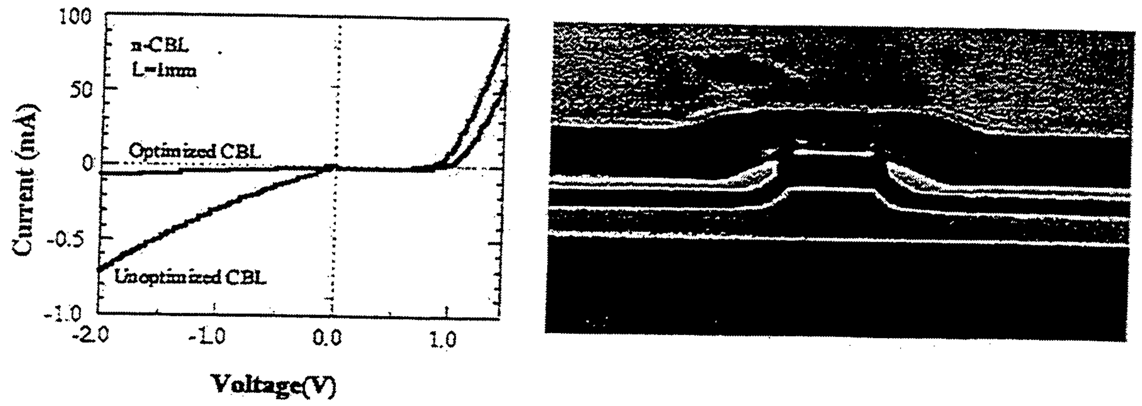

Figure 2.21 Cross-section for Optimized and Unoptimized Devices

2.8 Laser Testing

Typical device characteristics for broad [9] area lasers with three different compressive strains are presented here.

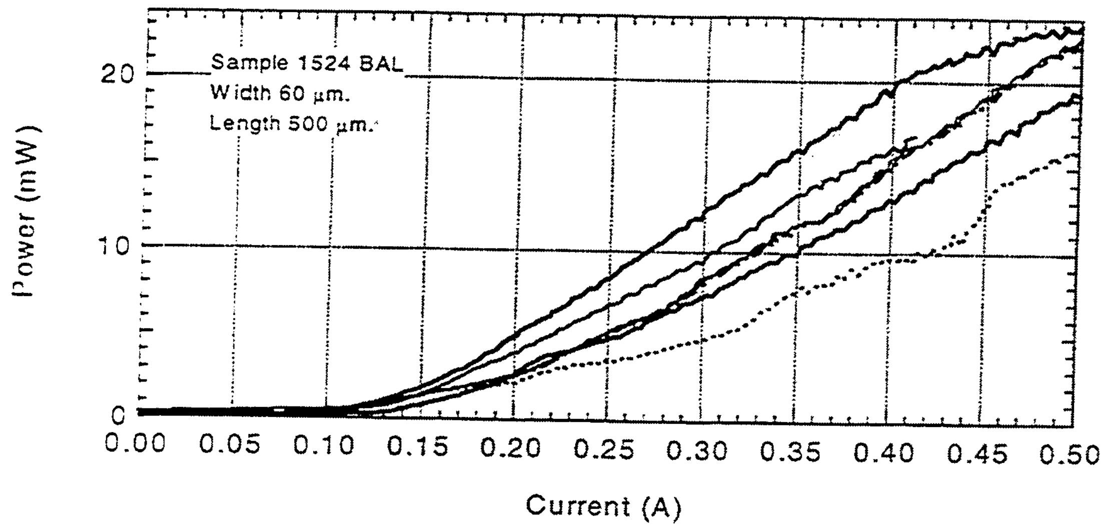

Figure 2.22 Typical Light-Current Data for Broad Area Lasers

Threshold current for these devices is around 120-150μA, which corresponds to a threshold current density of 400A/cm^2 (L=500μm) or 133A/cm^2 per well. We plot summarized data for different cavity length

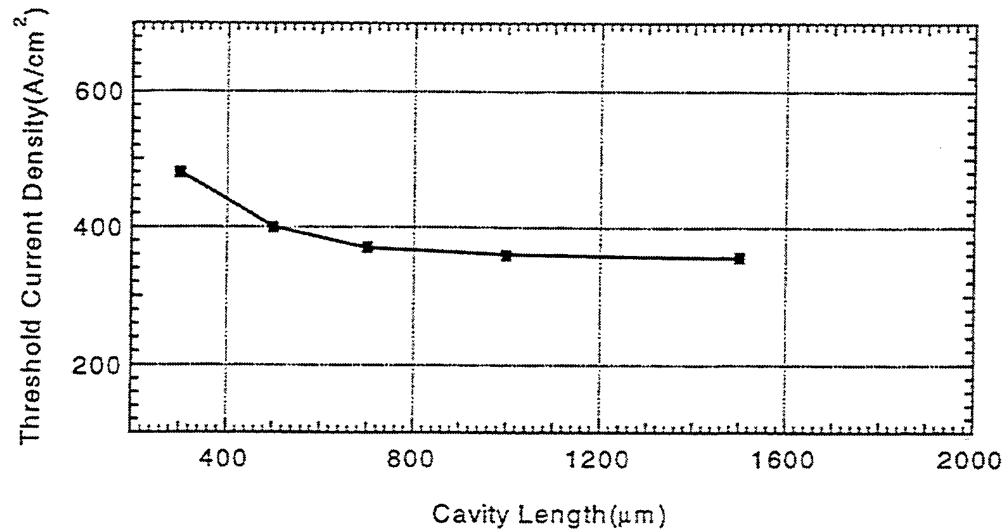

Figure 2.23 Threshold Current Density for Four Quantum Compressively Strain Well BAL

Near-field measurement, done on the same sample shows uniform emission below threshold and some filamentation above the threshold, as we can see on Figure 2.27

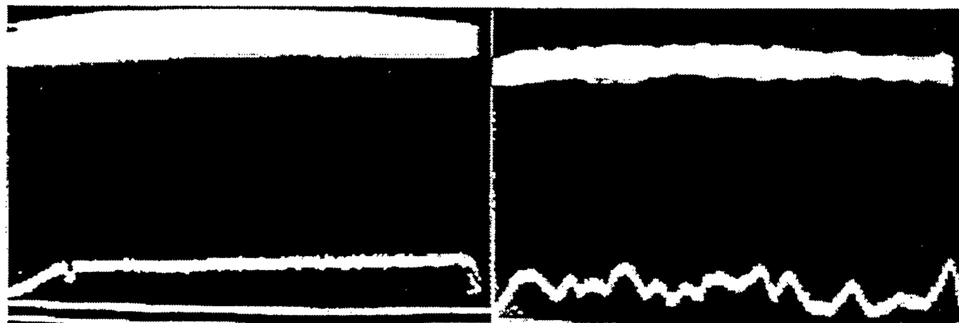

Figure 2.24 Typical Near Field Pattern from Broad Area Laser, Below Threshold (left) and Above Threshold (right)

Filamentation is a typical phenomenon in broad area lasers, due to the high number of lateral modes in wide waveguides [10]. We do not see this mode structure in single mode, ridge waveguide (RWG), laser devices, where the waveguide is supposed to support a single mode only. We can measure both near and far field data for ridge waveguide lasers, and because these are single mode devices we can easily relate one to another. The far field is the Fourier Transform of the near field [11], or we could use simple a gaussian approximation [12, 16],

$$\Omega_{th} = \frac{\lambda^2}{2\pi\omega_0^2}$$

where • 0 is the beam width and • th is the angular divergence.

Data for typical RWG devices is presented on Figure 2.24

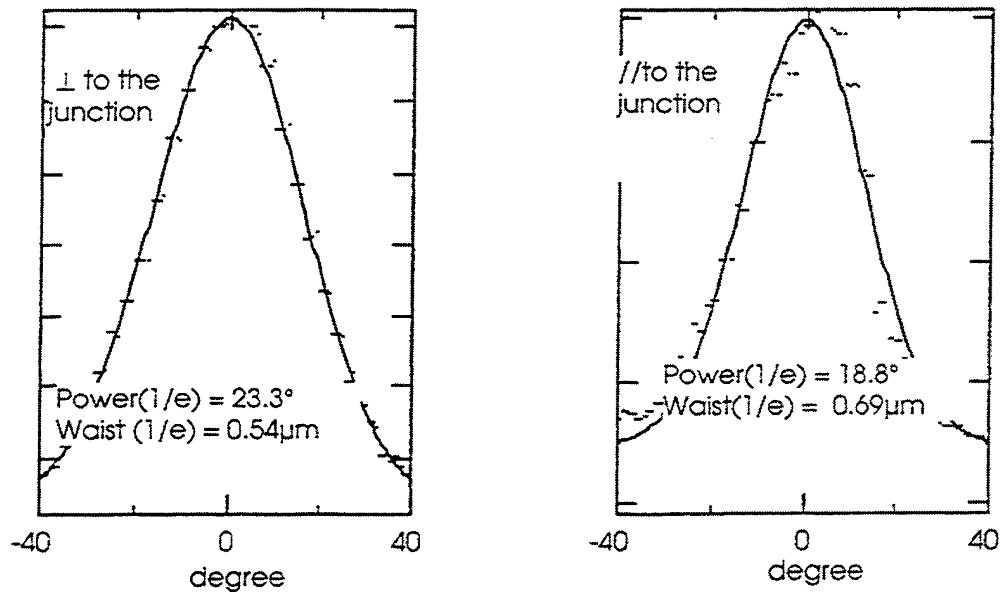

Figure 2.25 Far Field Measurements for RWG Device

From the divergence angle we have calculated the beam waist size, which was 0.54 μm perpendicular to the junction plane and 0.68mm at the plane. This data is in very good agreement with data obtained from near-field testing [17,18]. We have a tool to measure a spot size inside a laser waveguide, which could be useful for measuring mode transformation characteristics.

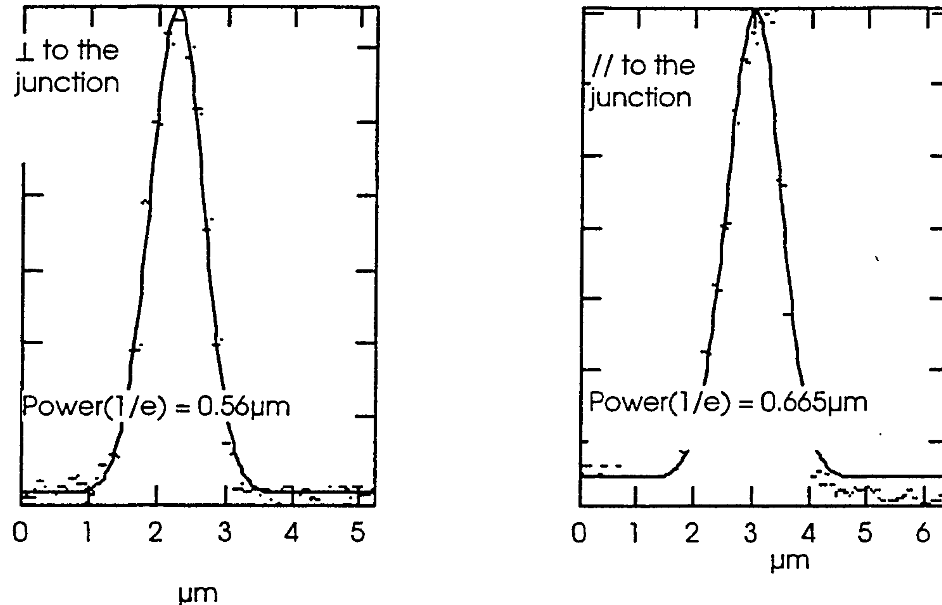

Figure 2.26 Near Field Data for the Same Device as the One Used for Far Field (Figure 2.24)

2.9 Conclusion

High performance lasers were demonstrated. RWG and BH devices were studied and optimized for threshold current. The modal gain and transparency current densities of the tensile and compressive strained lasers are close enough to make them suitable candidates for making polarization insensitive amplifiers which will be discussed in the next chapter.

References

1 Kushant Uppal PhD Dissertation University of Southern California 1997

2 J.Downes and D.A.Faux, J. Appl. Phys. 77, (1995) 2444

3 K. Uppal, D. Tishinin, I. Kim and P. D. Dapkus:" Study of 1.3μm tapered waveguide spot size transformers" JQE, Vol. 3 pp.975-980, 1997

4 T.L.Koch, U.Koren, G.Eisenstein, M.G.Young, M.Oron, C.R.Giles and B.I.Miller, IEEE Photon. Tech. Lett. 2, (1990) 88

5 C.Constantine, C.Barratt, S.J.Pearton, F.Ren and J.R.Lothian, Electron. Lett. 28, (1992) 1750

6 In Kim, D. Tishinin and P.D. Dapkus "Control of selective area growth and regrowth of InP on mesas by MOCVD using TBP"ICMOVPE IX, oral presentation.

7 K. Uppal, D. Tishinin and P. D. Dapkus: "1.3μm polarization insensitive tapered waveguide mode conversion structures with mixed quantum well active regions" LEOS 1996, oral presentation

8 T.Kambayash, C.Kitahara and K.Iga, Jpn. J.Appl. Phys., 19, (1980) 79

9 Atul Mathur, Ph.D. Dissertation, University of Southern California, 1995

10 Robert J.Lang, Anders G.Larsson and Jeffrey G.Cody, "Lateral modes of broad area semiconductor lasers:theory and experiment", IEEE J. Quant. Elec., vol. 27, no. 3, 1991

11 Siegman "Lasers" University Science book

12 G.P.Agrawal and N.K.Dutta, "Long Wavelength Semiconductor Lasers", Van Nostrand Reinhold, 1993

16.S.Kitamura, K.Komatsu and M.Kitamura, IEEE Photon. Tech. Lett., vol. 6, no. 2, pp 173-175, Feb. 1994

17.M.Joma, H.Horikawa, C.Q.Xu, K.Yamada, Y.Katoh and T.Kamijoh, Appl. Phys. Lett., vol. 62, no.2, pp 121-122, Jan. 1993

18. K. Magari, Mokamoto, H. Yasaka, K. Sato, Y. Noguchi and O. Mikami, IEEE Photn. Tech. Lett., vol.2,no.8, pp 556-558, Aug. 1990

Chapter 3

1.3μm Polarization Insensitive Amplifiers with Integrated Mode Transformers

3.1 Introduction

Semiconductor optical amplifiers are important elements in DWDM systems. Their small size, high gain, and high efficiency are key characteristics. High gain, bandwidth, and saturation along with polarization independent gain are minimum requirements for using an amplifier in single mode fiber optical networks. One of the main problems is that semiconductor optical amplifiers are quite expensive. This is mainly due to packaging costs, which involve active alignment to couple light in and out of the chip. Low-loss coupling of semiconductor optical amplifiers to cleaved single mode fibers with large alignment tolerance will simplify and reduce the cost of optoelectronic devices. A typical single-mode edge-emitting laser/amplifier has a 2μm lateral waveguide width with submicron thickness. This results in a highly elliptical mode with a 1-2μm size, having a 30-40° divergence angle [1]. Single mode fiber (core diameter about 9μm) has a divergence angle of less than 10°, so there is a big mode mismatch between the input/output fiber and the amplifiers. This results in high coupling losses and low alignment tolerances.

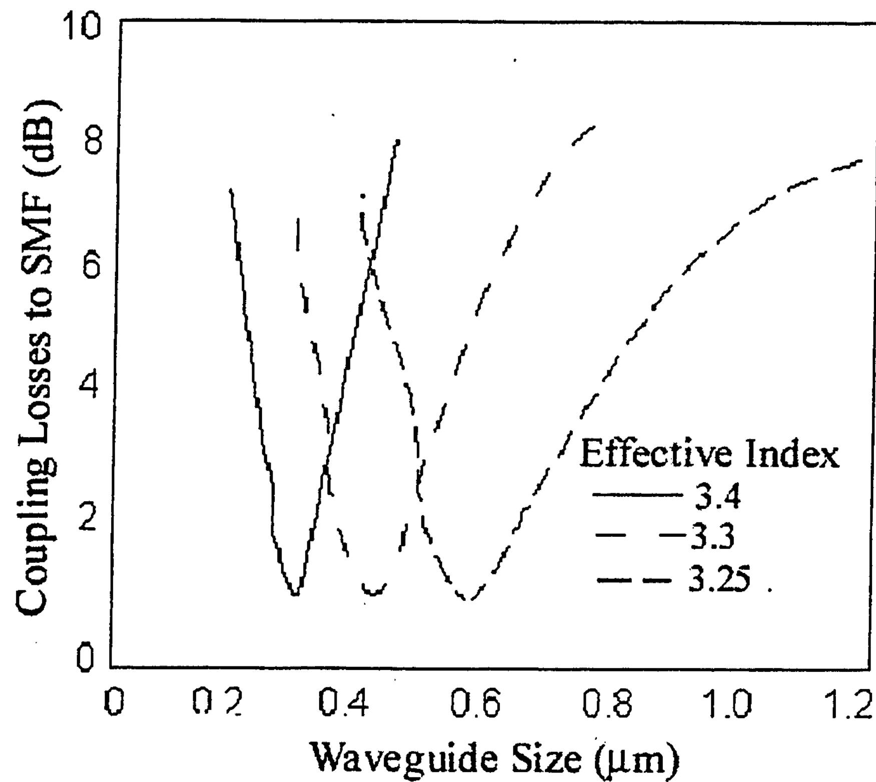

Figure 3.1 Coupling Loss vs. Diameter of the Guiding Core

To overcome these problems we have used a complex lens system to transform the beam and improve coupling. Each element has to be positioned and aligned separately. The other approach is to modify the mode inside of the waveguide, by expanding it and providing better matching to the fiber mode [2]. This monolithically incorporated section should transform the mode from the highly confined, elliptical laser mode to a larger, circular mode. The mode would thus be better matched to the beam profile inside the single mode fiber. This mode transformation region should also preserve the mode polarization state so that it comprises a polarization insensitive device. Several mode transformer designs were proposed and investigated. Selective area growth was employed to make the vertically tapered devices [3,4,5].

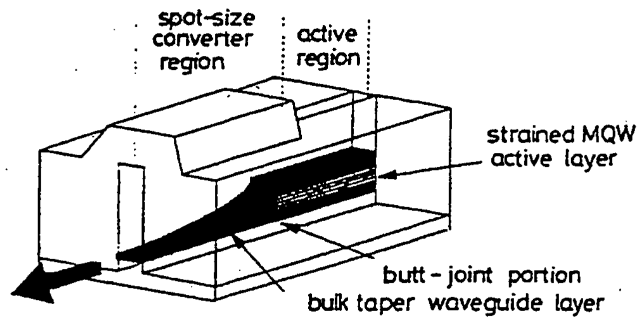

Figure 3.2 Selectively Grown Structure with Mode Transformer Region

In this approach, the sample was patterned before active region growth. Due to material migration, the growth rate was enhanced near the protected area. Thin waveguides in the input/output areas promotes mode expansions. This approach has an inherent problem: due to difference in surface migration, not only thickness, but also composition of the waveguide quantum well will change. This in turn will result in modification of the polarization state for the propagating light. Thus this solution is not suitable for making polarization insensitive devices. Another option is to use a passive waveguide, which is typically placed underneath the active one, so the travelling wave will be forced into the passive waveguide by the laterally tapering, upper active waveguide [6,7,8].

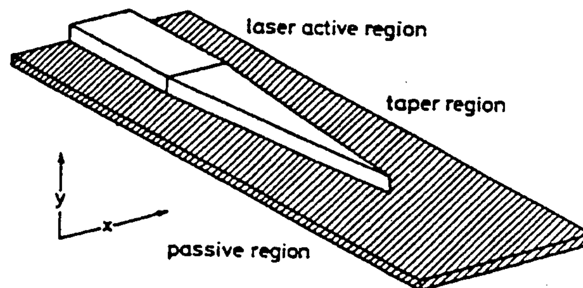

Figure 3.3 Schematic Diagram for Mode Transformation Done with Passive Waveguide

In this case we have to make both waveguides polarization insensitive with symmetric coupling regions to provide equal coupling for both modes. It is generally a very complicated technical problem to optimize all elements is such a system simultaneously in order to preserve the polarization state for the propagating light.

We chose a laterally tapered waveguide region, which is a convenient solution since it is easily implemented by means of standard semiconductor technology [9]. In this case our waveguide is the same up to the edge of the sample and the gain can be adjusted to preserve polarization even in the tapered section. Laterally tapered sections allow us to expand the mode inside the waveguide by reducing optical confiment [4].

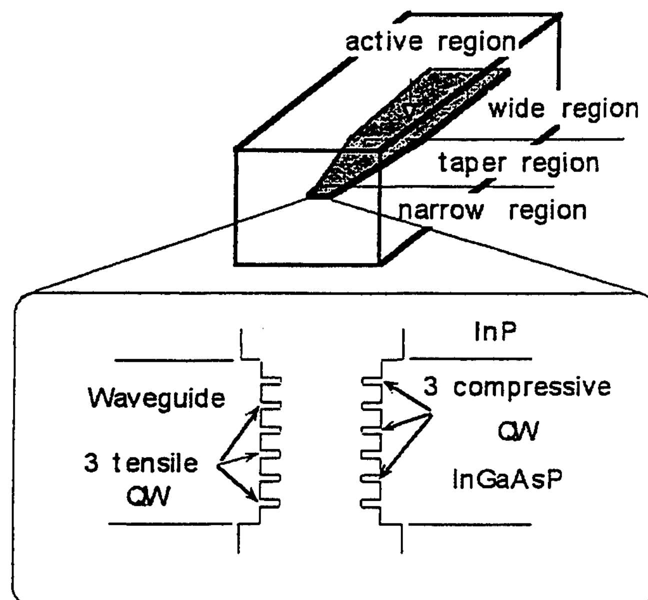

Figure 3.4 Lateral Taper Waveguide with Mixed Quantum Well Structure

If we taper the waveguide below its critical width it is clear that we loose confinement and therefore mode size should increase [10]. Simple effective index

calculations show that below 0.7μm, divergence angle change is almost inversely proportional to waveguide width.

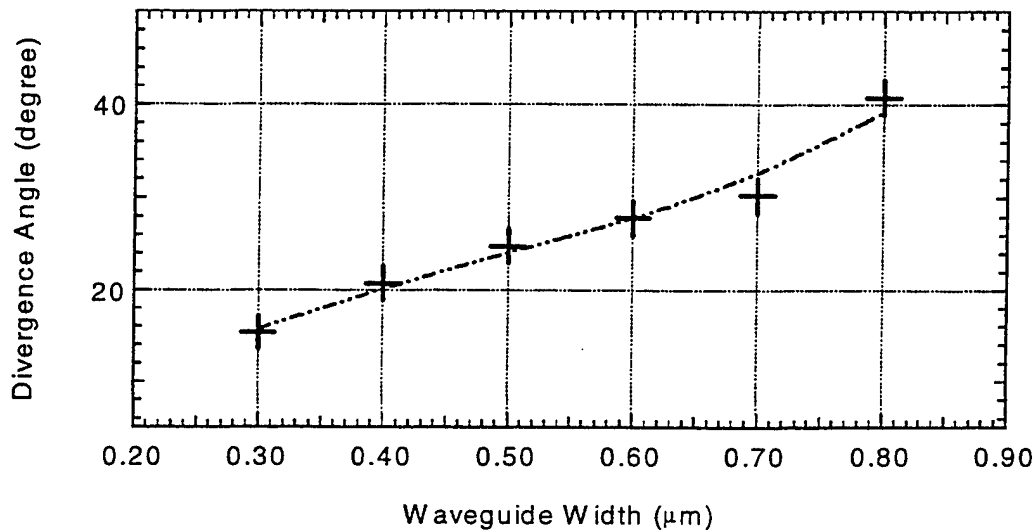

Figure 3.5 Far Field Divergence angle vs. Waveguide Width for 0.3μm Thick Waveguide

Hence, we can see that it is easy to change the mode size if we are able to fabricate a waveguide with sub-micron dimensions. We have described in Chapter 2 a novel fabrication technique, allowing us to accomplish this.

3.2 Fabrication

A low-pressure Thomas Swan MOCVD system was used to grow the structures used in this paper. Growth was done on (100) n+-InP substrate at a temperature of 640°C and a pressure of 76 Torr. The InGaAsP active region consists of three 65Å, 1% compressive strained quantum wells and three 100Å, 1% tensile quantum wells, separated by 200Å, lattice matched barriers (λ = 1.05μm) buried in the bulk InP layers. The active region, shown schematically on Figure 2.4, has two sections: a 500μm long linear gain region where light is tightly confined and a mode transforming section, which includes a

200 μm long laterally tapered region and an ~25 μm narrow output region. The width of the waveguide in the tapered region varies from 2μm (wide end) to ~0.5μm (narrow end).

For polarization insensitive devices, gain for TE and TM modes has to be equalized. We can use a bulk, double heterojunction active region, which gives us the same gain for TE and TM modes, but in this case we have to match confiment factors to have the same chip gain. A square waveguide has to be employed to achieve the same chip gain for TE and TM modes, which is impossible to implement in our tapered design. A mixed strain quantum well was used instead to provide gain for both polarization directions in this set of samples.

It was shown [11] that lasers, utilizing strained quantum well regions generally have superior performance compared to double heterojunction devices in many aspects: higher gain, high bandwidth, and faster response time. Light and heavy hole degeneracies are removed by introducing strain into the quantum well. Compressive strain promotes transitions to heavy hole bands and tensile strain makes the light hole level the ground level.

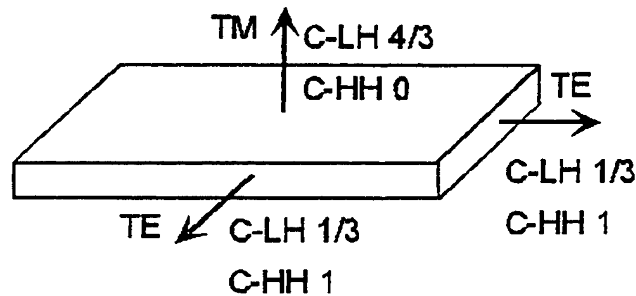

Figure 3.6 Optical Momentum Matrix Element for the Electron is Overlap with Light Electric Field Vector for Different Directions

The optical momentum matrix element, **M**, is modified due to changes in the ground level hole momentum. Compressively strained lasers emit only TE light and in

tensile strained devices the TM mode dominates. Devices with mixed quantum wells show lasing in both polarization directions and we can see kinks in the light vs. current data.

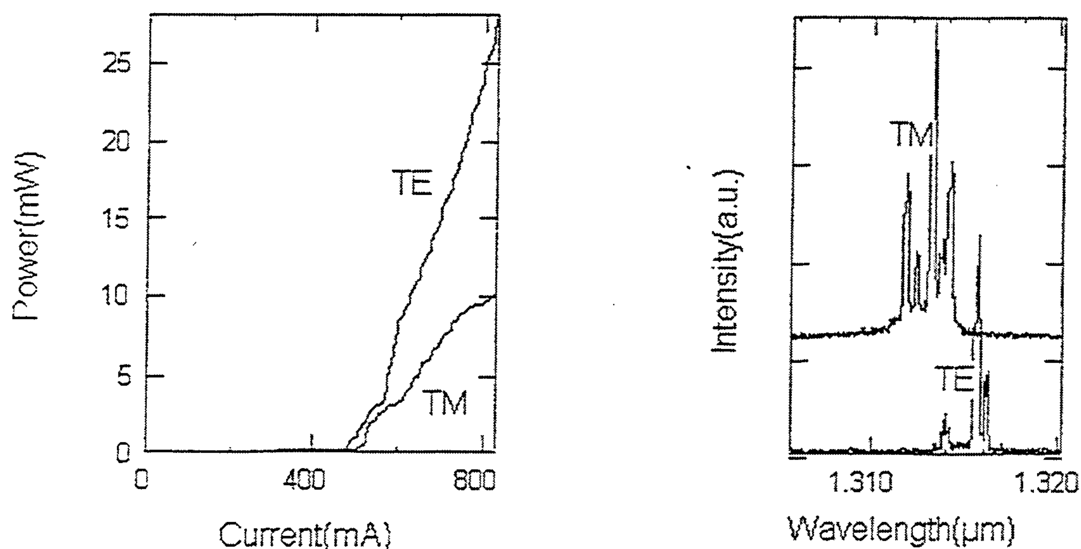

Figure 3.7 Light vs. Current for Different Polarizations in Broad Area Laser with Mixed Quantum Well; Right Picture Presents TE and TM Spectrums for the Same Laser

To fabricate the buried heterostructures devices, we perform 2 growth runs. First, we form the active region with an InP and an InGaAs layer on top. Compressive and tensile strained quantum wells were optimized separately to achieve overlap of transverse electric (TE) and transverse magnetic (TM) emission peaks by using a novel edge-photoluminescence technique [12]. We chose to have 3 tensile and 3compressive quantum wells. Compressive wells were 60Å thick with 1.1% compressive strain. The tensile wells were 100Å thick with 0.9% strain.

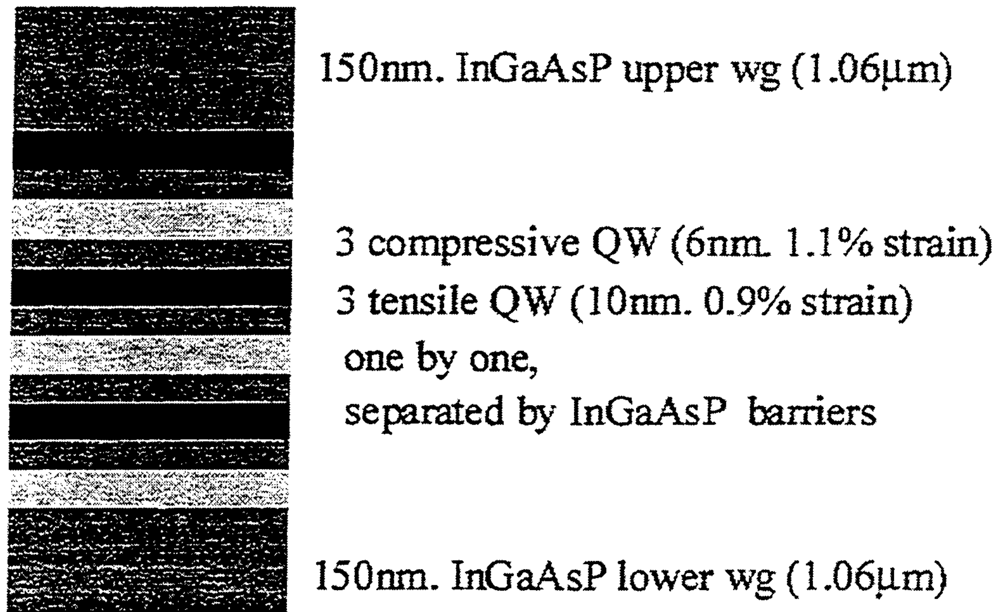

Figure 3.8 Waveguide Structure for the Amplifier Sample

The sample was then patterned, using standard photolithography, and the InGaAs layer was selectively etched and undercut beneath the mask to obtain the desired waveguide width in each section as was discussed in Chapter 2. The InP layer was then selectively etched using the InGaAs as a mask to achieve a smooth, vertical wall profile. This method provides excellent control of the waveguide width and provides low scattering losses at the same time. Finally the mesa width was transferred to the active layer by ECR etching (appendix A).

The regrowth included an InP cladding layer and a InGaAs cap layer. After this, a 10μm wide and 3 μm deep mesa was formed over the buried waveguide to provide better coupling to a single mode fiber [13]. The sample was then processed by standard laser fabrication techniques to provide contacts and output facets. The sample was cleaved into approximately 700 μm long bars, with the mode transforming section on the output end only. We chose this design so that we could compare coupling losses from the output

of the mode transformer and direct coupling losses to the linear region on the same chip. After basic laser testing (I_{th}=35-50 mA, wavelength -1340-1345 nm), we mounted the laser bars with p-side up on copper blocks for antireflection coating.

3.3 Antireflection Coating

Antireflection coating deposition is a very important step in fabrication of a traveling wave semiconductor optical amplifier. Reflectivity has to be under 10^{-4} to achieve less that 1 dB gain ripple. Several techniques were used to reduce facet reflectivity for a laser diode: angle–facet structure, window facet structure, and antireflection coating (either single layer or multiple layers).

The angle–facet structure design [14] can be done by defining a waveguide stripe at an angle to the cleaved plain.

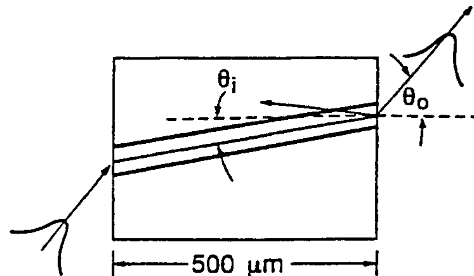

Figure 3.9 Angle Facet Amplifier Structure

In this design we reduce coupling back to the waveguide by tilting it with respect to the input/output facets. The reflected wave does not couple back to the waveguide due to differences in the angle of propagation. The main disadvantage of this structure is chip input coupling difficulty. The output angle in the air due to Snell's Law is

$$\sin(\Theta_o) = \sin(\Theta_i)\frac{n_i}{n_o}$$

To get low (10^{-4}) reflectivity we need to have Θ_0~ 3-7^0, which makes it very hard to couple light in, due to the high angle in the air, which is 9-20^0.

Window facet structure uses a window between the end of the waveguide and cleaved facet. This unguided region expands waves by reducing back reflection to the waveguide.

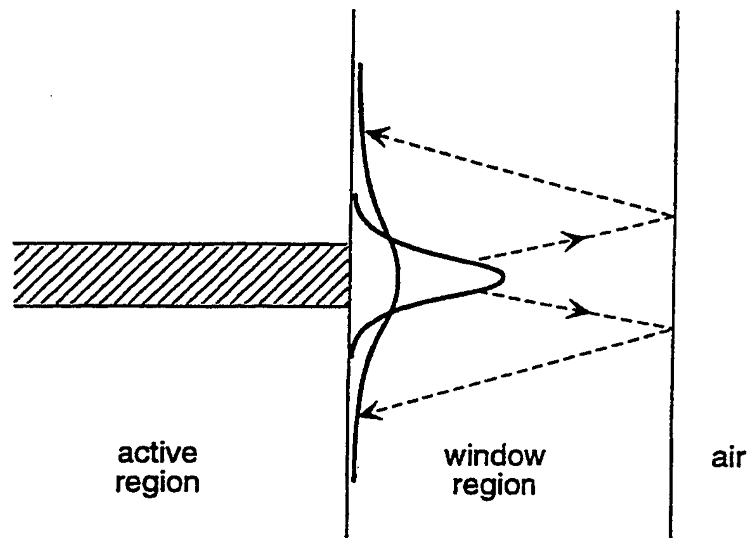

Figure 3.10 Window Facet Structure Principal Design

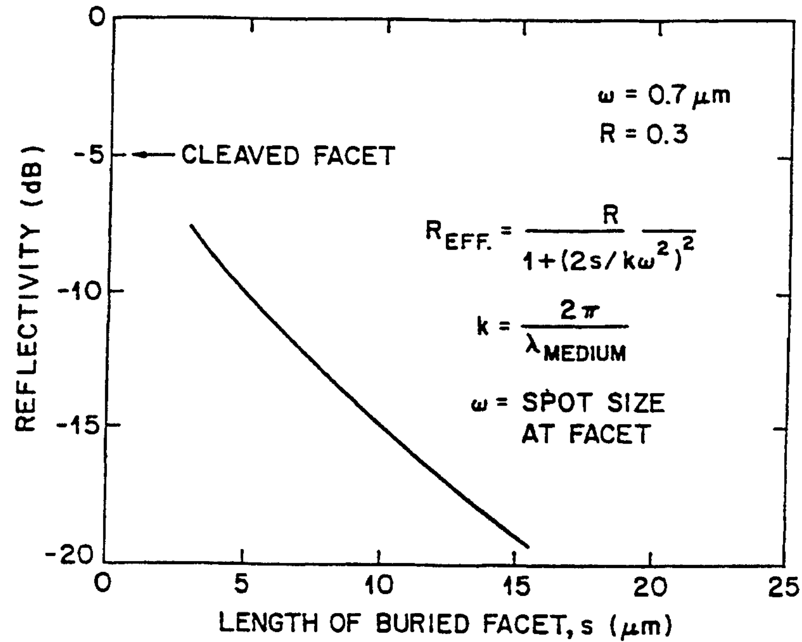

Figure 3.11 Effective Reflectivity as a Function of Buried Region Length

Effective reflectivity in this case depends on the windows region length. We can see from this graph, that in order to achieve low reflectivity (-40dB) we need to make separation very wide (if possible at all).

The most common approach to obtaining low reflectivity is an antireflection coating. It enables very low reflectivity (-60dB) with low losses and low polarization sensitivity. This procedure is easily compatible with any of the previous methods to reduce reflectivity even further.

3.4 Low Reflectivity Coating

Applying antireflection coating on the laser diode facets is a widely adopted method to obtain traveling wave semiconductor optical amplifiers [15]. The simplest

approach to calculate thickness and index is to make a plane wave approximation. In this case thickness is $\frac{\lambda}{4n_{ar}}$ where index is $n_{ar} = \sqrt{n_{eff}}$

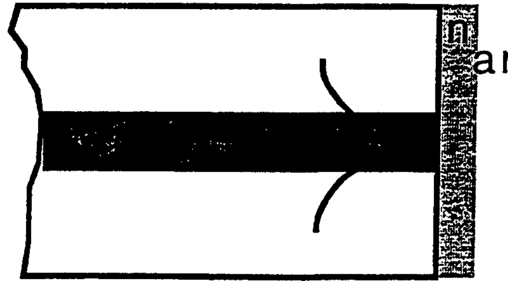

Figure 3.12 Single Layer Antireflection Coating

This approximation works well for plane wave, but in the case of the guided wave, which we have, we need to do more complicated analysis, as we will demonstrate later. We want to take into consideration the finite mode size and divergence. [16]

To start we approximate the waveguide mode as:

$$E_{inc}(x) = \begin{cases} A\cos(dh_a/2)\exp[h_c(d/2-x)], _d/2 \leq x \\ A\cos(h_a x), _-d/2 \leq x \leq d/2 \\ A\cos(dh_a/2)\exp[h_c(d/2+x)], _x \leq -d/2 \end{cases}$$

where

$$h_c^2 = \beta^2 - \kappa_c^2$$
$$h_a^2 = \kappa_a^2 - \beta^2$$

here, β is a propagation constant and $k_{a,c} = 2\pi/\lambda_{a,c}$ are phase constants in the diode. "A" and "C" represent active and cladding region, respectively. The boundary condition at the waveguide interface is: $h_c \cos(dh_a/2) = h_a \sin(dh_a/2)$

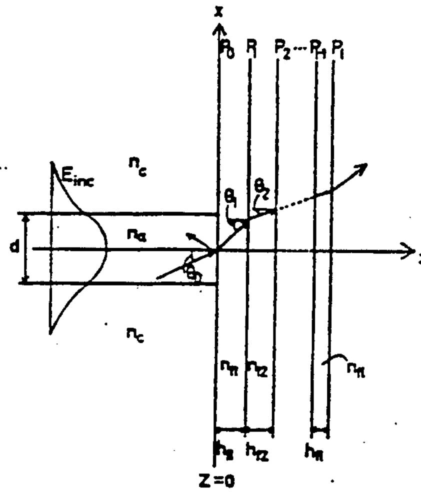

Figure 3.13 Model for Multilayer Laser Diode, Used in Analysis z<0-waveguide and z>0 AR coating layers

We can calculate an angular spectrum for the waveguide mode at the region

$$F_{inc}(\Theta)=\int_{-\infty}^{d/\infty} E_{inc}(x)e^{(i\kappa_a n_{eff}\sin(\Theta_0 x))}dx$$

where z>0. In this region the wave propagates through a layer used for an antireflection coating. The wave in this region is not guided, so we can treat each plain wave independently.

The Fresnel Reflection coefficients for AR coatings are

$$r(s)=\frac{(m_{11}+m_{12}p_{l+1})p_0-(m_{21}+m_{22}p_{l+1})}{(m_{11}+m_{12}p_{l+1})p_0+(m_{21}+m_{22}p_{l+1})}$$

Where:

l is the layer number (in our case it is 1 only)

$p_i=n_i\cos(\Theta_i)$ where n_i is an index for layer number I

m_{ij} is an element of characteristic matrix $M=M_1*M_2*\ldots M_l$ so,

$m_{11}(j) = m_{22}(j) = \cos\gamma_i$

$m_{12}(j) = -\frac{i}{p_j}\sin\gamma_j$

$m_{2i}(j) = -ip_j \sin\gamma_j$

$\gamma_j = 2\pi h_j \cos(\Theta_j)/\lambda$ is an propagation angle inside the AR coating layer

h_j is a thickness of the layer

We can solve this Fresnel equation for each plane wave, exactly like in a VCSEL case and after propagating through the AR coating layer/layers we can get a reflected wave through an inverse Fourier transform.

Reflectivity in that case can be found like

$$R = \frac{\left|\int_{-\infty}^{\infty} E_{inc}(x)E_{ref}(x)dx\right|}{\left|\int_{-\infty}^{\infty} E_{inc}^2(x)dx\right|}$$

We have done this calculation for our devices and Figure 3.15 presents the results.

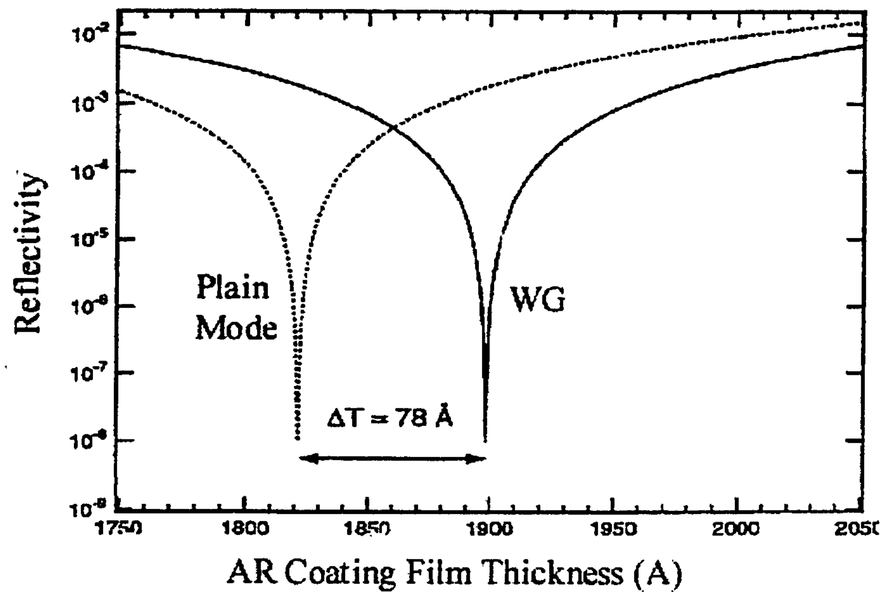

Figure 3.15 Calculation for Single Layer AR Coating, Results for Plane Wave Approximation and Guided Wave Calculation on the Same Graph

We can see from this calculation that the simple index approximation is not accurate enough to get $10^{-4} - 10^{-5}$ reflectivity. The difference between minimum in reflectivity is 78Å and due to guiding effects the real layer thickness has to be higher. This data shows that even with a single layer coating (which is easier to implement compared to multilayer structures) we can achieve very low (10^{-8}) reflectivity with the right index and thickness.

3.5 Single Layer AR Coating, Fabrication

Single layers of non-stoichiometric SiO_x were deposited on both facets. The refractive index of this material can be adjusted in the range from 1.5 to 1.9 by varying the oxygen composition of the deposited oxide. The index has to be $\sim 1.802 \pm 0.011$ to achieve reflectivities below 10^{-4}.

We used an e-beam deposition system where SiO (silicon monoxide) was used as a target for deposition. Material deposited on the sample was non-stoichiometric oxide due to partial oxidation as a result of reaction with oxygen in the deposition chamber. We initially used background oxygen pressure to correct the index, however there is always some oxygen inside the chamber as a part of background gases.

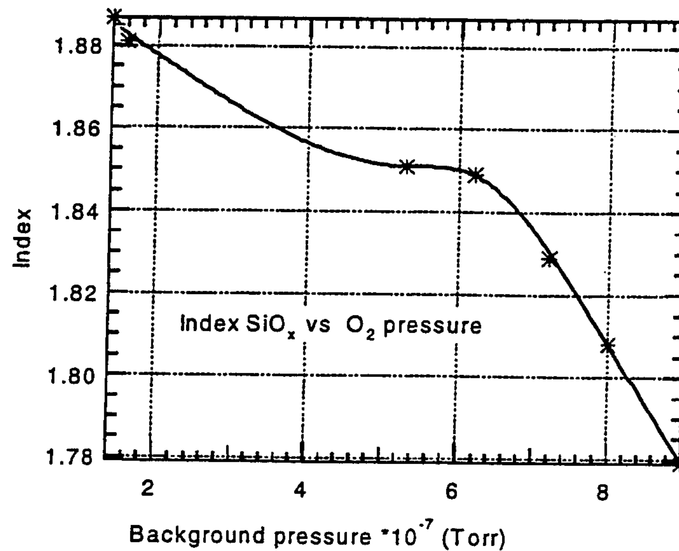

Figure 3.16 Index as a Function of Background Oxygen Pressure

We can see that the index varied almost linearly with background pressure. It is very hard to control the index precisely, so it was not reproducible from run to run. We can get it close but the accuracy needed to get a low reflectivity was almost impossible to achieve.

We also can introduce oxygen within the deposition chamber artificially. It works the same way, reducing the index of the deposited film. In this case, first we have to evacuate the chamber to the minimum achievable pressure, so that the index of deposited material is the maximum if there were no additional oxygen introduced. Then, after starting deposition, we introduce additional oxygen to reduce the index to the desired value.

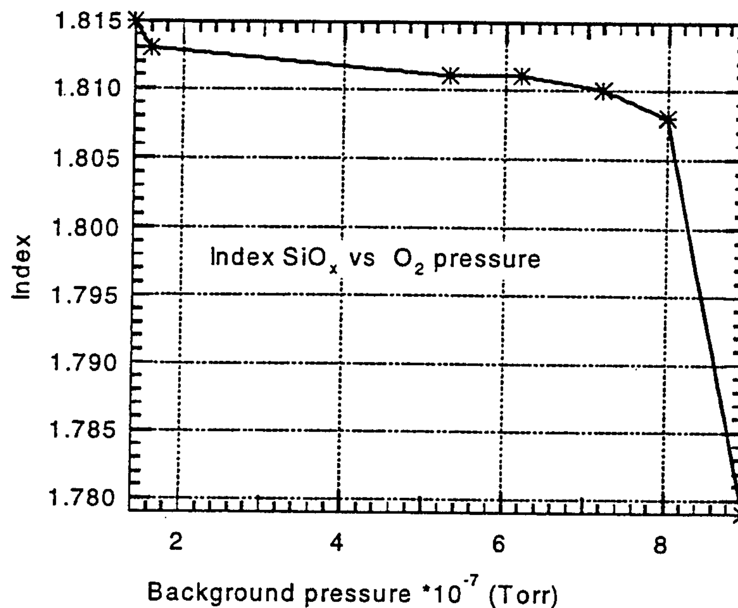

Figure 3.17 Index as a Function of Initial Pressure with Additional Oxygen Filled to $2*10^{-5}$ level

We can see first that additional gas pressure has to be much higher than the background pressure to reduce the index. We believe that this is due to the fact that we have not filled the evaporation chamber uniformly. Oxygen from the gas inlet, which was close to the pressure monitor, did not spread uniformly over the chamber, reducing the "interaction distance" between the gas and the evaporated material. We should also note that at low background pressure, the index does not depend on the initial pressure.

Several *in situ* monitoring schemes were proposed. Ellipsometry was used within a deposition chamber to monitor the index and thickness [17], while electrical diode characteristics were used [18] to monitor device losses.

Active laser power monitoring was used to get the right thickness. The idea behind this is to make a deposition on one facet and monitor the output power from the opposite facet. Threshold current of a laser diode is:

$$J_{thr} = \frac{1}{\beta}\left[\alpha + \frac{1}{2L}\ln\left(\frac{1}{R_b R_f}\right)\right],$$

where R_b and R_f are the reflectivity for front and back facet respectively. β is the gain factor, α the internal loss, and L is the length of the chip.

Threshold current should go up as the facet reflectivity decreases. Power emitted from back facet should thus go down because of two reasons. First, the threshold current is increasing. Output light is proportional to $|I_{pump} - I_{thr}|$, thus the output light should decrease. Second, the amount of light coming from the facet is inversely proportional to the facet reflectivity, so the relative amount of light coming from the back facet is decreasing. Thus a minimum of reflectivity corresponds to a minimum amount of light emitted from the back facet. Hence by monitoring the light output we can obtain optimal coating layer thickness even if we have variations in the index during deposition.

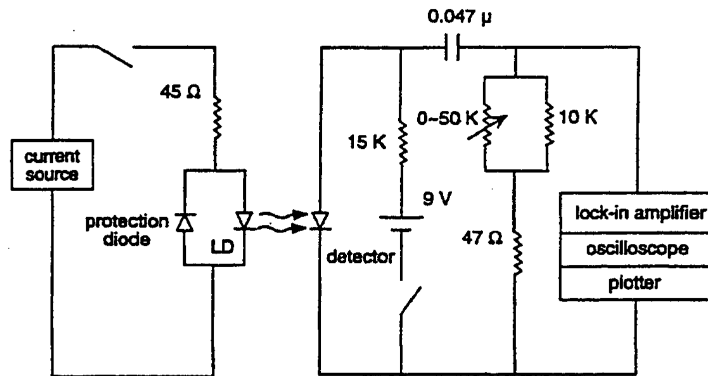

Figure 3.18 Schematic Diagram for a Circuit Used for Active Reflectivity Monitoring

For active reflectivity monitoring, we used a current source to generate pulsed current through the coated diode. A protection diode was used to limit possible reverse

voltage and a resistor was used to match the load impedance. A standard, reverse biased photodiode was used as a detector. The lock-in amplifier was used to demodulate and remove noise from the output signal. Output from the lock-in amplifier was recorded as a function of time, thus we can see a change in the output signal (and therefore reflectivity) in time. A plot of the output signal is presented in Fig. 2.19. An oscilloscope was used only to visually check the circuit and adjust the variable resistance to maximize the signal.

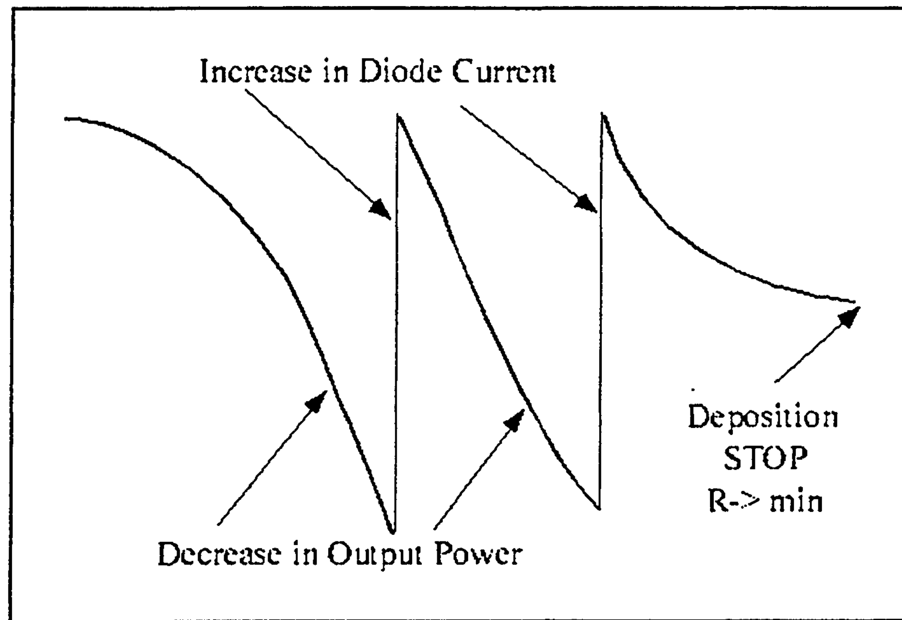

Figure 3.19 Trace Recorded form First Facer Deposition

We can coat the entire bar, mounted on a copper block, during the same deposition.

Results for one bar with 6 laser chips are presented in the next figure:

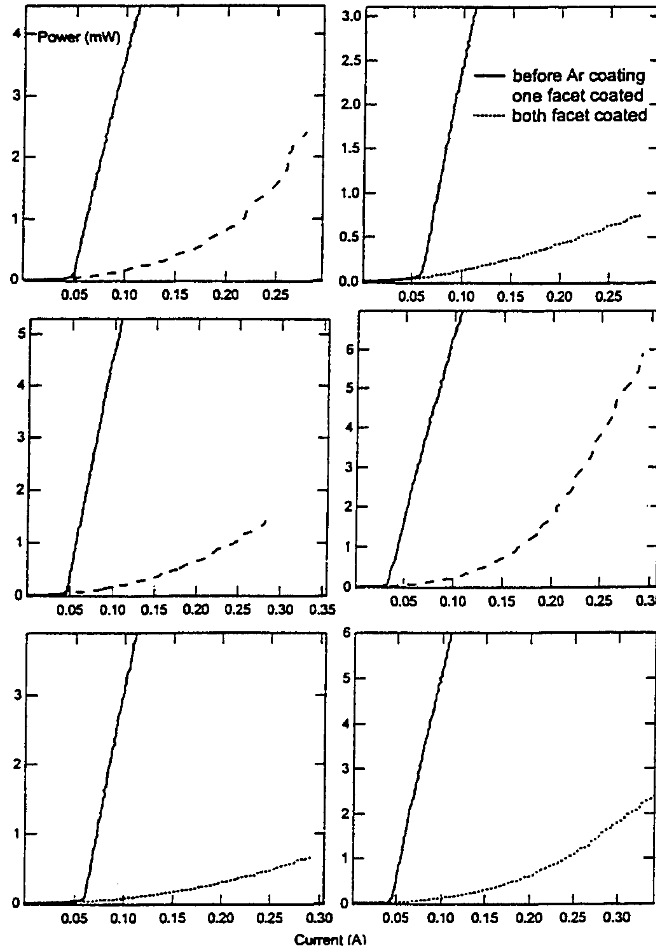

Figure 3.20 Light-Current Data for 6 Lasers' Coated Together on the Same Bar

We can see that after both facets are coated, we can pump chip up to 10 times threshold and it still does not lase. Spontaneous emission is also a good indicator for the quality of an antireflection coating.

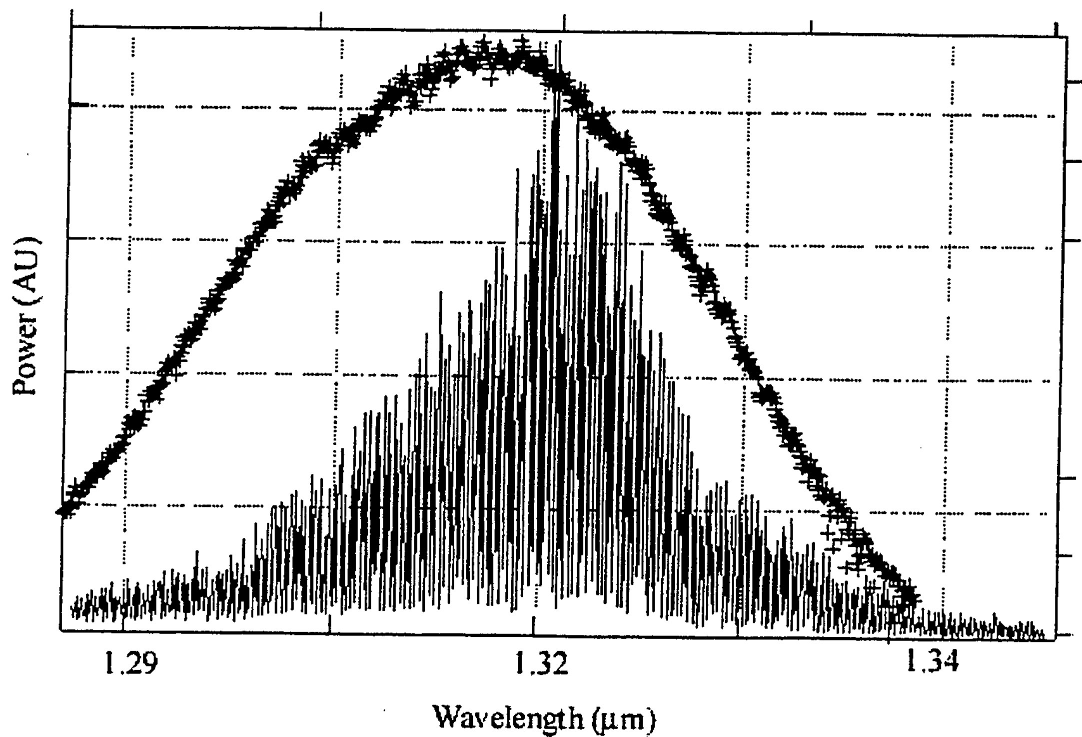

Figure 3.21 Spontaneous Emission Spectra for Laser before and after AR Coating

We can see that Fabry-Perot ripples in the reflectivity were significantly reduced. The maximum for the emitted light is also shifted to the high-energy side, due to band filling effects.

We used active monitoring of the laser light inside the chamber to control final thickness of the film. The residual reflectivity can be estimated from the gain ripple.

$$G(v)=\frac{(1-R_1)(1-R_2)G_s}{\left(1-\sqrt{R_1R_2}G_s\right)^2+4\sqrt{R_1R_2}G_s\sin^2[\pi \quad (v-v_0)/\Delta v]}$$

Where:

G_s is the small signal gain,

$R=\sqrt{R.R.}$ is an average reflectivity, and R_i is a facet reflectivity.

We measured small signal gain and did a curve fitting, as shown in Figure 3.22

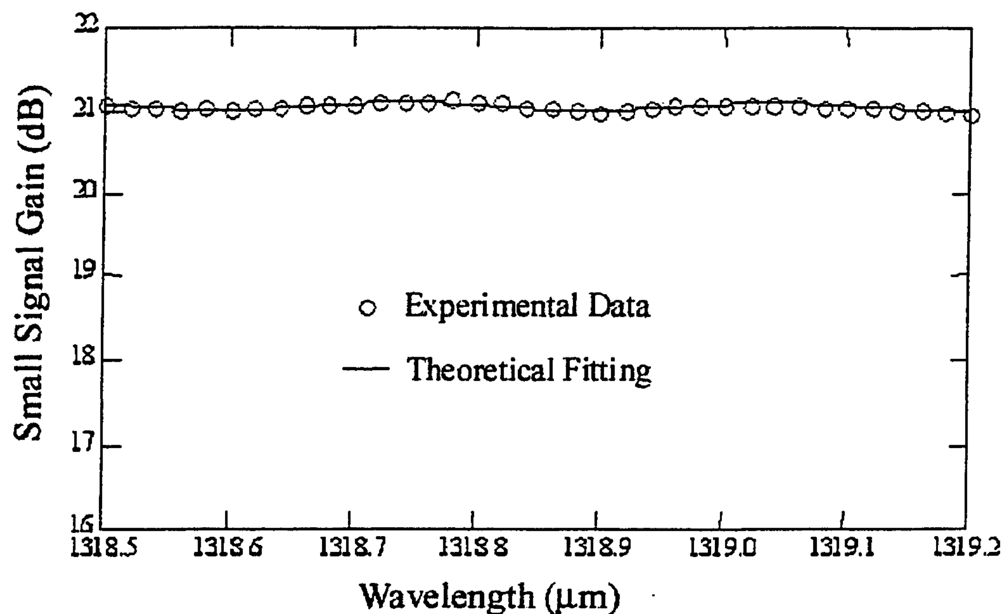

Figure 3.22 Theoretical Fitting of the Experimental Data to Calculate a Reflectivity

From the curve fitting we found that estimated reflectivity was on the order 5-10 x 10^{-5}, which corresponds to ripples of less that 0.2dB with 20 dB small signal gain.

The properties of the resultant amplifier chips were then tested. We used a Nd:YAG laser with center wavelength around 1.319 μm coupled to a polarization-maintaining (PM) fiber as the light source. Using only a PM fiber at the input lets us control the input light polarization and allows switching between TE and TM modes. We used both bulk and fiber optics for the output. Pulsed operation was chosen to minimize heating of the chip during testing. We used a 10 kHz repetition rate and 500 ns pulse duration. A boxcar integrator was used to extract the output signals.

First we measured transparency current (gain=1), to determine coupling efficiencies. Input light was modulated and we measured the induced voltage amplitude and phase between input light and photo-voltage.

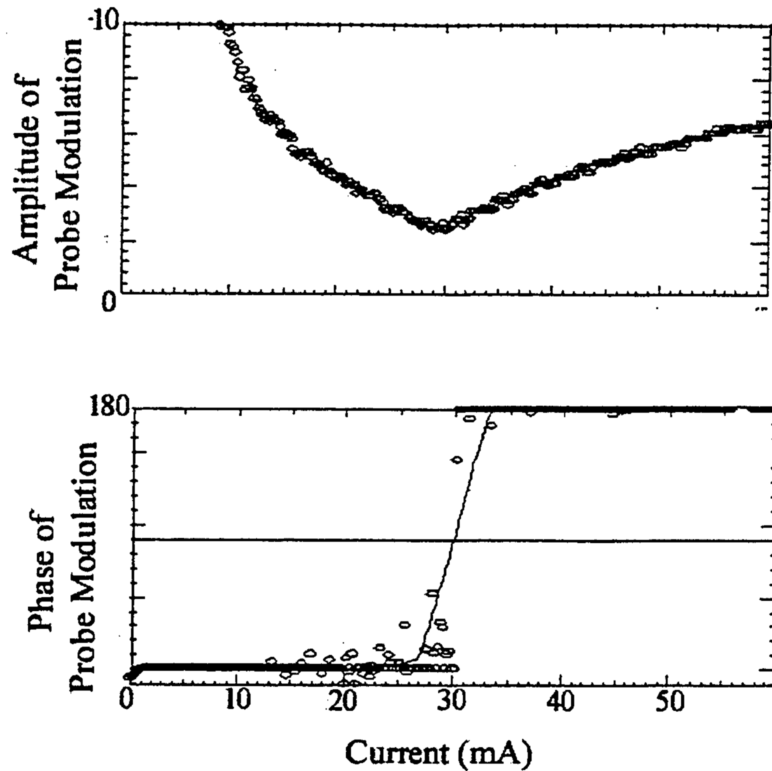

Figure 3.23 Amplitude and Phase of Induce Voltage Generated on the Chip as a Result of Input Light Modulation

We can see that we go from the absorption region at low pumping current to the gain region with a current above transparency. Photo induced voltage has a minimum at the transparency current, because propagating light does not suffer any losses or gain during propagation. Phase changes between the input light and the induced voltage also changes from in-phase at the absorption region to out-of-phase when we have positive gain in a device.

3.6 Results and Discussion

The reason for incorporating a mode transforming section in the amplifier is to improve coupling efficiency and reduce alignment sensitivity for coupling to cleaved, single mode fibers. To make the tapered waveguide a practical structure we have to loosen alignment tolerances and improve coupling. Using our design, we have measured coupling efficiency from the tapered end to a cleaved single mode fiber with a 9 μm core diameter to be 25%, which is about a 3-4 dB improvement compared to coupling to the un-tapered end (~ 8-10%). In figure 2 we show the measured alignment tolerance for coupling to this fiber.

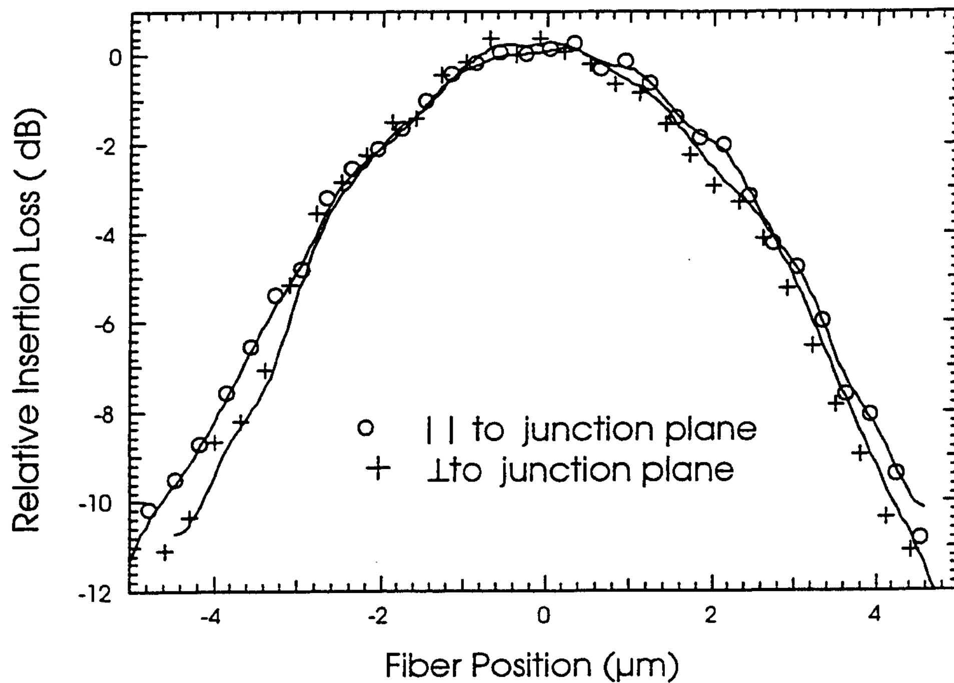

Figure 3.24 Alignment Tolerance to Single Mode (9μm core diameter) Fiber

The alignment tolerance is found to be 2.5 μm (at -1 dB level) regardless the direction of fiber motion. This suggests that the mode transformation has been successful and that a nearly circular beam has been formed at the output facet. This has been independently confirmed by far field measurements on uncoated laser samples.

The chip gain was measured using a polarization maintaining fiber at the input with either TE or TM polarizations and both fiber and free space optics at the output. Figure 3 presents the measured chip gain for both TE and TM polarization as a function of pumping current. The maximum unsaturated gain achieved with these devices was 18 dB at a current of 180 mA. Over the entire range of currents the gain difference between TE and TM modes is less than 1 dB.

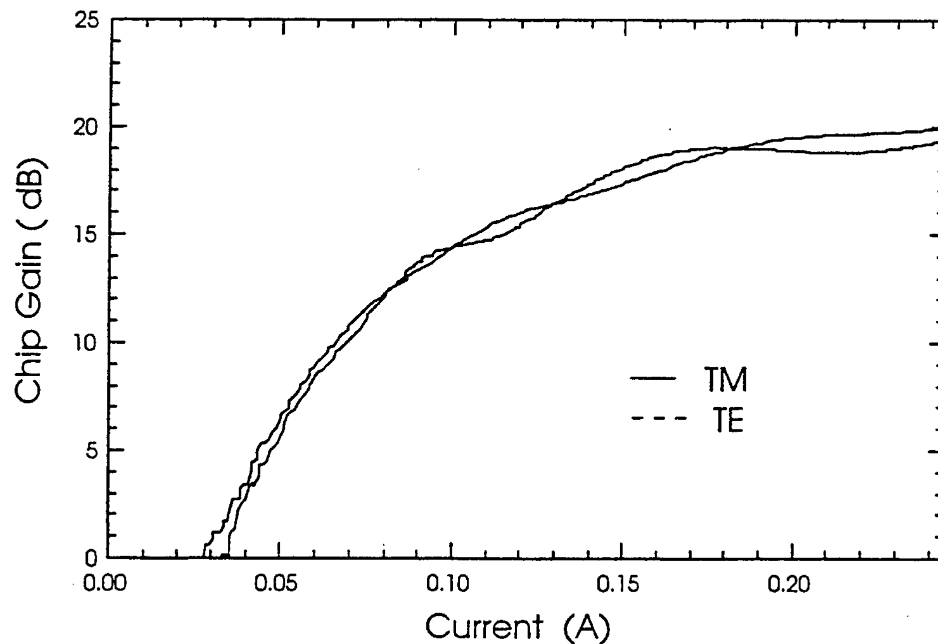

Figure 3.25 Chip Gain versus Pumping Current for TE and TM Input Light Polarization

This polarization insensitivity is comparable to that measured in amplifiers with no mode transformer indicating that our laterally tapered section provides polarization insensitive mode transformation [19].

We have also explored the polarization behavior in the saturation regime, which is an important characteristic for optical switching systems. The basic gain region design achieves polarization insensitivity by carefully matching the TM gain provided by the tensile strained wells to the TE gain provided by both well types [20]. Maintaining polarization insensitivity over the range of input powers then requires the gain from each of the quantum wells to saturate in the same manner.

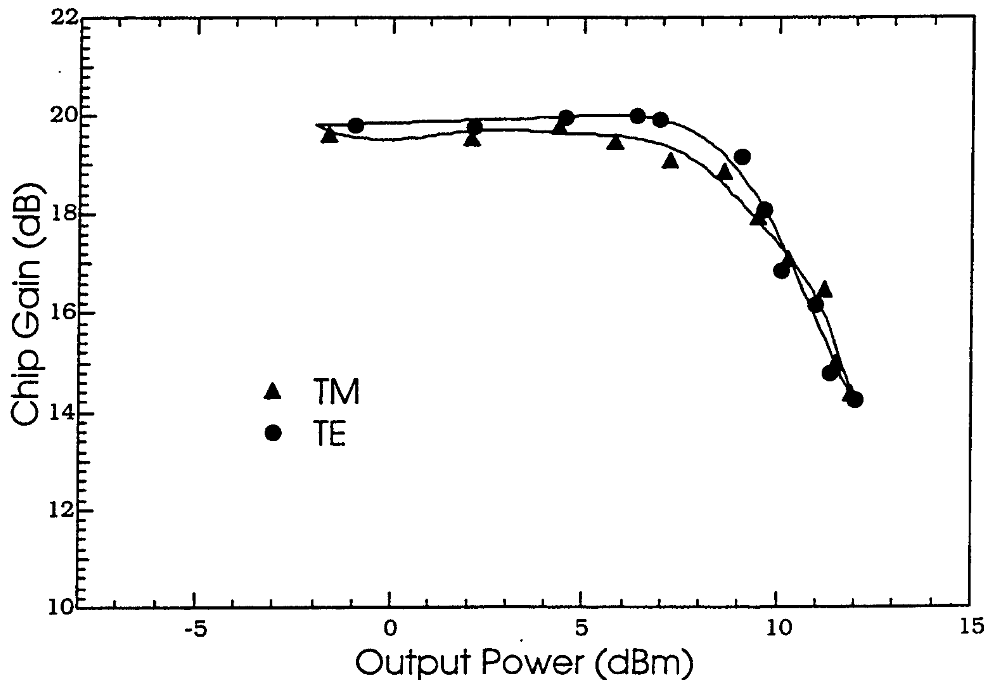

Figure 3.26 TE and TM Gain versus Output Power .The 3dB Saturation Power is Measured to be ~10 dBm Independent of Polarization

Previous work on similar structures has shown that polarization independence is achieved even into saturation in this design owing to the rapid equilibration of carriers and the optical cross coupling that occurs in this amplifier design [20]. The gain

saturation measurement results are presented on Figure 4. This data corresponds to 200 mA pumping current. Output power for -3dB gain saturation at 200 mA was found to be 10 mW and 10.2 mW for TE and TM modes, respectively. These values are comparable to those measured for un-tapered devices showing that the mode transformer does not degrade high power performance. This is expected because our laterally tapered section expands the waveguide mode and significantly reduces the confinement factor. Thus these sections provide less gain to the structure and do not effect the saturation characteristics. The spectral dependence of the gain for both TE and TM polarizations is measured indirectly from polarization resolved spontaneous emission spectra and directly by using a tunable laser and demonstrated comparable results as shown in Figure 3.27.

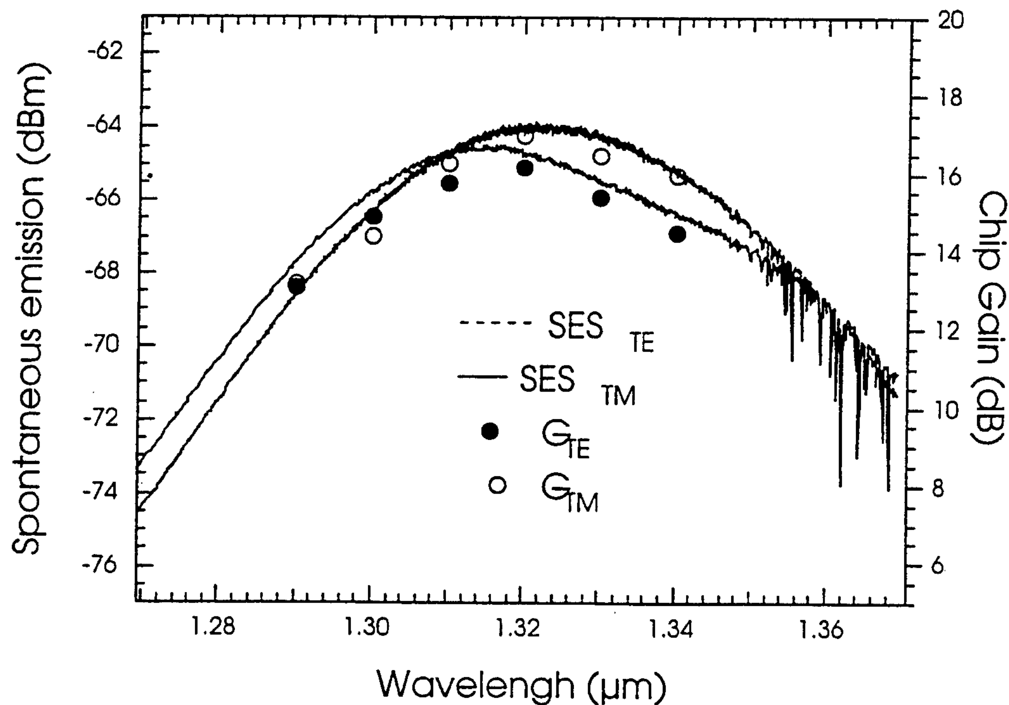

Figure 3.27 Chip Gain and Intensity of Spontaneous Emission versus Wavelength for Mixed Strain Amplifier with Integrated Mode Coupler

The gain bandwidth is measured to be 45 nm at the -3dB level. There is a maximum difference between TE and TM gains of ~1 dB over this entire range of wavelengths. This large polarization insensitive bandwidth will enable the use of wavelength division multiplexing in optical switching systems.

3.7 Conclusions

We have demonstrated for the first time a polarization insensitive, mixed strain quantum well amplifier with monolithically integrated mode transformers and have shown experimentally that the integrated, laterally tapered section does not affect polarization, saturation or spectral characteristics of the amplifier. We have demonstrated high gain (18 dB) and high saturation power (10 dBm) in a device with improved coupling to single mode fibers.

References

1 K. Uppal, D. Tishinin, I. Kim and P. D. Dapkus:" Study of 1.3μm tapered waveguide spot size transformers" JQE, Vol. 3 pp.975-980, 1997

2 K. Uppal, D. Tishinin and P. D. Dapkus: "1.3μm polarization insensitive tapered waveguide mode conversion structures with mixed quantum well active regions" LEOS 1996, oral presentation

3 H.Okamoto, Y.Suzaki, Y.Tohmori, M.Okamoto, Y.Kondo, Y.Kadota, M.Yamammoto, K.Kishi, Y.Sakai, M.Wada, M.Nakao and Y.Itaya, Electron. Lett. 32, (1996) 1099

4 H.Kobayashi, M.Ekawa, N.Okazaki, O.Aoki, S.Ogita and H.Soda, IEEE Photon. Tech. Lett. 6, (1994) 1080

5 A.Kasukawa, N.Iwai, N.Yamanaka, Y.Nakahira and N.Yokouchi, Electron. Lett. 32, (1996) 1294

6 R.Zengerle, B.Jacobs, W. Weiershausen, K.Faltin and A.Kunz, J.Lightwave Tech., 14, (1996) 448

7 B.Mersali, H.J.Bruckner, M.Feuillade, S.Sainson, A.Ougazzaden and A.Carenco, J.Lightwave Tech., 14, (1996) 1865

8 P.Doussiere, P.Garabedian, C.Graver, D.Bonnevie, T.Fillion, E.Derouin, M.Monnot, J.G.Provost, D.Leclerc and M.Klenk, IEEE Photon. Tech. Lett. 6, (1994) 170

9 D. Tishinin, K. Uppal, I. Kim and P. D. Dapkus, "1.3μm Polarization Insensitive Amplifiers with Integrated Mode Transformers" LEOS 98, oral presentation MP1

10 H.C.Casey, M.B.Panish and J.L.Merz, J.Appl. Phys., 44, (1973) 5470

11 A. Mathur and P. D. Dapkus : "Polarization insensitive strain quantum well medium for laser and optical amplifiers" Appl. Phys. Letters 61(24), 2845- 2847 (1992)

12 K Uppal, D. Tishinin and P. D. Dapkus: " Characterization of mixed quantum well structures" J. Apply. Physics 81(1) pp. 390-393 1997

13 R. Zengerle and W. Weiershausen: " Tapered two-layer InGaAs/InP waveguides for highly efficient chip coupling to single mode fibers" Optics Communications 115, 453-460 (1995)

14 Kelly, Lealman , Rivers, Perry and Silver : "Polarization insensitive, 25 db gain SOA withot antireflection coating. " Electronic Letters, Vol. 32, pp. 1835-1837, 1996

15 Gallant, Tilton, Bossert and Dente :"optimized single-layer antireflection coating for semiconductor laser" IEEE PTL, vol 9, pp.300-3002, 1997

16 Ramadas, Garmire, Ghatak, shenoy " Analysis of absorbing and leaking waveguides: a novel method", Optic Letters, vol 14, pp. 376-378, 1989

17 Fan, Riantm Verdiell and Dagenias: " Real-time insuty monitoring of Ar coating for SOA by ellipsomtry", IEEE PTL, vol.4, no9, September 1992

18 D. Zhu "Novel optical switches based on TW SAO" dissertation, 1997

19 . S. Dubovitsky, A. Mathur, W. Steier and P. D. Dapkus: "Gain Saturation Property of a Polarization Insensitive Semiconductor Amplifier Implemented with Tensile and Compressive Strain Quantum Wells." IEEE Phot. Tech. Letters 6, 176-178 (1994)

20 . A. Mathur and P. D. Dapkus : "Polarization insensitive strain quantum well medium for laser and optical amplifiers" Appl. Phys. Letters 61(24), 2845- 2847 (1992)

Chapter 4

Vertical Resonant Couplers with Precise Coupling Efficiency Control Fabricated by Wafer Bonding

4.1 Introduction

Dense WDM components and fiber amplifiers have dramatically increased the bandwidth of long distance telecommunication systems in recent years. The next step in utilizing existing fiber bandwidth is reducing channel separation. Add/Drop nodes based on high Q cavity devices have to be implemented to individually access any single channel in future networks. Semiconductor μ-cavities are attractive elements to incorporate into WDM photonic integrated circuits [1,2] as wavelength selective elements because of their extremely high Q-factor (narrower channel separation become possible), low losses and small sizes.

In contrast to existing waveguide technology, which may occupy several millimeters of material in photonic integrated circuits, μ-resonators can be implemented in elements as small as a few μm in dimension [3,4]. Optical waves propagating in a whispering gallery mode in such a μ-resonator may be coupled in and out of the cavity by precisely positioned waveguides with very small mode overlap. Coupling strength, which is defined by separation, should be small enough to avoid overloading the Q-factor of the cavity, but should be strong enough to support mode energy transfer. The separation

should be controlled precisely in this system to achieve "critical coupling" (rate of energy transfer due to coupling to the resonator is equal to the sum of all losses). In this condition all energy will flow from the input waveguide to the output waveguide. In all we have WDM channels propagating in one waveguide, that we can selectively extract at any single wavelength.

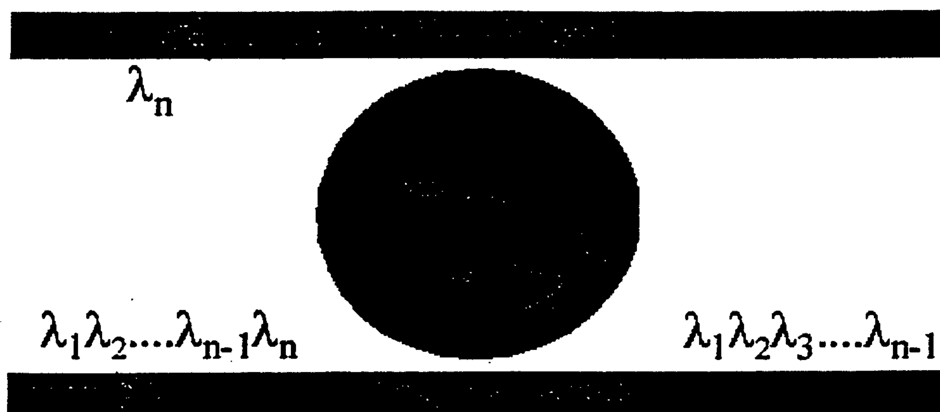

Figure 4.1 Schematic Diagram for Add/Drop Note with Single μ-Disc Coupled to 2 Waveguides

To understand how this is achieved, we can consider a μ-disc evanescently coupled to two waveguides: the input and the output. The coupling has to be small to retain narrow cavity modes. We assume that we have a set of wavelengths propagating in the one of the waveguides, such that only few correspond to resonant frequencies in the resonator. These wavelengths will be coupled to a cavity mode and energy will be transferred into the resonance cavity and sequentially to the second output waveguide. Signals with other frequencies will propagate through the input waveguide.

The small size of these elements, the potential for large-scale integration, and the possibility of achieving very narrow linewidths in high Q resonators are some of the key advantages of these elements. To achieve narrow linewidths in high Q resonators suitable

for WDM applications, weak and precisely controlled input and output coupling is required. We proposed to use novel vertical coupling region, which allows us to precisely control resonator coupling and make many new kinds of μ-resonant devices.

4.2 Device with Vertical Coupling Region

A free spectral range of 10-50 nm requires a resonator cavity, either a ring or a disk, with a diameter in the range 5-20 μm and a lateral index step large enough to support strongly guided ring or whispering gallery modes [4]. In earlier work [1,2] these constraints were met by using evanescent side coupling between waveguides and 10- 20 μm diameter resonators formed with air/semiconductor interfaces.

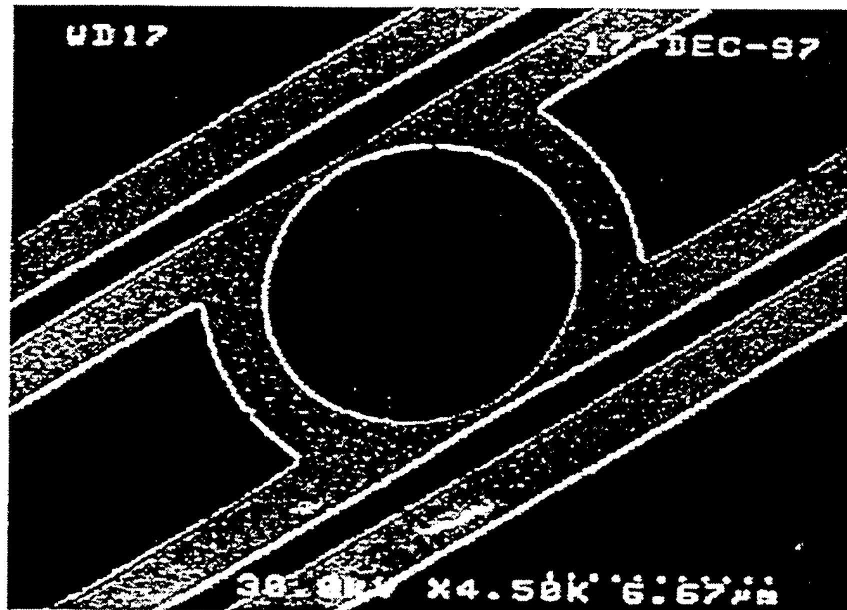

Figure 4.2: μ-Disc Laterally Coupled to Waveguides

The waveguides and μ-disc were created using electron beam lithography. SiN was used as a mask for ECR etching of the semiconductor materials. For single mode operation, such side coupled structures require waveguides with widths less than 1 μm and coupling separations smaller than 0.1μm. Owing to the evanescent nature of the coupling, the

coupling is exponentially dependent upon the separation between the waveguide and the cavity. It is difficult to control the dimensions and loss of the waveguide and the coupling between structures when such a fine control is required, even with e-beam lithography. Furthermore, the use of side coupling also requires the use of the same waveguide structure in both the disk and the waveguides. This eliminates the option of employing active and passive components in the same circuit.

The approach presented in this chapter [5] exploits the ability to produce precisely controlled coupling separations through epitaxial growth rather than lithography by using vertical coupling rather than lateral coupling structures [1,2]. In this approach, resonators and waveguides are vertically stacked during epitaxial growth with independent control and optimization of the structure and technology used for each. Our implementation of this approach enables a generic methodology for complex three-dimensional integration of waveguide structures.

Our approach is shown schematically in Figure 4.3.

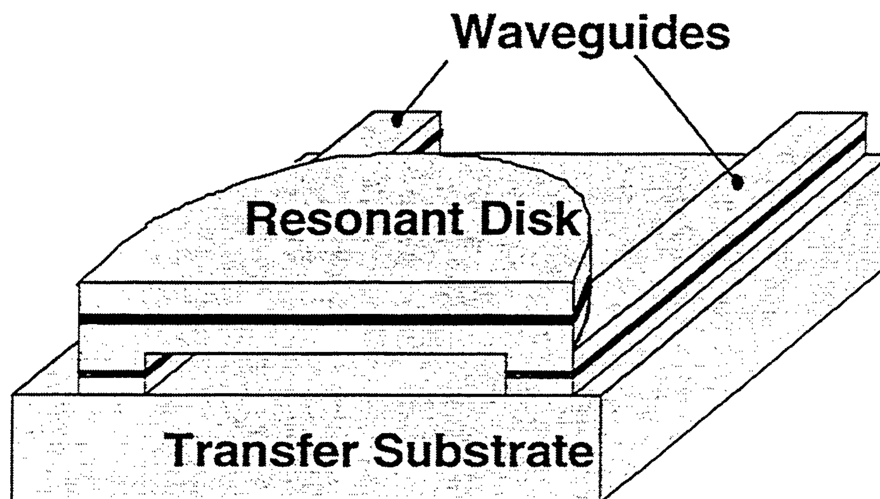

Figure 4.3 Design of the Vertical Coupler

Coupling between input/output waveguides and the microresontator occurs vertically through a precisely controlled waveguide separation layer that is epitaxially grown. The entire vertical, double waveguide structure, including the guiding layers for the μ-resonators, is formed in a single planar epitaxial growth. The layer thicknesses are chosen to provide the desired vertical confinement and coupling in the waveguides and resonator. Thus, layer thicknesses and all critical separations are defined by the epitaxial growth and this coupling gap can be easily controlled in the submicron range to achieve precise control over coupling. The waveguide structures were optimized independently with waveguide layers 0.5 μm thick and disk layers 0.3 μm thick. These parameters were used to achieve low propagation losses in the waveguides and good mode matching to the disk.

The coupling between the waveguides and the resonator was estimated using the mode overlap between a straight waveguide and a parabolically curved guide as was described previously [5]. The coupling in the vertically coupled structures used in this paper was estimated to be less than 1%. Wafer bonding was used to process multilayer structures. The next Figure shows SEM photographs of vertically coupled waveguide resonator structures that have been fabricated using this approach.

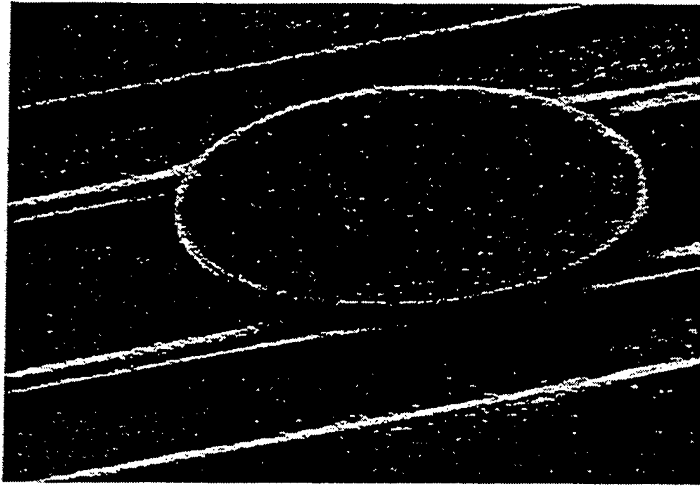

Figure 4.4 Picture of Final Structure; μ-Disk is Suspended on Input/Output Waveguides with an Air Gap Below

The resonators and waveguides employ air-semiconductor lateral guiding and exhibit smooth sidewalls that are consistent with the formation of low loss devices. From the next SEM picture we can clearly see that the suspended 40 μm disk exhibits no bending and is robust enough to withstand all the post processing.

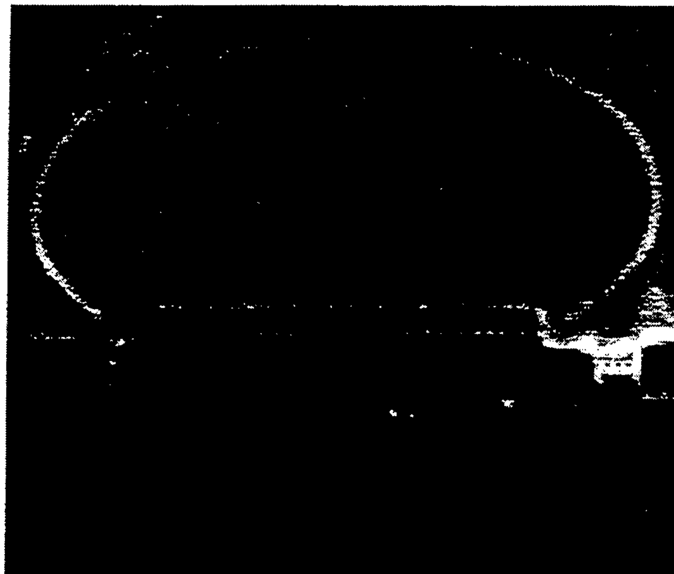

Figure 4.5 Cross Section for 40μm Suspended μ-Disk

4.3 Waveguide Approximation

To estimate the resonator performance first we need to understand the loss mechanism for the loaded cavity. It is desirable for DWDM systems to have a resonator with a high Q-factor. By definition, Q-factor is inversely proportional to the cavity losses, as we can see from the following expression:

$$Q = \frac{E_{store}}{dE/_{dt}\,T}, \text{ where}$$

E_{store} - Energy stored in the cavity

$dE/_{dt}$ - Loss of energy per unit time

T -Period of oscillation

We can add up all of the losses to find total energy dissipation per cycle. As a result, total cavity Q can be calculated as:

$$\frac{1}{Q} = \frac{1}{Q_{scatering}} + \frac{1}{Q_{absorbtion}} + \frac{1}{Q_{coupling}} + \ldots$$

The different Q's represent different channels for energy flow. We can see from here that to create a high Q cavity we need not only make a cavity with high quality surface and low absorption, but also have fine, controllable coupling. For example one percent energy loss per period limits the Q-factor for the loaded cavity to a value less that 100.

Overlap between the waveguide mode and cavity mode can be used to estimate the total coupling [6]. First, we compute the waveguide mode and then we estimate overlap. We have to remember that we are dealing with coupling between strait and circular waveguides and thus have a short interaction length as a result. This means that

4.3 Waveguide Approximation

To estimate the resonator performance first we need to understand the loss mechanism for the loaded cavity. It is desirable for DWDM systems to have a resonator with a high Q-factor. By definition, Q-factor is inversely proportional to the cavity losses, as we can see from the following expression:

$Q = \frac{E_{store}}{\frac{dE}{dt} T}$, where

E_{store} - Energy stored in the cavity

dE/dt - Loss of energy per unit time

T -Period of oscillation

We can add up all of the losses to find total energy dissipation per cycle. As a result, total cavity Q can be calculated as:

$$\frac{1}{Q} = \frac{1}{Q_{scatering}} + \frac{1}{Q_{absorbtion}} + \frac{1}{Q_{coupling}} + \ldots$$

The different Q's represent different channels for energy flow. We can see from here that to create a high Q cavity we need not only make a cavity with high quality surface and low absorption, but also have fine, controllable coupling. For example one percent energy loss per period limits the Q-factor for the loaded cavity to a value less that 100.

Overlap between the waveguide mode and cavity mode can be used to estimate the total coupling [6]. First, we compute the waveguide mode and then we estimate overlap. We have to remember that we are dealing with coupling between strait and circular waveguides and thus have a short interaction length as a result. This means that

phase matching is not important and that the coupling coefficient does not depend on wavelength. The cross-sectional geometry for our system is presented in the next figure.

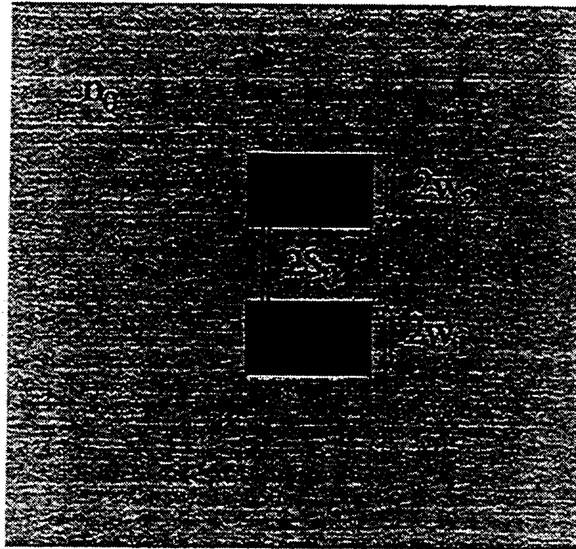

Figure 4.6 Geometry and Index Profiles of 2 Coupled Waveguides

Here $2S_0$ is the smallest separation between waveguides, and n_i is the index for each layer. The entire structure is embedded in material with index n_o. Both waveguides in the general case are assumed to be curved with radius R_1 an R_2. A straight waveguide can be viewed as a waveguide with R->∞. In this case instantaneous coupling strength can be evaluated as [6]:

$$\kappa[s(z)] = \frac{\varepsilon_0 \omega}{4} \int_{-\infty}^{\infty} (n_1^2 - n_0^2) e_1(x) e_2^*(x) dx$$

Where:

$e_j(x)$ is normalized energy in a waveguide,

ε_0 - is the permittivity of free space and

w is the circular frequency of the propagating light.

To calculate net coupling we need to integrate instantaneous coupling strength over the interaction region, weighted by the mismatch in phases between propagating modes:

$$\kappa_{total} = \int_{-\infty}^{\infty} \kappa[s(z)] e^{-j\Delta\beta z} dz$$

Where the phase mismatch $\Delta\beta = \beta_1 - \beta_2$. We can see that coupling, $\kappa[s(z)]$, depends exponentially on the separation, hence only the region with smallest separation needs to be considered in our calculations. To make this system integrable, we should treat circular curvature as parabolic with transformation:

$s = s_0 + \gamma z^2$ with $\gamma = \dfrac{1}{2R}$, where $R = \dfrac{R_1 R_2}{R_1 + R_2}$ is a normalized radius.

We can find our net coupling with this approximation and we can integrate over the interaction length:

$$\kappa = \frac{\omega\varepsilon_0 \cos(k_x 2\omega_2)}{2\sqrt{P_1 P_2}(k_{x1}^2 + \alpha_2^2)}(n_1^2 - n_0^2) \times \sqrt{\frac{\pi R}{\alpha_2}} \exp[\alpha_2\omega_2 - 2s_0] \times$$
$$\times [\alpha_2 \cos(k_{x1}\omega_1)\sinh(\alpha_2\omega_1) + k_{x1}\sin(k_{x1}\omega_1)\cosh(\alpha_2\omega_1)]$$

Where:

$P_i = \dfrac{\beta_i}{2\omega\,\mu_0}(\omega_i + \dfrac{1}{\alpha_i})$ is the normalized mode power,

$\alpha_i = \sqrt{\beta_i^2 - n_0^2\kappa^2}$ is the cladding decay constant where

$k_{xi} = \sqrt{n_i^2 k^2 - \beta_i^2}$ is the propagation constant.

In all cases i is referring to the waveguide and k is the free space wave vector.

We calculated coupling [7] for different μ-disc diameters and indices of cladding. The most interesting cases are when: 1) the waveguides are embedded in the semiconductor material. 2) the region between waveguides is filled with air. The first case can be implemented with buried waveguides, or by filling the separation between waveguides (where an interaction occurs) with high index material. The semiconductor-air-semiconductor is a typical example for laterally coupled waveguides, separated by an air gap. We have done coupling calculations for different disc diameters in the case of a semiconductor filled environment. Diameters studied were chosen from 10-40μm.

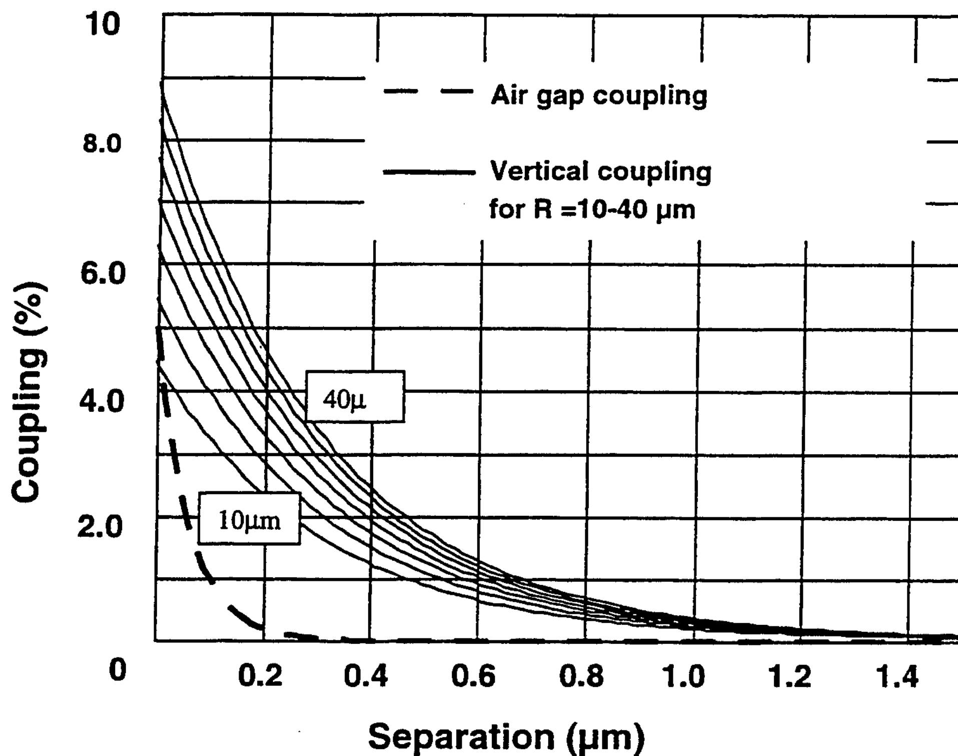

Figure 4.7 Coupling Estimation for 10-40 μm Ring (Solid Lines) with Semiconductor Spacer Layer and with Air (Broken Line) Spacer for 40 μm Ring.

We can see from the figure above that we have stronger coupling to high diameter discs. This happens because we did not take into account phase shift caused by waveguide

curvature. All phase mismatches in our calculations are due to difference in waveguide geometry. The interaction length is increasing almost linearly with disk diameter and if there are no additional phase differences accumulated, the coupling will also increase. In the case where coupling length is small compared to critical distance there will be no other phase differences. As a result we can say that our coupling does not depend on the frequency of the propagating light.

It is also important to notice a difference in the distance providing the same coupling strength between the air and a semiconductor filled interface. We can find from the graph that to achieve 1 percent coupling we need an air gap of less than 0.1μm, while we can have a 0.5-0.7 μm separation layer in a semiconductor filled case. This by itself increases tolerances in separation by almost 10 times.

The quality factor for a cavity can now be calculated from the definition as a ratio between stored energy to energy coupled per optical cycle.

$$Q \approx \frac{2\pi^2 R n_1}{\lambda_0 K^2}$$

Where K is a coupling coefficient, R is the disc radius, and λ_0 is the wavelength in vacuum.

We only consider two loss mechanisms in this case: coupling and radiation losses. Therefore Q-factor depends only on the coupling coefficient and disc radius. Results for a 20μm radius cavity are presented in the next figure.

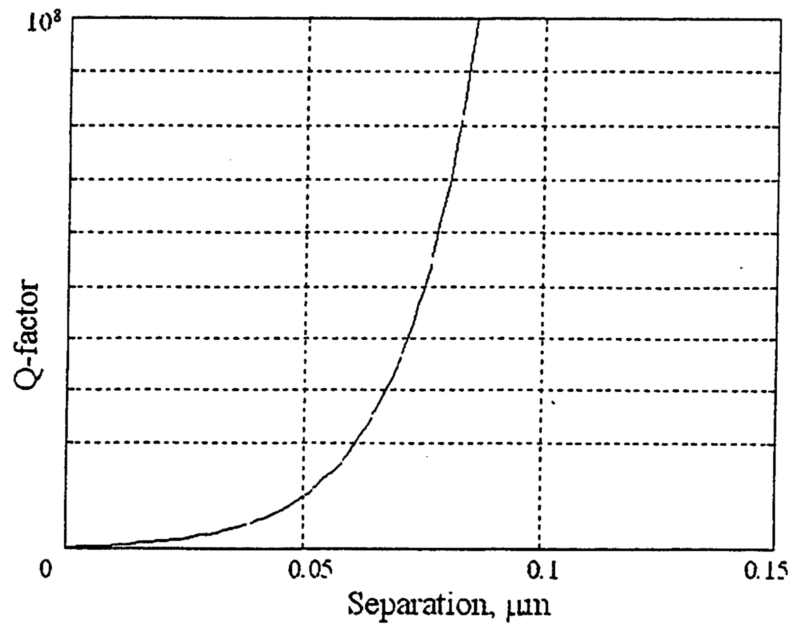

Figure 4.8 Q-factor for Loaded Cavity vs. Separation fro a semiconductor separation layer

We can see from this graph that quality factor increases exponentially with decreasing coupling strength. A very high quality factor cavity can be designed in this way. Unfortunately, the Q-factor for an actual device reduces due to many other kinds of losses.

Bandwidth can be defined at the half-power level and it can be calculated if we know the quality factor for a cavity. We can estimated it like λ/Q

$$\Delta\lambda \approx \frac{2K^2\lambda^2}{(2\pi)^2 Rn_1}$$, where we used $\Delta\omega = \frac{2\pi c}{\lambda_0^2}\Delta\lambda$.

The bandwidth is proportional to K^2, which shows the amount of power coupled into the ring.

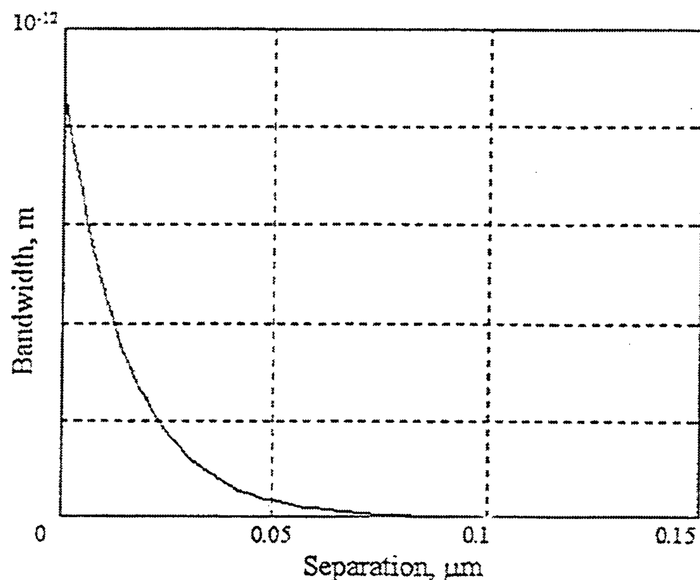

Figure 4.9 Bandwidth as a Function of Separation for 20µm Ring

The bandwidth decreases as quality factor increases as we see from the graph above. This analytical evaluation lets us see the trends and estimate any possible changes. Since they do not take into account resonant effects, which are very important for microcavity devices, we have to use a numerical simulation to completely understand mode behavior in the cavity.

4.4 Numerical Analysis

Filter Finite Difference Time Domain (FFDTD) [8] calculations utilize direct solutions to Maxwell's equation do find the mode structure.

$$\nabla \times E = -\frac{\partial B}{\partial t} \qquad \nabla D = \rho$$

$$\nabla \times H = J + \frac{\partial D}{\partial t} \qquad \nabla B = 0$$

First, we generate a model for the device and guess the initial pulse for the electro-magnetic field. Final solutions can be obtained by propagating the guess field in time-space. We can filter out mode structure and energy distribution as result of this simulation.

The structure is presented as a matrix in this calculations. We have an option to use two-dimensional rectangular or cylindrical coordinates as a basis for the device. Cylindrical symmetry in devices such as VCSEL's or μ-discs/rings can be used to reduce dimension to two and still preserve full device properties. Full 3-dimensional calculations require a lot of computer memory and can take a very long time. Therefore, in the course of this research we mainly used 2 dimensional approximations. The first step in creating any of these models is allocating a matrix and filling it with a background material.

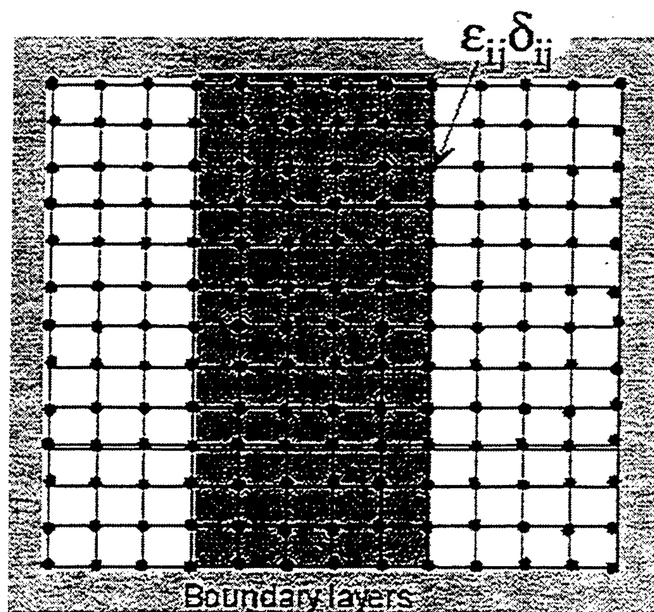

Figure 4.10 Structure Prepared for Simulation with Imbedded Waveguide and Boundary Layers

We assign a dielectric constant and conductivity to each point in the matrix. Waveguides, resonators and all other elements are created by modifying material parameters in specific regions of the system. For example, in figure 4.10, I show a waveguide, which represents a device in the center of cladding material. Supportive layers have to be placed near the external edge of the structure to preserve electromagnetic field continuity, which is a problem because of the finite size of the modeling area. We can create any complicated structure in this manner by superposition of many different areas.

The initial guess field has to be created also. It will propagate in space and time to filter out resonant modes. We can calculate the coupling of energy from the initial guess field to the resonance mode as $\int \boldsymbol{E}_{guess} \boldsymbol{E}^{*}_{r\,\mathrm{mod}\,e} \boldsymbol{d}^{3}\boldsymbol{r}$. A δ-function was used as an initial guess. It provides similar coupling to all possible modes in the disc structure due to rotational symmetry.

We can simulate it by creating an extremely sharp, Gaussian distribution. A software package Visualization Tool Kit (VTK) was used to superimpose the field on the structure and check initial settings.

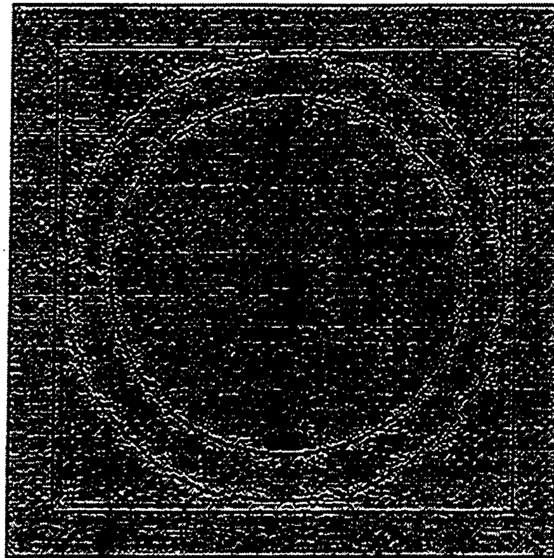

Figure 4.11 Electro–Magnetic Field Plotted on the Top of μ-Ring Waveguide with Absorbing/AR Coating Surrounding Regions

We can see that our initial guess field has a δ-function shape and is located in the center of ring waveguide. It will couple in all modes, which have nonzero overlap.

First, we propagate the EMF in time and monitor power at some points. It is very reasonable to choose a starting point for monitoring. In this case we should have an initial bump (at T=0 all other energy is concentrated there).

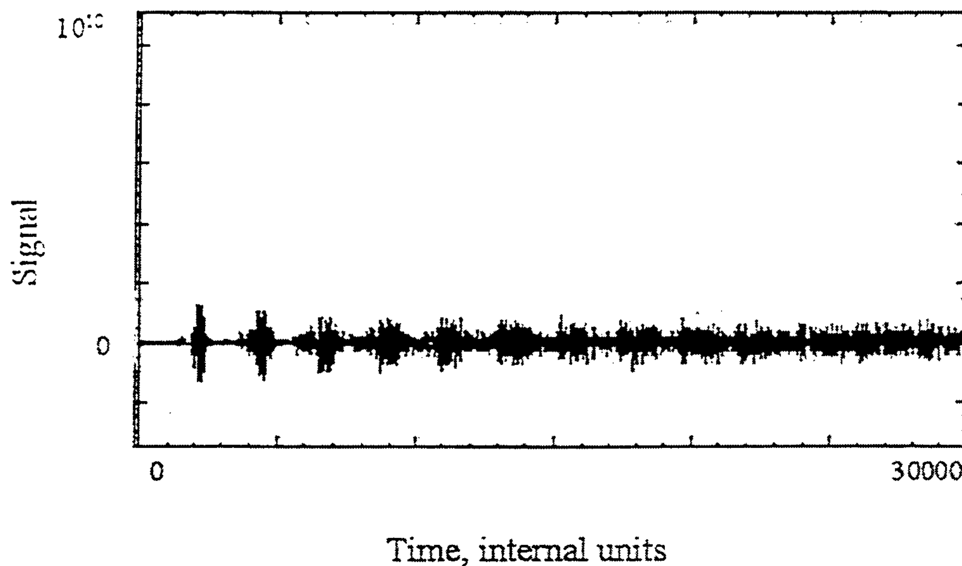

Figure 4.12 Signal vs. Time for the μ-Ring Resonator

We can also see periodicity in the signal due to round trip time delay. A Fourier transform must to be performed in order to extract the resonant frequency for the studied system.

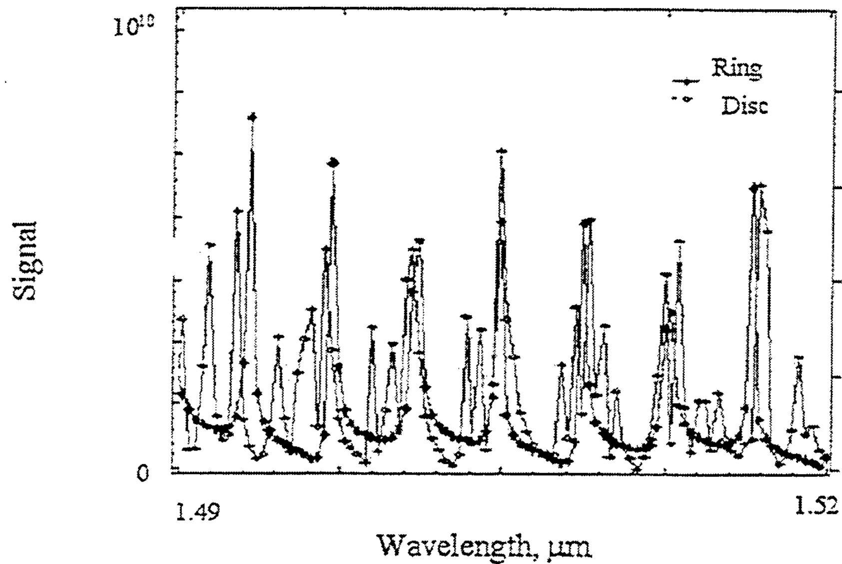

Figure 4.13 Resonance Frequencies vs. μ-Ring/μ-Disc with the same Diameter

We can see, after a Fourier transform, where the resonant frequencies are located for a given system design. Discs have high mode density compared to a μ-rings. We believe that we see higher order radial modes [1], which are supported by discs but cannot propagate in a μ-ring. Numerical values used for resonant frequencies are calculated for internal units, where we assume c=1(speed of light) and distances between points in the device matrix are also equal to one. This makes the structure scalable with respect to the wavelength. One can find out precise device dimensions if the resonance is to be matched to some set of transmission frequencies.

Resonance frequencies determined through Fourier transforms are used to filter out energy distribution in a guided mode. The next figure shows two different modes corresponding to ω_{res1}=0.1304687813 and to ω_{res2}= 0.1279301318. They correspond to two next nearest peaks on the frequencies graph, but the separation is great enough to filter out the two different modes.

We also can determine the error in the Q factor for each mode. They are

	Mode # 43	Mode # 44
Resonance Frequency	0.1279301318	0.1304687813
Quality Factor	12430.7255	13120.189
Calculation Error in Q-factor	0.0019417856	0.00088261271

We can see that both modes have high Q- factor and our calculation error is very small. The mode with the higher quality factor was calculated with lower calculation error, because the energy in the resonator has a lower leakage rate. Thus the signal-to-noise ratio is higher because the mode propagates for a longer time. The energy distribution for each mode is presented in the next figure. Both modes look very similar, but there is a difference in the number of maxima and minima on the plot.

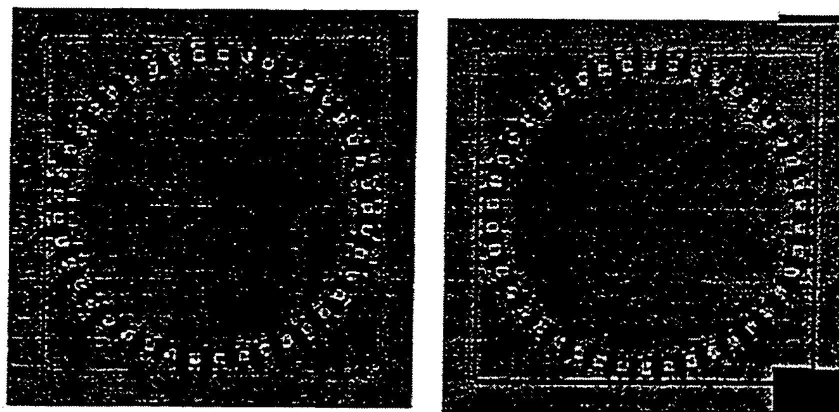

Figure 4.14 Energy Distribution in a μ-Ring for 2 Adjacent Modes

We can add a set of waveguides coupled to the μ-disc. The initial guess EMF can be launched on to one waveguide. Energy will flow out from the waveguide through its ends, but some portion will be coupled to the μ-disc.

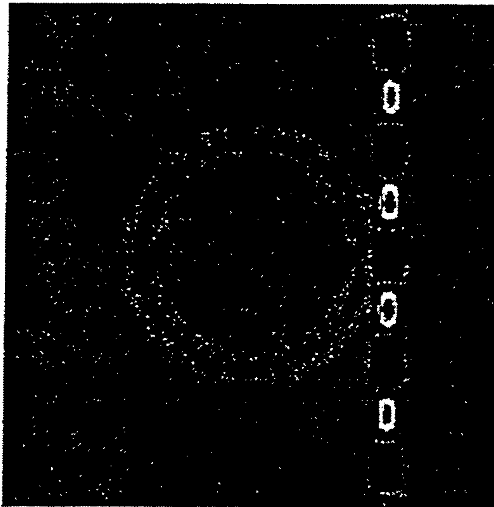

Figure 4.15 Initial Guess Field for μ-Ring Coupled to Input/Output WGs

Energy, coupled to the μ-cavity will leak out over time, but due to the high quality factor of the disc, it's decay rate will be smaller. Over time, the energy distribution shifts form the waveguide (at $T = 0$) to the resonant cavity as we can see in the next figure.

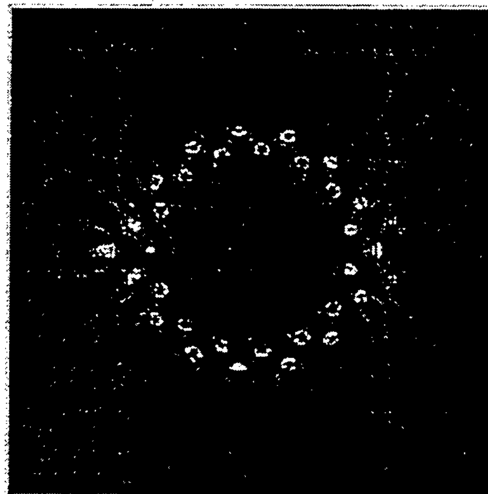

Figure 4.16 Resonance Mode Filtered for a μ-disc Coupled to Input/Output Waveguides

Only the cavity mode survives after propagating for a period of time. The energy propagates in the resonator with some leaking out through the waveguides. The Q-factor for this system is reduced compared to an isolated disc. The calculations show Q_{loaded}=1278.107. This is a more than 10 times reduction compared to an unloaded resonator, due to additional losses from waveguide coupling. The coupling coefficient was estimated to be less than 0.1%.

Three-dimensional calculations can be done in the same way. The difference is the dimensionality of the matrices used in the system. We have generated initial three-dimensional matrices for structures and initial fields.

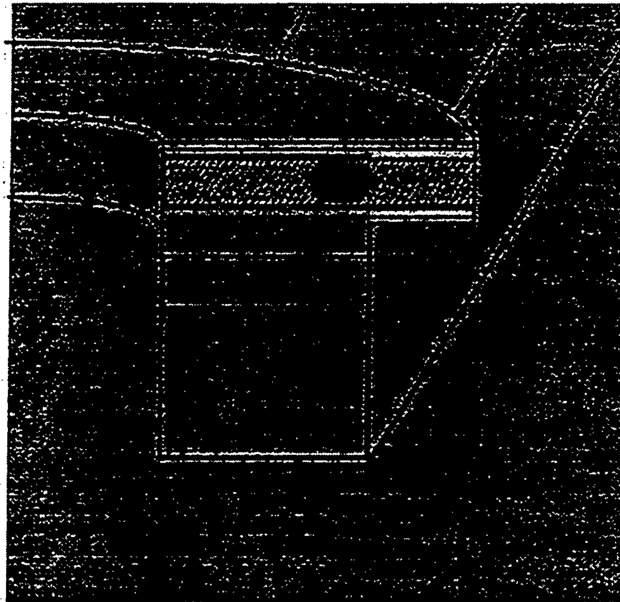

Figure 4.17 Initial field for 3D Vertical Coupler. Gray Line Represents AlOx Regions, Used to Confine Cavity Mode

Fig. 4.17 presents a cross-section of a µ-ring located on top of a waveguide. The initial EMF was launched in the cavity to improve energy coupling.

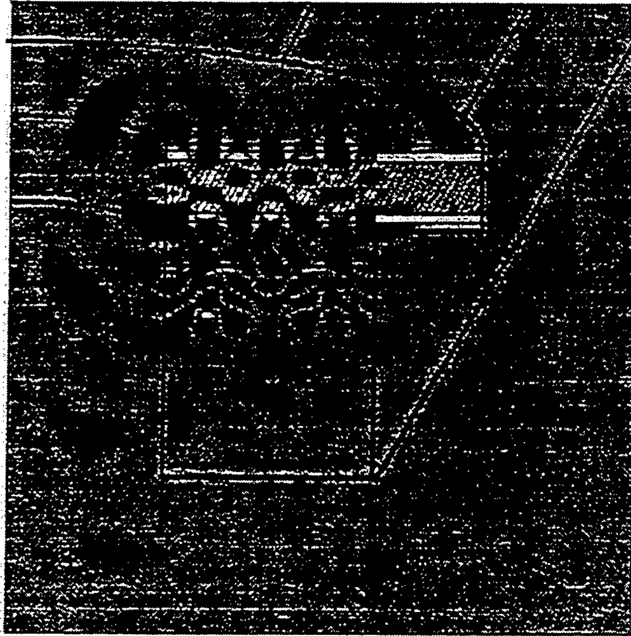

Figure 4.18 Resonance Mode for vertically coupled structure

The energy distribution follows the same principles as in the 2D calculations. Resonant modes are supported by the μ-ring and energy leaks in to the waveguide through the coupling layer, located in between.

4.5 Device Testing Results

To determine the spectral transmission of the coupler, a fiber coupled tunable laser (New Focus Model 6328) with central wavelength around 1550 nm was coupled into one of the waveguides and the output of the same guide was monitored with a photodetector. Polarization of the input light was controlled using a polarization-maintaining fiber only on the input side. The output light from the waveguide was collected using bulk optics with an iris diaphragm used to select the guided mode as it is schematically shown in the Figure 4.19.

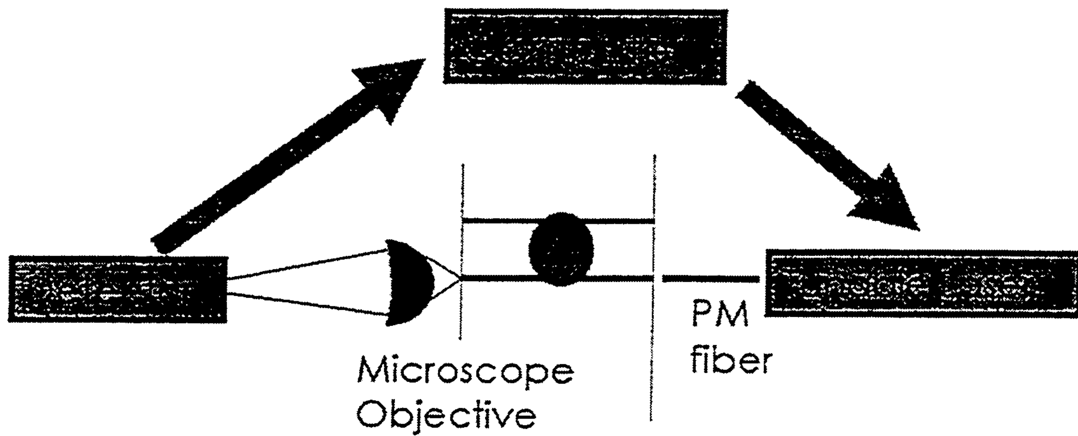

Figure 4.19 Testing Setup Used for Wavelength Selective Measurements

Both the incident and transmitted light intensities were measured to normalize any intensity fluctuations from the source and intensity fluctuations on the output at various wavelengths. No antireflection coating was deposited on the input/output ends of the waveguides. Results for a resonant coupler employing a 44μm diameter (40μm after 2μm lateral oxidation from the edge of the disc) disk in the AlGaAs GaAs system are shown in Figure 4.20.

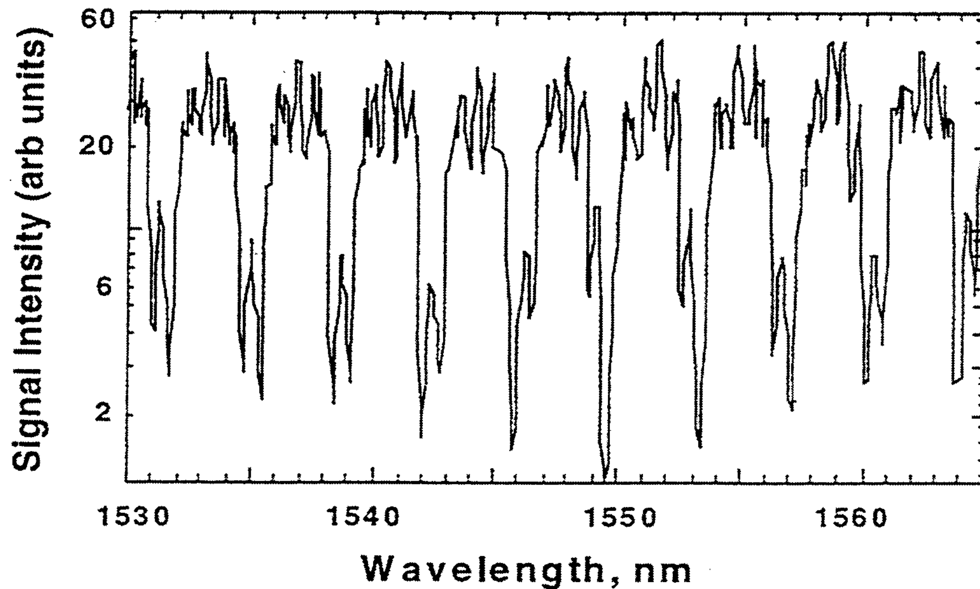

Figure 4.20 Transmission Spectra for 40 μm. μ-Disk

These data were obtained from a structure in which the radial mode confinement in the disk was achieved by the use of selective oxidation of an AlAs layer located above and under disc waveguide layer [9]. As mentioned earlier, the data in Figure 3.20 is affected by the Fabry-Perot modes of the input waveguide. It is evident from the shallow, high frequency oscillations in the data. More important for the purpose of this chapter are the presence of deep minima in the spectrum that results from resonant coupling from the waveguide to the μ-disk on top. The free spectral range of these resonances corresponds roughly to the estimates for a disk of this dimension and generally scales with the dimension of the disk. Light resonantly coupled to the output Fabry-Perot waveguide structure showed only the complementary spectral components. Without removing the Fabry-Perot resonances from the data it is not possible to accurately measure the Q of the resonator. However, our best estimate, using the width of the minima ($\lambda/\Delta\lambda$), of the Q for these structures was approximated at 700, which correspond less than a 1% coupling efficiency. At present we do know if the Q estimated in this way is being affected by our failure to resolve individual disk modes, which can be densely spaced, particularly when the coupling occurs to the more complex radial modes of the disk structure. In our geometry, where the waveguide is under the disk, increased coupling to higher order modes is possible and some additional care must be taken to assure that only lower order disk modes are excited. For example, the waveguide can be spaced further towards the edge of the disk or the disk geometry can be modified to frustrate the higher order radial modes.

Light coupled to the μ-disc eventually should be coupled to the other output waveguide. We can use this [10] to create add/drop nodes for a WDM system. It should

be pointed out that the disc mode is not a standing wave as in Fabry-Perot cavity mode. In the case of standing wave devices, energy traveling in one direction is equal to the energy traveling in the opposite direction. Waves coupled to a μ-disc from input waveguide couple to modes that are propagating only in one direction. Of course some light gets scattered and eventually maybe coupled to counter the propagating mode, but the majority of the light should stay in the mode. Output light for the same reason should propagate in the opposite direction with respect to input light, so this resonator works like a μ-bend on 180^0. We should have been able to detect output light from the second waveguide in our device, but technically it was impossible. The distance between input-output waveguides was less than 40μm, which is less than a fiber cladding diameter, so we cannot directly detect light coming from the output waveguide in our present test setup configuration. As mentioned before, we did not have an AR coating on the facets, so in reality light coming from a μ-disc was reflected by semiconductor/air interfaces at the end of the waveguide. Thus we can detect it from the other end.

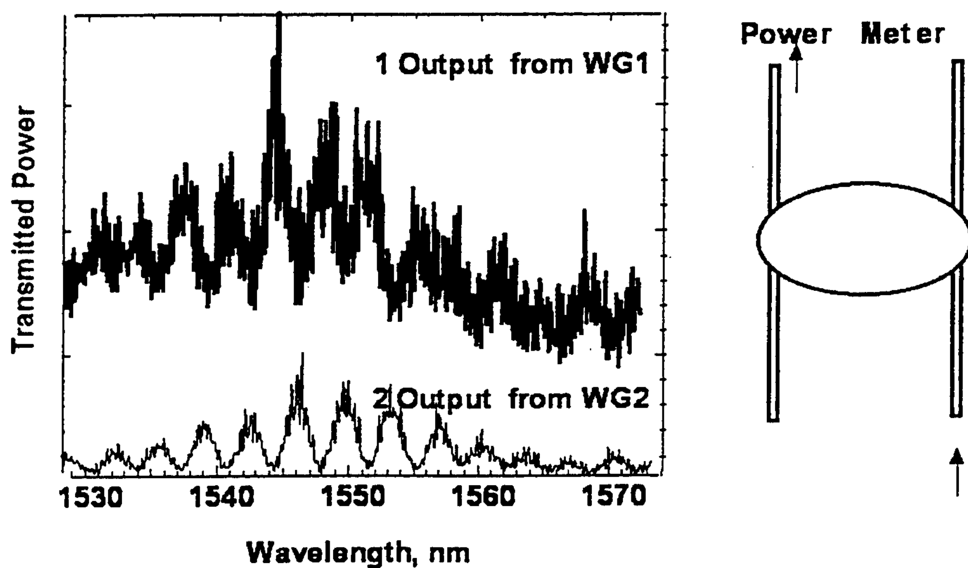

Figure 4.21 Output Light for 2 Waveguides

We can see that transmission spectra for the first waveguide and coupled spectra for the second are complementary to each other. Energy coupled to the μ-disc from the first waveguide is eventually coupled out from the resonator to the second output waveguide. Separate layers were used for disc and waveguide processing, so this lets us easily modify the structure and incorporate a gain into the resonator layer. We choose an InP based material system to achieve gain at 1.5μm. Four quantum wells were located in the disc waveguiding layers. We shifted a maximum PL intensity to low wavelength so it was not completely aligned with the tunable laser emission range. The reason for doing this was to observe μ-disc properties in the region where gain is changing.

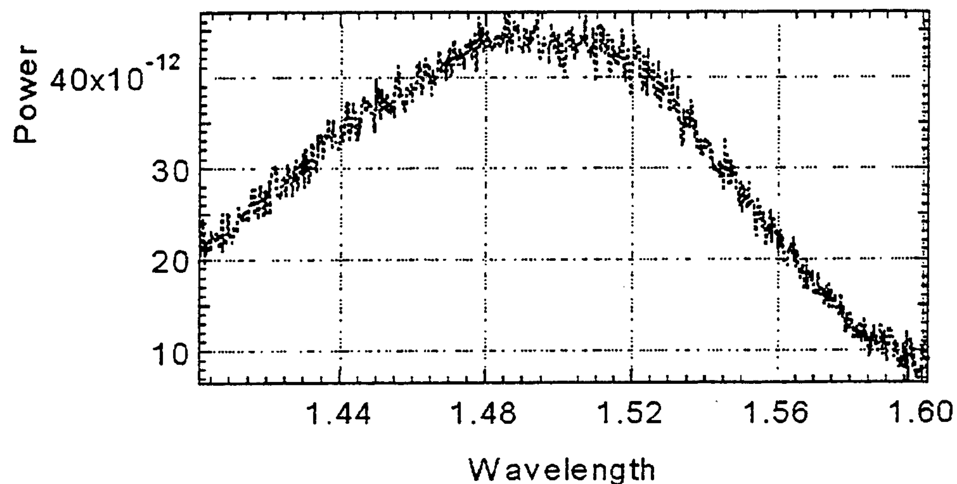

Figure 4.22 PL data for Active μ-Disc Device

This sample was processed the usual way with additional steps to create electric contacts as it shown in the next figure.

Figure 4.23 Gold Contact on the Top of the µ-Ring

This contact was used to pump a µ-disc and create a gain. This gain can compensate for radiation losses of the device and improve the quality factor. The slow variation of the intensity corresponds to QW gain variation.

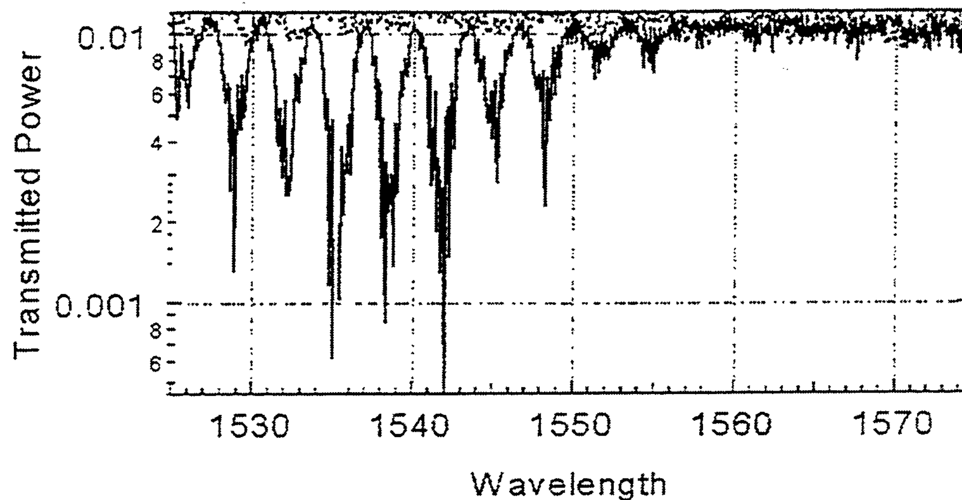

Figure 4.24 Transmission Data for an Active µ-Disc Device

We can see that the µ-disc does not show any resonance transmission pattern without pumping (blue curve). High disc losses do not allow modes to build up and transfer energy to the other waveguide. Device gain lets us overcome losses and the quality factor is improved, so clear transmission minima appear on the graph. We can see

it only on the low part of the scanned wavelength, because our gain was initially offset to lower the high-energy side.

Further optimization of this coupling structure is underway to implement higher Q and single mode structures, to eliminate the Fabry-Perot modes and to study the dependence of coupling (and Q) on the separation distance.

4.6 Conclusion

We have demonstrated a novel approach to the formation of resonant couplers that employs vertical coupling controlled by epitaxial layer thickness between waveguides and resonant structures. We have chosen to demonstrate the concept using μ-disks owing to their potential for compact dense WDM PIC implementation but any other resonant structure is possible. Clear evidence for resonant coupling was demonstrated. A unique aspect of the processing approach used here is the definition of complex waveguide structures on two sides of an epitaxial structure by using wafer bonding to a transfer substrate to obtain access to the second side of the layer structure. This approach is generally useful for fabricating complex three-dimensional PICs.

References

1. D. Rafizadeh, J.P.Zhang, S.C. Hagness, A. Taflone, K.A.Stair, and S.T.Ho: "Waveguide Coupled AlGaAs/GaAs Microcavity Ring an Disk Resonators with High Finesse and 21.6-nm Free spectral Range" Optical Letters vol. 22, No16, August 1997, pp.1244-1246

2. J. Foresi, B. Little, G, Steinmeyer, E. Thoen, S.Chu, H. Haus E. Ippen, L. Kimerling, and W. Greene: "Si/SiO_2 Micro-Ring Resonator Optical Add/Drop Filters"LEOS1996 CPD22-2

3. P. D. Dapkus, D. Tishinin, and In Kim "Active and Passive Microdiscs Coupled to Waveguides for WDM Applications" LEOS 99

4. B.E. Little, S.T. Chu, H.A.Haus, J. Forresi, and J.P.Laine: "Microring Resonator Channel Dropping Filters" Journal of Lightwave Technology, vol 15 no 6, June 1997, pp.998-1005

5. D. V. Tishinin, I. Kim, A. E. Bond, C.K. Lin, and P. D. Dapkus, "Novel fabrication process for vertical resonant coupler with precise coupling efficiency control," LEOS 11th Annual Meeting, (Institute of Electrical and Electronics Engineers, New York, 1998) Orlando, FL, December, 1998; paper TuK5.

6. B.E. Little, S.T. Chu, H.A.Haus, J. Forresi, and J.P.Laine: "Microring Resonator Channel Dropping Filters" Journal of Lightwave Technology, vol 15 no 6, June 1997, pp.998-1005

7. D. Tishinin, P. D. Dapkus, A. E. Bond, I. Kim, C. K. Lin and J. o'Brien "Vertical resonant couplers with precise coupling efficiency control fabricated by wafer bonding" PTL Vol.11. pp.1003-1006, 1999

8. Chu and Chaundhuri "A finite-difference time-domain method for design and analysis of guided-wave optical structures" J. Lighwave Tech. Vol. 7, pp. 2033-2038, 1989

9. E.I. Chen, N. Holonyak, J.M. Ries: "Planar Disorder-Defined and Native-Oxide-Defined Photopumped AlAs-AlGaAs Superlattice Minidisk Lasers" Journal of Applied Physics, vol 79, issue 11, June 1996, pp.8204-8209

10. Little, Haus, Foresi, Kamerling and Ippen:"Wavelength switching and routing using absorption and resonance" IEE PTL, vol. 10, No 6, July 1998

Chapter 5

μ-Disc Processing

5.1 Introduction

This chapter will discuss processing steps for μ-resonators discussed in Chapter 4. ~~We developed a new appro~~ach based on usage of wafer bonding. This technique lets us process structures with two waveguiding layers. Waveguides grown separately on top of each other can be defined independently in top and bottom layers. We apply this technique to obtain unique integrated structure of the μ-disc on top of the two waveguides. Geometrical differences between top and bottom layers do not allow any other ways to define the bottom waveguide, as is shown in the next figure. This unique vertical integration makes this processing extremely useful for creating principally new devices, like vertical coupling for μ-resonators (see Chapter 4)

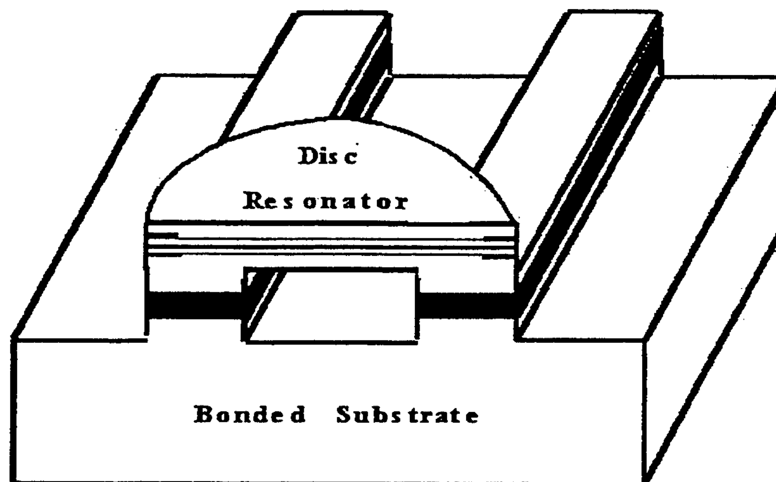

Figure 5.1 Schematic Drawing for Resonator Vertically Coupled to the Waveguides

5.2 Device Structure

In this work, we used both GaAs and InP materials systems. Devices based on the GaAs material system used in this study were grown in a home-made MOCVD system. Vertical reactor geometry provides very good sample uniformity and reproducibility of the growth [1, 2]. The sources used in this system were arsine, TMG and TMA. Hydrogen was used as a carrier gas for all the sources. Growth was done at 76 Torr and 7300C. All flow rates, temperature and reactor pressure were control by computer. The layer compositions in both cases were similar. Active InP devices will be discussed separately. We have employed an etch-stop layer and two waveguiding layers with layers of low index material in between. In our initial studies, we used a 0.2μm thick layer of InGaAs and Al95Ga05As as the etch-stop layer on InP and GaAs substrates, respectively. The waveguide structures were optimized independently with waveguide layers 0.5 μm thick and disk layers 0.3 μm thick being used to get low propagation losses [3] at the waveguides and good mode matching to the disk. In the GaAs samples, AlxO was used for lateral confinement of the light in the disk structure. A 0.2-1.0 μm thick low index layer was used for the separation layer in all the samples. The coupling between the waveguides and the resonator was estimated using the mode overlap.

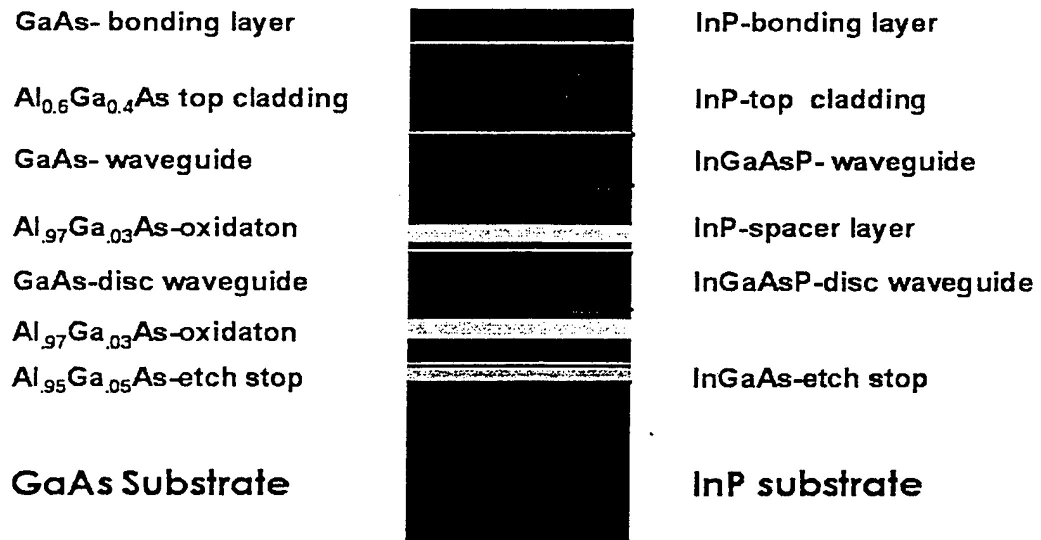

Figure 5.2 Device Structure Used for Vertical Coupler

This picture presents a typical structure layer design. The first grown layer ($Al_{.95}Ga_{.05}As$ -0.5μm.) was used as an etched stop layer. The other layers define a structure in reverse order from top to bottom. The waveguide to be used for disk definition is actually a lower layer. The top index layer will be used to define input/output waveguides, which will ultimately be on the bottom of the structure.

5.3 Processing Overview

To form different lateral waveguiding structures in the waveguides and the resonators, we employed a novel processing sequences [4] as shown in following figure.

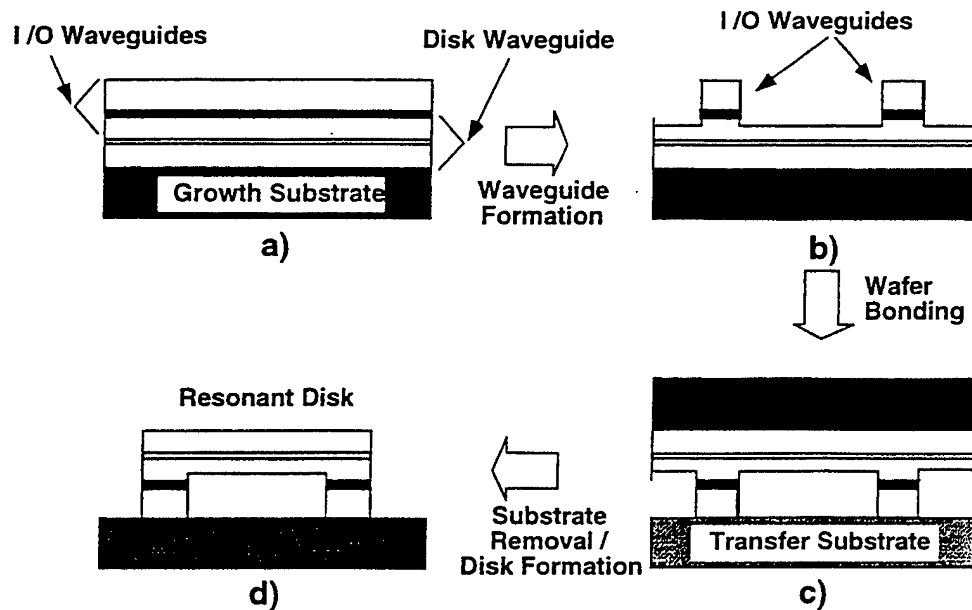

Figure 5.3 Vertical Coupler Processing Overview
a) As-grown structure with coupled waveguide layers
b) I / O waveguide formation
c) Wafer bonding to transfer substrate
d) Growth substrate removal and disk formation

The input and output waveguides in our coupler are grown as the top layers of the structure. Waveguides are first fabricated in the top layers using a simple etched mesa [5] waveguide structure. The lateral waveguide could be formed in a number of well-known ways including ridge stripes, buried heterostructures, or oxide confined stripes. After this step the top of the epitaxial layer is atomically wafer bonded to another (transfer) substrate and the original substrate is removed by polishing and selective etching [6]. It is noteworthy that the transfer substrate does not have to be of the same material as the original substrate and several possibilities can easily be envisioned (Si, silica, insulating oxides, other III-Vís). After removal of the original substrate, the bottom epitaxial layers are exposed for independent lateral patterning and waveguide

formation. The completed structure is then processed into devices using conventional processing techniques. The processing approach can be used to fabricate more complex PICs that involve coupling between multiple resonant structures and between waveguides in different layers of the structure. It resembles recently published [7,8] and independently developed three-dimensional waveguide couplers but differs in certain important aspects. Most important is the use of a contiguous epitaxial layer in the present work to minimize the difficulty of aligning the top and bottom layers.

5.4 Waveguide Etching

The input and output waveguides are fabricated on top of the epitaxially grown layer using conventional optical lithography and electron cyclotron resonance (ECR) reactive ion etching. Air-confined waveguides were used to simplify processing. The multimode waveguides were 2-μm wide. Later we started to use ridge waveguides to be able to produce single mode devices. It is almost impossible to make a single mode waveguide with optical lithography on air-confined structures. The huge index step at the semiconductor/air interface supports several modes even for submicron waveguide widths.

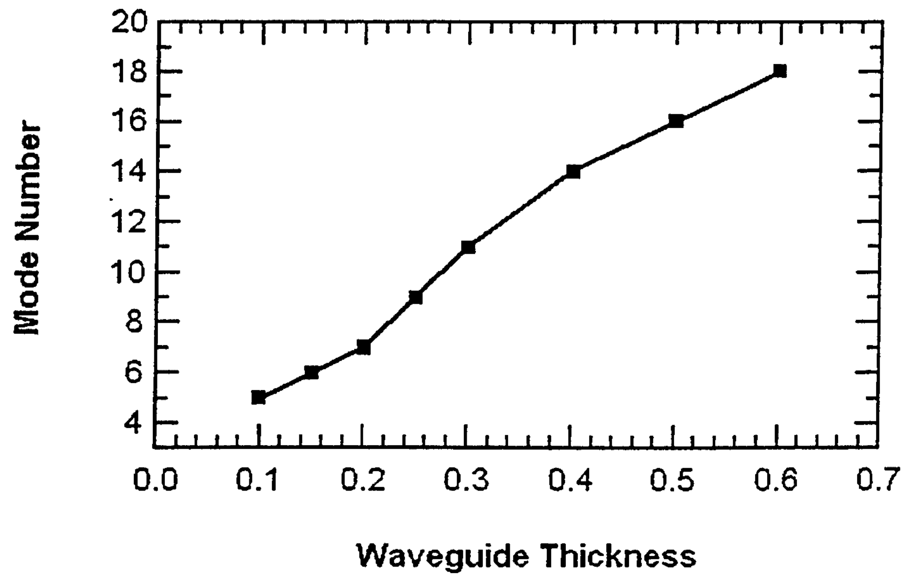

Figure 5.4 Mode Number vs. Waveguide Thickness

Another problem with the air-confined waveguide is low effective index, so we have to increase the thickness of the guiding layer to reduce coupling into the substrate mode. Calculated effective index as a function of waveguide parameters is presented in the figure below.

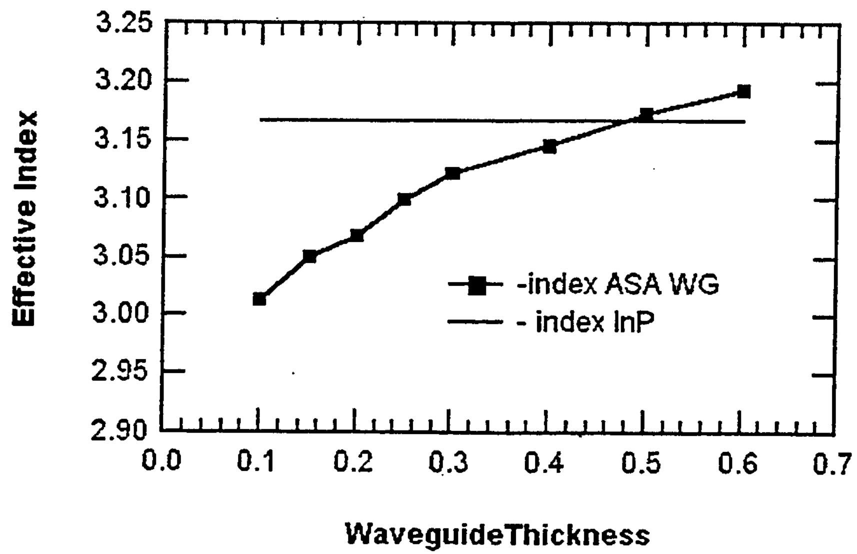

Figure 5.5 Effective Index for an Air Confined Waveguide vs. Thickness

Ridge waveguide structure can be easily designed to support only one mode.

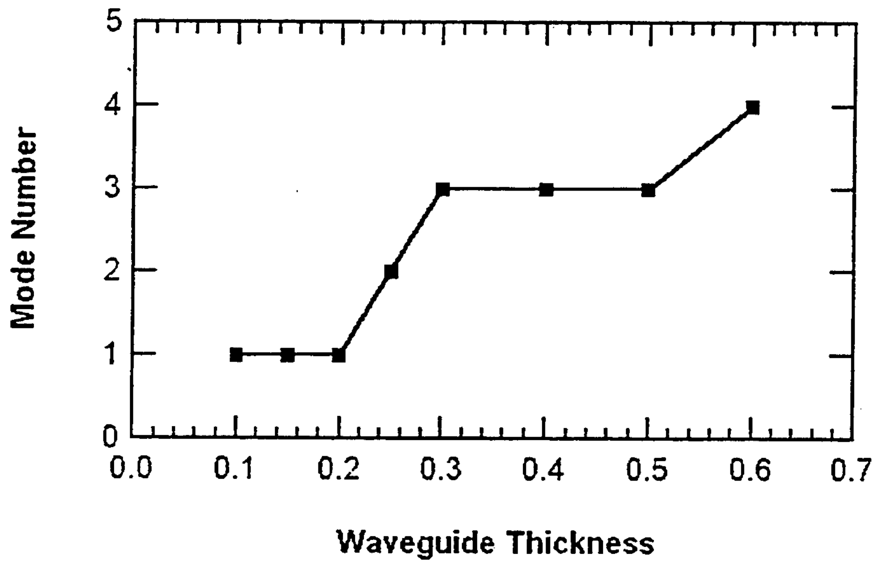

Figure 5.6 Mode Number for RWG

We can see that a waveguide of thickness less than .2 μm exhibits clear single mode properties, while the same waveguide with air on both sides supports at least six modes. The effective index for the ridge waveguide also does not change with thickness as fast as that for air-confined structure. We can see this in Figure 5.7

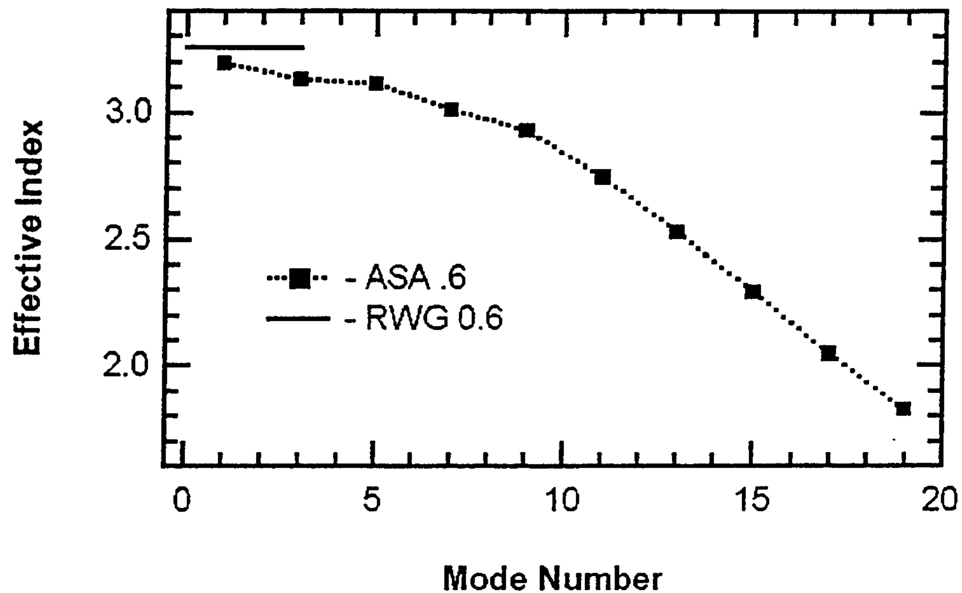

Figure 5.7 Effective Index as a Function of Waveguide Thickness for RWG and ASA structures.

The structures were etched through the top cladding layer and waveguiding layer and terminated within the separation layer for air-semiconductor-air waveguides. Etching was terminated in the top cladding in the RWG structures. Samples were cleaned with O_2 plasma after an ECR etching [9]. An SEM picture of the prepared sample is presented in the next Figure.

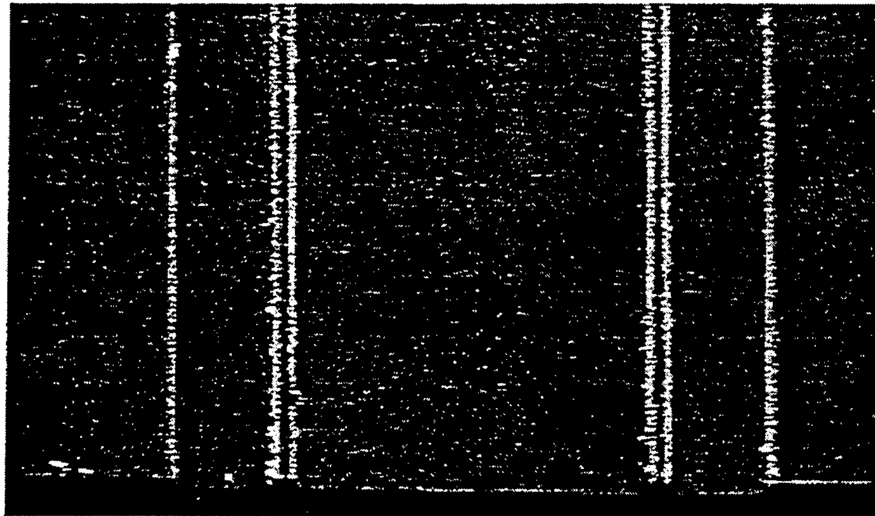

Figure 5.8 Cross-Section of an Etched Sample

This processed surface is then bonded to another wafer (InP or GaAs in our examples) and the original substrate is removed by polishing and selective etching.

5.5 Wafer Bonding

In this set of experiments the transfer substrate was the same as the original substrate, i.e. GaAs samples were bonded to GaAs and InP samples to InP substrates. As was previously mentioned, there is no strict physical limitation on the transfer substrate, because the bonded interface is not a part of the device. All active layers are located well above the bonded interface and are optically isolated from it. The thickness of the isolation layer is not a constriction on our devices due to the fact that it is not a part of coupling region. The bonding temperature was optimized in each case to avoid sample degradation.

5.5.1 Temperature Calibration

We will discuss temperature optimization for InP based materials, however, structures based on GaAs material system were optimized exactly the same way [6]. To optimize bonding temperature we made a sample with a quantum well located near the surface. We tried two different InP spacer layers near the surface: 0.1 and 0.7 μm. Channels were etched in the top layer, which defined a separation. These test samples were bonded at different temperatures to bare substrates and photoluminescence was measured from the quantum wells.

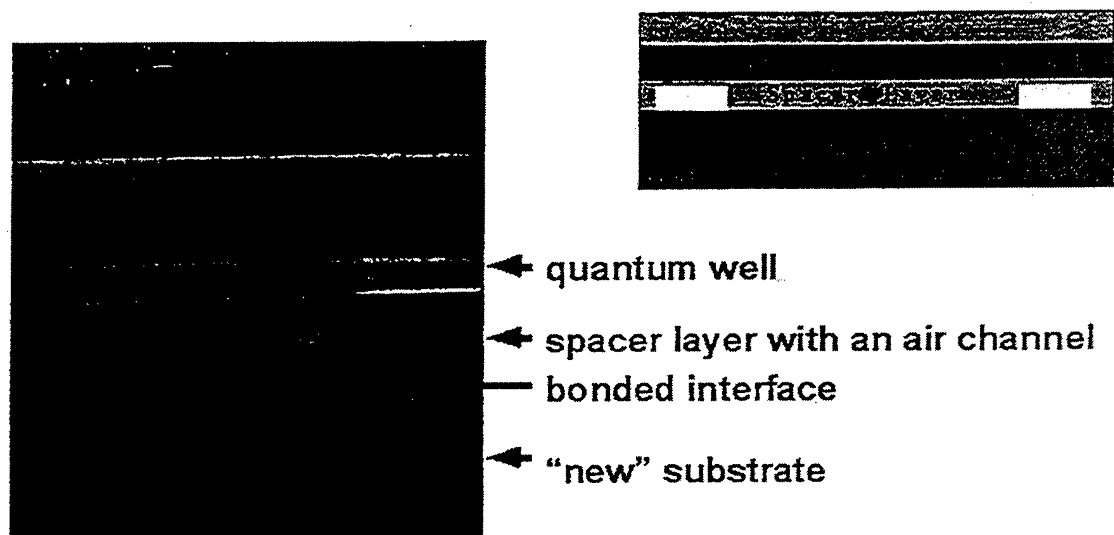

Figure 5.9 Testing Sample Layer Structure and SEM Photograph or Bonded Interface

We can see from SEM pictures that the bonded interface is almost undetectable and quantum wells located near the bonded surface do not display any visible degradation. PL results are presented in the next Figure.

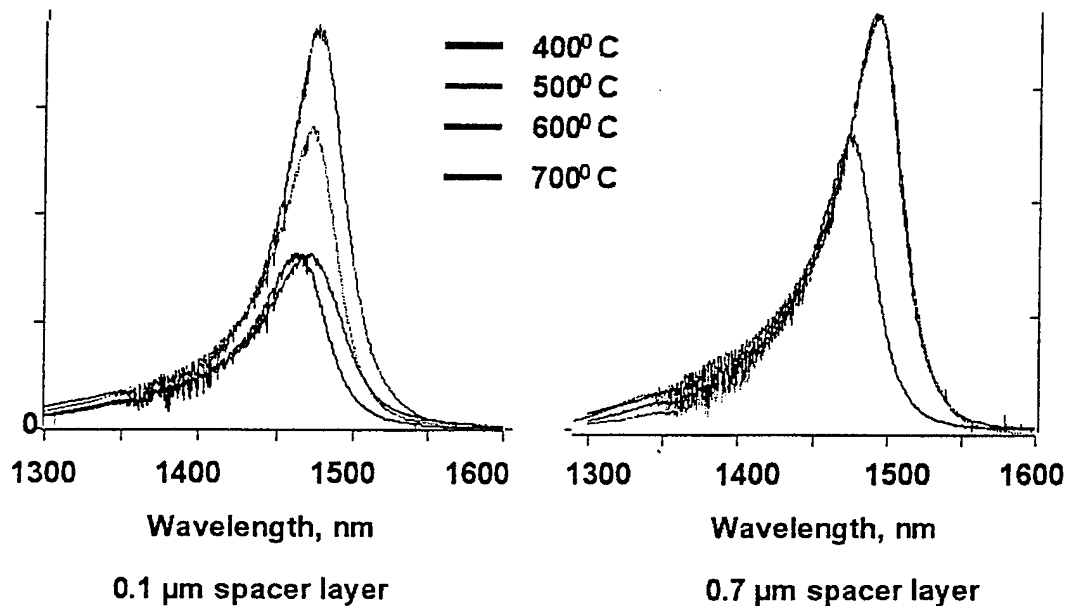

Figure 5.15 PL data for InP Bonded Samples

Samples with 0.1μm separation layer show no degradation in luminescence if bonding was done at 400^0C. Higher bonding temperature decrease PL intensity compared to the "as grown" sample. We were able to increase the range of temperatures suitable for bonding by increasing the spacer layer thickness to 0.7μm. Samples with thick separation between the quantum wells and bonded interface show no degradation in Pl intensities up to 600^0C. Bonding done at 700^0C still degrades the quantum wells. We need to check the electric properties of the interface to finally define the bonded temperature, because we already know that mechanical stability is good.

We use broad area devices, fabricated on bonded surfaces, to check the electrical properties. Lasers were located on the bonded area and were processed under standard conditions, as it was described in Chapter 2. We used 4 compressive quantum wells located 0.7mm above the bonded interface. All other layer thicknesses were the same as

in conventional lasers. We did, however, add one etched stop layer underneath the whole structure. This etched stop layer was removed before testing.

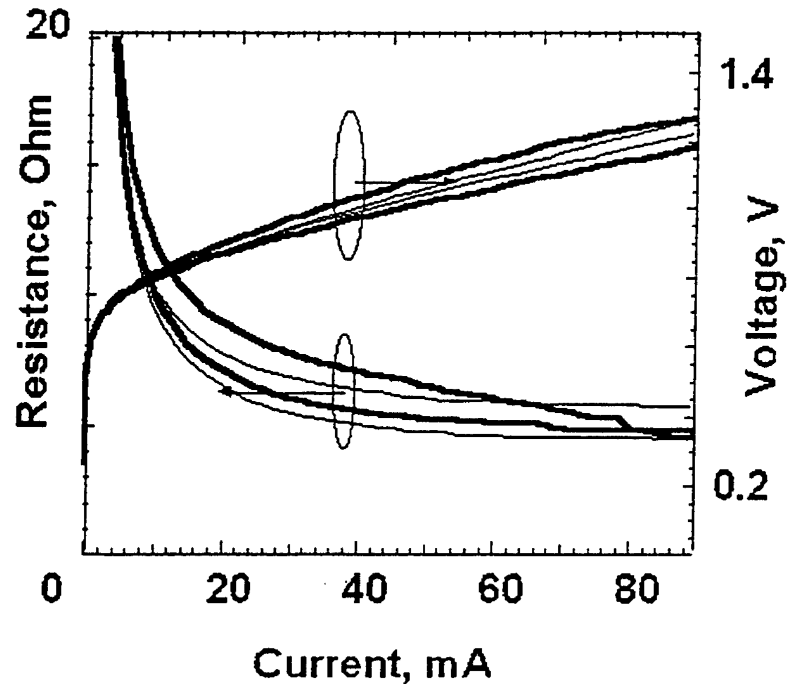

Figure 5.10 Current-Voltage Characteristic and Resistance Data for Bonded Samples

Sample were 60 µm wide and 700µm long. Resistance to forward bias was less than 5 Ohms, which is comparable to typical laser structures of the same size [11], therefore the bonded interface does not increase device resistance. Voltage across the junction measured for bonded devices is the same that we would expect to see on broad area lasers. This shows that our bonded interface exhibits ohmic behavior.

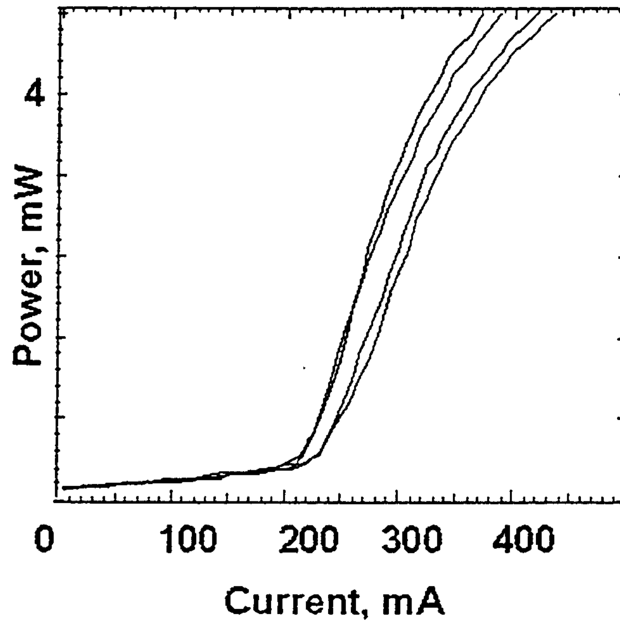

Figure 5.11 LI Data for InP Broad Area Lasers

Lasers processed from bonded material show uniform characteristic with threshold around 200mA (for devices 60x700mm), which corresponds to a 350-400A/cm^2 current density. We have a threshold current density of less than 100A/cm^2 per quantum well, which is comparable with the best laser results [12].

All this data shows that InP bonding done at 400^{0}C does not degrade quantum well quality and provides good mechanical stability and a low resistance, ohmic interface suitable for active device processing. Similar calibration was done on GaAs samples, so we chose to use 400^{0}C bonding temperature for InP wafers and 750^{0}C for GaAs based materials.

5.5.2 Bonding Procedure

Samples were etched in an ECR system to form waveguides before bonding. The channels between waveguides were used to extract gases trapped between wafers [6]. We used an oxygen plasma asher to make sure that the sample surface did not contain organic residue. Typical time used for this procedure is 2 minutes (similar to regrowth preparation). Then the sample was thoroughly cleaned with organic solvents. The sample surface was then etched with Buffered Oxide Etchant for one minute. We put both sample and bonded substrate in water and put them in contact with a water tank. All this processing was done in a clean room environment. Samples were taken from the clean room after they were placed in contact and pressure was applied by our bonding fixture. The bonding fixture used in this set of experiments contains three graphite plates connected with molybdenum screws. The bottom plate has three threaded holes for initial screw fixations. The middle plate was not fixed on the rods, so it was able to rotate on some angle, which allows more uniform pressure to be applied to the sample surface. The top plate was applying pressure through graphite balls located in between the top and middle plate. A schematic drawing for the bonding fixture is presented in the next Figure.

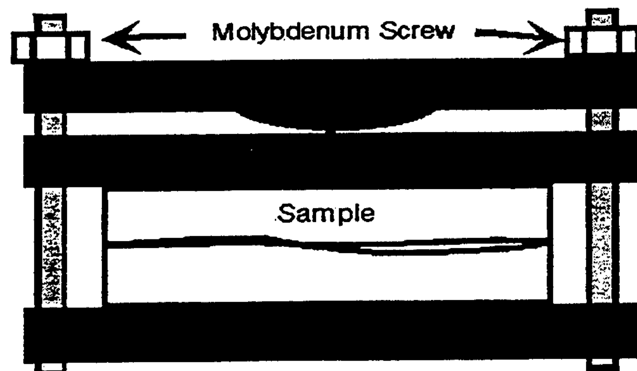

Figure 5.12 Bonding Fixture Used for Samples Bonding

After bonding, samples were lapped to 100-150 μm. and the original substrate was removed by selective wet etching. We used $HCl:H_2O$ (3:1) to selectively etch the InP substrate and NH_4OH: H_2O_2 (50:1). Selectivity to the stop layer was very good in both cases. We used InGaAs and $Al_{95}Ga_0As$ as a stop layer for InP and GaAs based material accordingly. The next picture presents a top view of the bonded sample

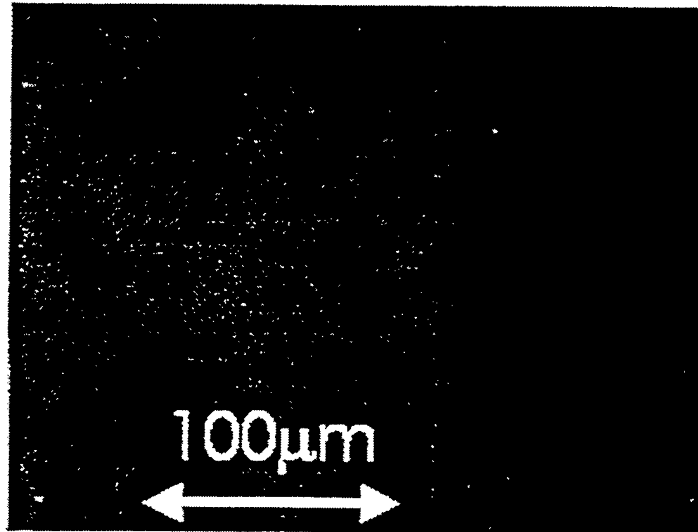

Figure 5.19 Top View of the Bonded Sample without Voids

Samples were ready for further processing after etching. After bonding we processed the other waveguide independently. The top surface was very clean and suitable for photolithography, while the bonded interface was very reliable and stable. We used the bonded sample to do all laser-processing steps, including heating (for SiN_x deposition and oxidation) and cleaving.

5.6 μ-Disc Definition

The thin layer of material on top of the already processed waveguide is completely transparent to IR light and backside alignment lets us position the μ-disk on top of the waveguides. μ-Discs were aligned on the top of the waveguide so that the coupling from both waveguides was similar. This was one the most important steps in equalizing input-output coupling. To get maximum energy transfer, input coupled energy should be equal to the sum of the losses due to scattering and output coupling. A good μ-disc resonator should have very low losses, thus we can assume that the input coupling is be equal to the output coupling. This means that the μ-disk has to be positioned almost symmetrically over the waveguides. Any displacement will increase coupling to one side and decrease cavity quality factor as a result. We were able to see both waveguides and our alignment was done using an optical microscope.

μ-Discs were etched using the ECR with chlorine-based etchants. Selective oxidation [13] was used to improve edge quality and to reduce scattering losses. Conditions were very similar to those used for waveguide definition [9]. We used a laser to control etching depth, and etching was stopped at the separation layer. Passive devices were thinned down to 100 -120μm. and cleaved on 500-1000μm bars

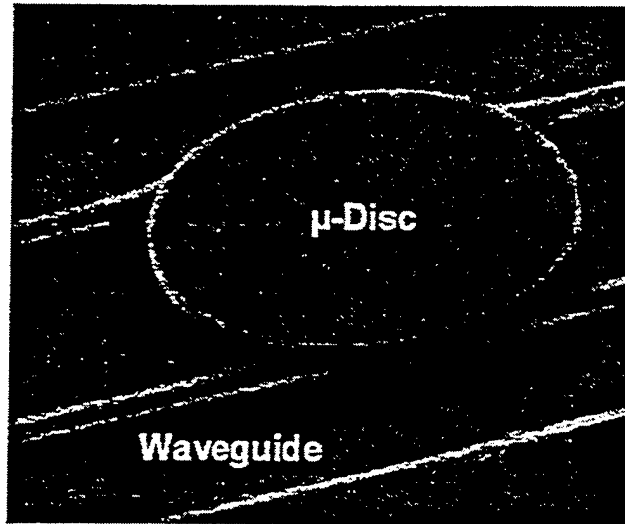

Figure 5.13 Top View for a µ-Disc Etched on the Top of Waveguides

The next SEM image shows that even a large diameter disk made this way is not wobbled, does not possess any waviness and is a very stable object.

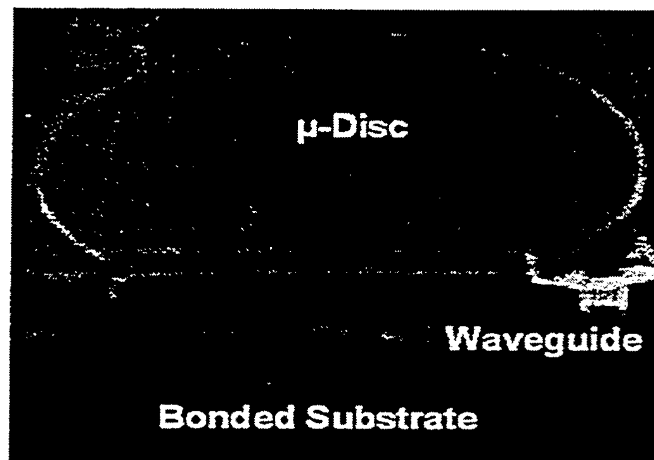

Figure 5.14 Cross-section SEM Image for Bonded µ-Disc Device

We can see that the µ-disc is strong enough to survive a cleaving [14]. Waveguides are bonded to the new substrate and bonding interfaces located on the top of the substrate.

5.7 Active μ-Disc

The contact has to be defined on the top of the ring/disc to pass a current. The n-contact is common for all devices and we used a standard electroplating solution to make an n- contact. [12].

The p-contact has to be defined on the top of the structure. We deposit SiN_x first to passivate the sample surface and create a current path. Thick photoresist was then spun on the sample to cover everything, including the discs. Etch-Back techniques were used to open a contact over the μ-disc area. We only etched samples in low-pressure oxygen plasma with periodic surface monitoring. Elevated areas have thinner photoresist layers and the time required to clean this area is less. We were able to self align open areas to the top of the disc.

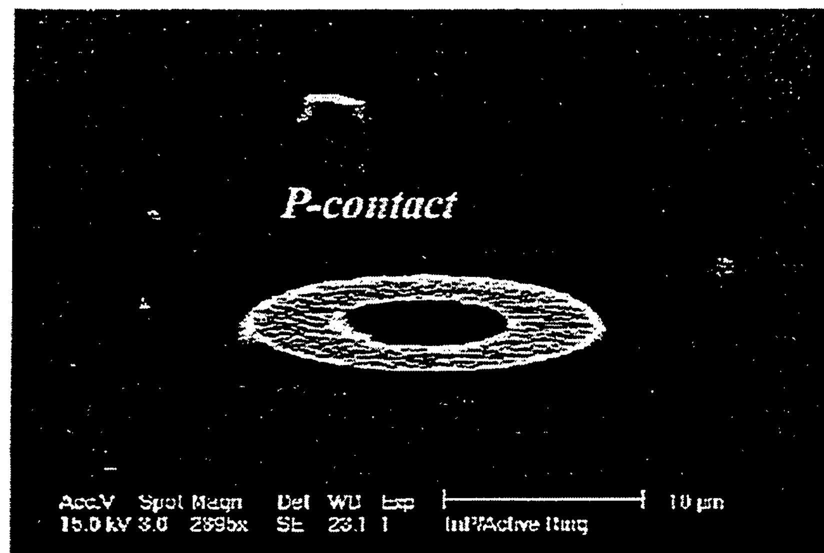

Figure 5.15 μ-Ring with P-contact on top, Fabricated by Using Self-alignment Technique

After P-contact definition, the transfer substrate was also lapped down and the sample was cleaved into 200-800 μm bars for optical testing using standard laser bar cleaving procedures. No AR coatings were deposited on this set of samples, which is evident in the data presented later. Finally the bars were mounted on copper blocks for testing as it was discussed in Chapter 4.

References

1.In Kim, D. Tishinin and P.D. Dapkus "Control of selective area growth and regrowth of InP on mesas by MOCVD using TBP"ICMOVPE IX, oral presentation.

2. Won-Jin Choi " Design and fabrication of novel InGaAs and al Ga InP quantum well lasers by MOCVD" Ph.D. Thesis dissertation 1999.

3.K. Uppal, D. Tishinin, I. Kim and P. D. Dapkus:" Study of 1.3μm tapered waveguide spot size transformers" JQE, Vol. 3 pp.975-980, 1997

4. D. Tishinin, P. D. Dapkus, A. E. Bond, I. Kim, C. K. Lin and J. o'Brien "Vertical resonant couplers with precise coupling efficiency control fabricated by wafer bonding" PTL Vol.11. pp.1003-1006, 1999

5 D. Tishinin, P. D. Dapkus, A. E. Bond, I. Kim, C. K. Lin and J. o'Brien "Vertical resonant couplers with precise coupling efficiency control fabricated by wafer bonding" PTL Vol.11. pp.1003-1006, 1999

6 Chao-Kun Lin, Sangwan Ryu, Won-Jin Choi, and P. D. Dapkus, "Wafer Bonded Bottom-Emitting 850 nm VCSEL's on GaP substrates", IEEE Photonics Technology Letters, August 1999.

7 B. Liu, A. Shakouri, P. Abraham, B. G. Kim, A. W. Jackson, and J. E. Bowers, "Fused vertical couplers," Appl. Phys. Lett. Vol 72, no. 21, pp 2637-2638 (1998).

8. B. Liu, A. Shakouri, P. Abraham, Y. J. Chiu, S. Zhang, and J. E. Bowers, "Fused InP-GaAs vertical coupler filters," IEEE Photon. Technol. Lett, vol. 11, pp 93-95, Jan. 1999

9. Fen, Lothian, Kuo, Hobson and Lopata " BCl3/N2 dry etching of InP, InGaAs and InAlAs" J. Vac Technol. B14(3) May 1996

10 Aaron Eugene Bond " Photonic and electronic Devices for high Performance Smart Pixels" Ph.D. Thesis dissertation 1999.

11. K Uppal, D. Tishinin and P. D. Dapkus: " Characterization of mixed quantum well structures" J. Apply. Physics 81(1) pp. 390-393 1997

12. A. Mathur and P. D. Dapkus: "Polarization insensitive strain quantum well medium for laser and optical amplifiers" Appl. Phys. Letters 61(24), 2845- 2847 (1992)

13. E.I. Chen, N. Holonyak, J.M. Ries:" Planar Disorder-Defined and Native-Oxide-Defined Photopumped AlAs-AlGaAs Superlattice Minidisk Lasers" Journal of Applied Physics, vol 79, issue 11, June 1996, pp.8204-

14. D. Tishinin, I. Kim, A.E. Bond, C. Lin, J. o'Brien, and P.D.Dapkus "Novel Fabrication Process for Vertical Resonant Coupler with Precise Coupling Efficiency Control" LEOS 98. oral presentation, Tuk5

Chapter 6

Conclusions and Future Research Direction

6.1 Conclusion

6.1.1 Semiconductor Optical Amplifier

In this work we have demonstrated, for the first time, polarization insensitive semiconductor optical amplifiers with an integrated mode transformer section [1]. Tensile and compressive quantum well gain was studied experimentally in devices with a tapered section. We showed that lateral tapering of the waveguide does not affect media gain characteristics.

The gain media with mixed quantum wells used in this study were grown by MOCVD. Tensile and compressive quantum wells were optimized separately to achieve polarization insensitive gain. A novel edge photoluminescence technique was used to calibrate quantum well spontaneous emission. Broad area devices made with this material show lasing in both the TE and TM modes. Device characteristics were studied and the design was optimized for threshold current density and polarization property of emitted light. The lowest threshold current density achieved was $235A/cm^2$ for three QW devices with compressive strain and $277A/\ cm^2$ for three quantum well devices with tensile strain. These results are comparable to the best results reported in the literature. Uniformity measurements done on broad area devices show no dark spots which verifies the uniformity of our material.

To implement low threshold devices, buried heterostructure lasers were fabricated. ECR dry etching was calibrated to give us uniform etching with vertical and smooth sidewalls. $CH_4/H_2/Ar$ was used to perform the etching. Effects of etching depth and regrown layer composition were studied. Low threshold devices with small leakage current were fabricated, as a result. We have demonstrated less than 12mA threshold current in BH devices [2].

The mode conversion section was modeled and experimentally demonstrated. Laterally tapered region added to the waveguide gives us a $10\text{-}15^0$ reduction in the far field angle. Near field measurements show a 1.5 times increase in mode size, which corresponds to the reduction in output beam divergence we observe in far field. The output beam profile was single mode in the tapered structures with vertical walls.

Butt coupling to a single mode (9μm diameter) cleaved fiber was improved as a result of this mode transformation. Coupling losses were reduced by 3-4 dB, with reduced alignment tolerance by more than 4μm in both directions. Taper losses were measured to be around 1-2 dB. The tapered section gives us 2-3dB improvement even after we subtract additional losses in the tapered section.

Traveling wave semiconductor optical amplifiers were fabricated by applying antireflection coatings to a dual-polarization laser design. A low reflectivity coating obtained with nonstoichiometric SiO_x was calibrated for index and thickness. Residual reflectivity measured on studied samples proved to be less than 10^{-5}. Chip gain was measured to be more than 18 dB with less than 1 dB of polarization sensitivity at all pumping currents. High saturation powers of 10dBm were measured for both TE and TM input light polarizations. The taper section does not affect the polarization properties

in our design of the SOA. Gain and saturation power in the device with an integrated mode transformer section is comparable to the typical data for a BH device, so we can say that our tapered region does not affect polarization gain and saturation properties in a traveling wave amplifier.

6.1.2 μ-Resonator Devices

In this project novel μ-resonator devices were implemented in the GaAs and InP material systems. Novel vertical coupling to the μ-disc (ring) was proposed and implemented. μ-Discs positioned on top of input/output waveguides gives us precise control over coupling strength [3]. MOCVD growth was used to define coupling separation. Numerical estimation of this design was performed to optimize the coupling and quality factor. Experimental demonstration of the proposed device has been done.

Numerical simulation was done by direct solutions to Maxwell's equations in two and three-dimensional cases. Effects of waveguide design and separation distance were studied to optimize the vertical coupler [4]. We designed single mode waveguides with predictable coupling to a resonator element, located on top of the waveguide. We can control resonator bandwidth by controlling input/output coupling, when modifying the quality factor.

Wafer bonding was used to define a 2-layer structure with precise vertical coupling between the vertically integrated waveguides and resonator elements. Wafer bonding was calibrated to give good mechanical strength and good optical and electrical properties at the same time. Laser devices made using wafer bonding show 4-5 Ohms resistance and no increase in threshold current compared to as grown devices. Optimal

temperatures were chosen to be 400^0C for InP wafer and 750^0C for GaAs wafers. Good bonding uniformity was achieved on samples with 1 cm^2 area.

Chlorine based ECR etching was calibrated to provide uniform etching suitable for laser and waveguide formation. BCl_3 used in this set of samples gives very clean bottom surface with smooth slightly undercut sidewalls. A clean bottom surface is very important for improving micro resonator quality factor, because it is located under the micro-disc and within resonator mode field. The same etching recipe was used for disc/ring definition. Sidewall roughness also restricts the quality factor of the resonator. In this study, we used AlO_x to reduce interaction between evanescent light and edge defects. The Q factor was improved form 700-800 to about 1500 by using aluminum oxide.

Samples made on InP wafers show low Q-factor, but we can add an active gain to compensate for radiation and scattering losses. We have shown that by pumping the μ-disc we can compensate for losses and improve cavity properties even for devices with some sidewall defects.

6.2 Future Research Direction

Amplifiers and micro resonators are potential building blocks for future integrated optical circuits. Their small dimensions and wavelength selectivity make them extremely attractive for photonic devices. We can build complete WDM systems using a combination of wavelength selective filters (μ-ring) and optical amplifiers. Resonant elements can also be used as a building block for creating higher odder filters [5,6].

Wavelength separation between channels for such system is defined by current international DWDM standards, which is now 2.5Gbit and 0.3nm per channel. To meet

these challenges the quality factor for a resonator must be increased, preferably to 10000. This should not limit the bandwidth but it will provide necessary selectivity. We can do this several different ways.

First we can improve edge smoothness. Already passive devices (no input/output load) have been demonstrated with record Q-factors of up to 6000 [1]. Unselective wet etching may be used to reduce edge roughness. Another approach is to a introduce second step during dry ECR etching. Very low power gives us uniform, smoothing etching [7].

Secondly, active gain can be introduced to compensate for device losses. It was already shown in chapter 4 that active devices even with a lossy resonator cavity can show energy transformation in and out of the cavity. The same principle may be used to push up the quality factor by precise gain adjustments. The problem with our current design is pumping uniformity. The air gap located under the resonator prevents uniform current distribution and makes it virtually impossible to achieve reasonable gain near the outer edge of the disc between waveguides, where the optical mode is the strongest. New waveguide designs could be used to remove this air gap region. Fortunately, in our device design top and bottom layers are processed independently and we can easily switch to the buried heterostructure waveguides, by doing thick selective overgrowth before bonding. Uniform resonator pumping lets us to utilize material gain to improve single unit performance.

References

1. D. Tishinin, K. Uppal, I. Kim and P. D. Dapkus, "1.3μm Polarization Insensitive Amplifiers with Integrated Mode Transformers" PTL, vol. 9,No 10, October 1997 pp.1337-1339

2. D. Tishinin, K. Uppal, I. Kim and P. D. Dapkus, "1.3μm Polarization Insensitive Amplifiers with Integrated Mode Transformers" LEOS 98, oral presentation MP1

3. D. Tishinin, P. D. Dapkus, A. E. Bond, I. Kim, C. K. Lin and J. o'Brien "Vertical resonant couplers with precise coupling efficiency control fabricated by wafer bonding" PTL Vol.11. pp.1003-1006, 1999

4. D. Tishinin, I. Kim, A.E. Bond, C. Lin, J. o'Brien, and P.D.Dapkus "Novel Fabrication Process for Vertical Resonant Coupler with Precise Coupling Efficiency Control" LEOS 98. oral presentation, Tuk5

5. Little, Haus, Foresi, Kamerling and Ippen :"Wavelength switching and routing using absorption and resonance" IEE PTL, vol. 10, No 6, July 1998

6. Fen, Lothian, Kuo, Hobson and Lopata " BCl3/N2 dry etching of InP, InGaAs and InAlAs" J. Vac Technol. B14(3) May 1996

Appendix A

ECR Calibration

A.1 InP Etching

The electron cyclotron resonance etching system is very popular for dry etching both because of its manageable etching rate and the resulting smooth surfaces, which are suitable for regrowth. In this project we have used a commercial ECR made by "Plasmaquest".

The general design is shown in the picture below:

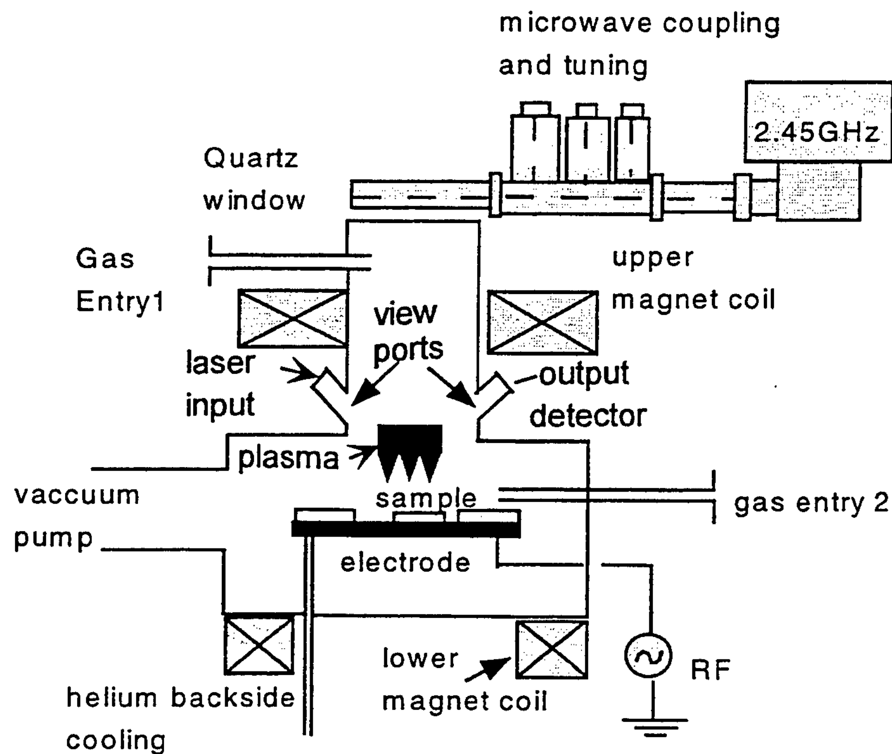

Figure A.1 Schematic Drawing for an ECR System

The system has eight gas lines connected to it. We have tried two different gas combinations: $CH_4/H_2/Ar$ and BCL_3/Ar. Both of them are generally suitable for InP and GaAs material systems, but for this set of experiments, which were done on long wavelength material, we chose the methane-based system. This was because of its applicability at room temperature and ability to provide us almost vertical walls under the right etching conditions.

During the etching we used both a DC bias and microwave 13.56MHz power coupled into the chamber, surrounded by two magnets to collimate the plasma. We used a 185A current in the upper magnet and 125A in the lower magnet, producing high-density plasma. Backside helium was used to stabilize the sample temperature and to prevent the sample from overheating, an effect, which could cause etch rate variations. Sometimes vacuum grease was used to improve thermal contact between the sample and loading chuck. In any case methane based etching was done without additional heating and the sample temperature was kept below 50°C.

We used $CH_4/H_2/Ar$ for this set of experiments because it gives us vertical walls and our etching depth is below 1 micron. Chlorine based etchants (BCL_3) are not good candidates due to their high etch rate and over-cut profile. The low etching rate for the methane based system can be attributed to low plasma generation efficiency and short lifetime due to gas phase reactions [1]. A hydrocarbon-based etchant also has the advantage of being non-corrosive and nontoxic compared to chlorine-based chemistry. In this $CH_4/H_2/Ar$ combination, methane reacts with group III components, creating volatile products and hydrogen combines with group V materials, removing them from the surface.

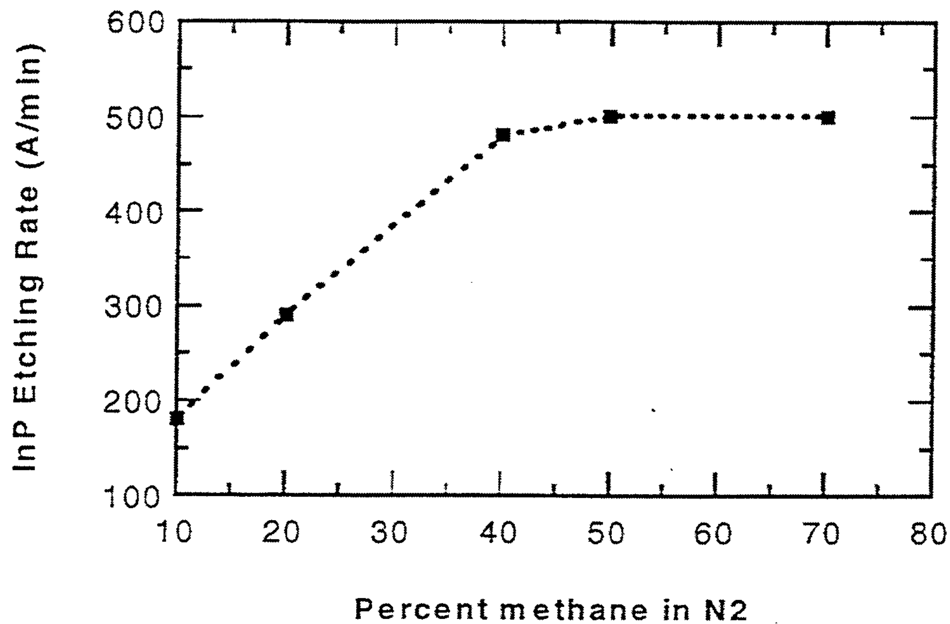

Figure A.2 Etching Rate vs. Methane/N2 Ratio

These hydrocarbons deposit on less reactive surfaces like SiN_x (used as a mask), the ECR chamber walls and even on the etched sidewalls of the sample. This can improve mask/semiconductor selectivity under the proper conditions and also provides vertical walls. In contrast, etching with chlorine-based etchants gives over-cut sidewalls, which are not suitable for tapered waveguide definition. A small quantity of Argon was added to reduce the deposition rate and also to stabilize the plasma at low microwave power (this is desirable to reduce surface damage). Microwave power is also an important factor in etching calibration. High bias (corresponding to high power) improves etching directionality but at the same time it increases the surface damage.

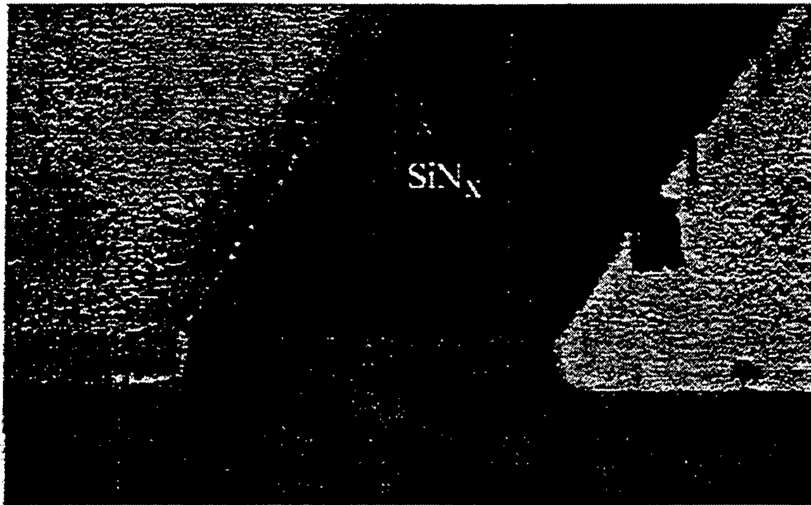

Figure A.3 ECR Etched Surface 100V Self Induced DC Bias with Polymer Already Removed

At small bias $CH_4/H_2/Ar$ etching gives extremely low damage depth (about 20Å) [2], but etching is very slow, hence we have problems obtaining vertical sidewalls. However, it can be used as a second step, after the structure is already defined. We remove a few nanometers of material without changing the waveguide profile. This will generate nearly undamaged surfaces [3]. Regrowth done on this kind of treated bottom surface shows that we can cover it and get a good growth very quickly.

We used $CH_4/H_2/Ar$ (8/17/10sccm.) at a working pressure of 2 mTorr with background pressure in the chamber around 10.6-10.7 Torr. We obtained a 500Å/min etch rate with vertical walls. We get some polymer deposition on the SiN_x mask region, but it is easily removed with about 2 minutes of immersion in O_2 plasma for every 10 minutes of ECR etching.

A.2 Etching with Chlorine

Chlorine-based ECR etching was used for both material systems [9]. GaAs devices were etched at room temperature, while for InP waveguides we raised the temperature to 150°C. BCl_3 used for InP etching gives us a clean profile with slight undercutting and a cross section that looks similar to chemically etched devices. We used 1kW of microwave power and studied the effects of bias. Low bias and a correspondingly low RF power create a great deal of deposition on the sample surface, as shown in the following figure:

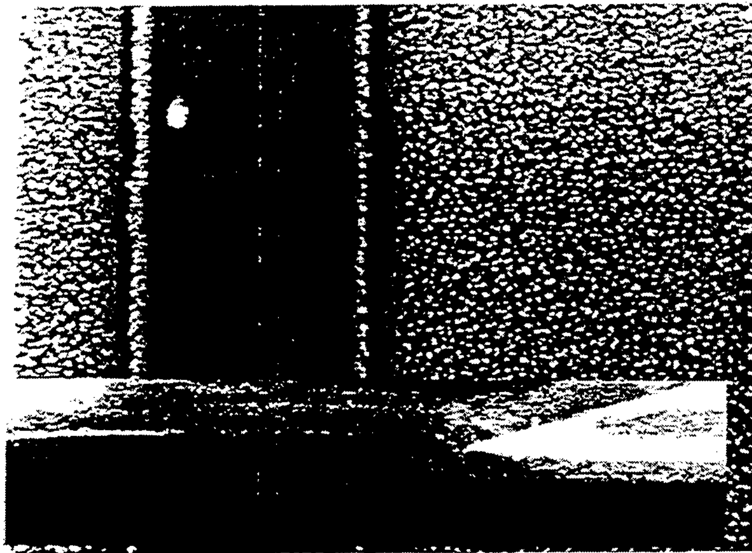

Figure A.4 Top View and Cross-Section on the Sample With Polymer Like Deposition

A bias of more than 50 volts always results in very clean etching without any deposition whatsoever. The bottom surface is usually very clean and smooth, which is very

important for a waveguide with a very thin top cladding layer. A Rough bottom surface located near the top of waveguide would result in increased scattering losses.

Different gases can be added to BCl_3 to modify etching profiles. We typically use argon as an additional gas, which stabilizes the plasma. Profiles obtained by the BCl_3/Ar combination gas etching is presented below.

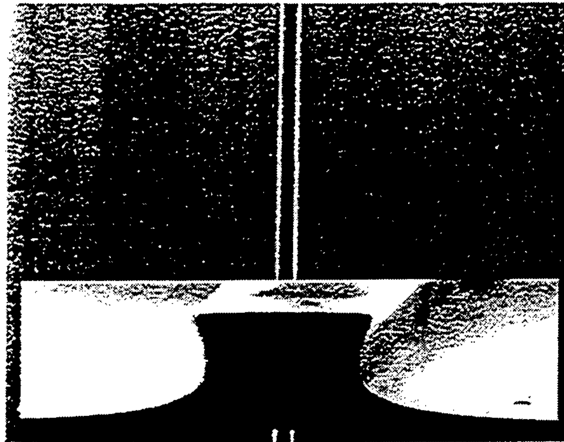

Figure A.5 InP Sample Etched in $BCl_3$and Ar Gas Combination

Oxygen added to a gas mixture facilitates the generation of vertical walls and keeps the bottom field clear, as we can see in the next figure.

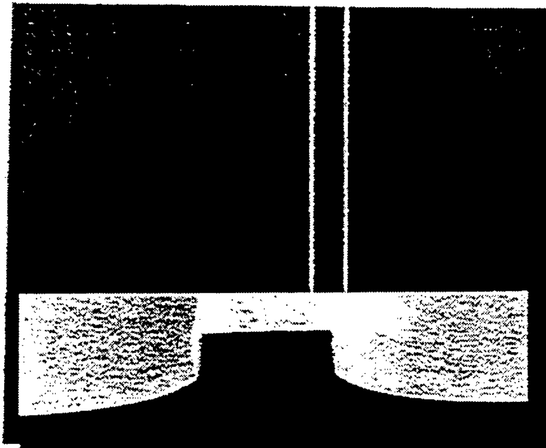

Figure A.6 InP Sample Etched with BCl_3 and O_2 Gas Combination

Optical monitoring [10] was used to determine the etching end-point.

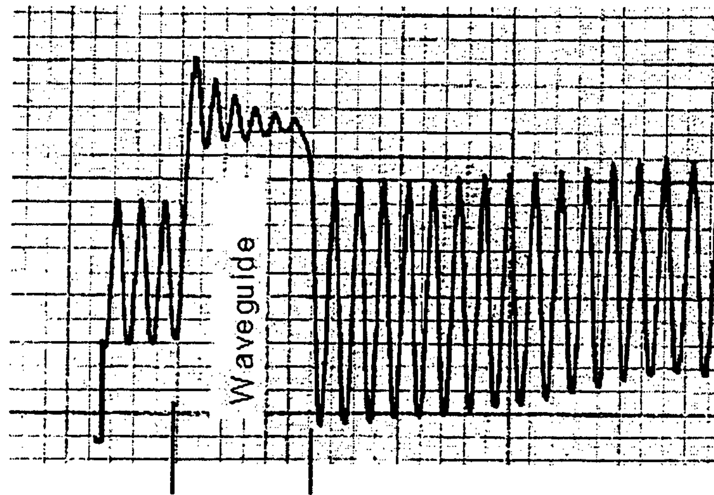

Figure A.7 Reflectivity Monitoring Data for GaAs Waveguide

This reflectivity data was compared to calculated reflectivity, presented in the next Figure:

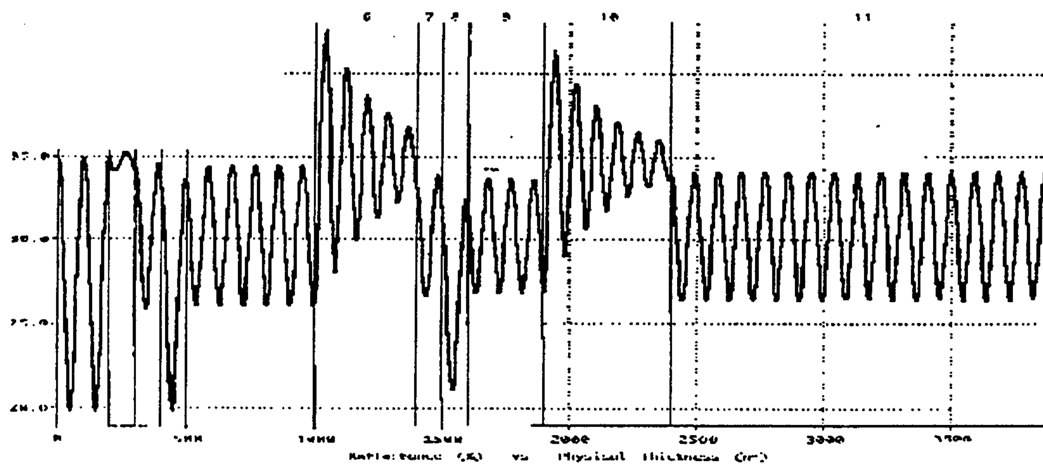

Figure A.8 Calculated Reflectivity vs. Etching Depth

We can see from this that it is possible to stop etching precisely at any point if we know the material structure.

Chlorine and methane based etching is applicable to all III-V semiconductors. We can get smooth bottom surfaces and strained sidewalls with the right etching conditions. The methane/hydrogen ration is very important for uniformity and quality of room temperature etching.

Reference:

1 S.Adachi, H.Kawaguchi and G.Iwane, J.Materials Science, 16, (1981) 2449

2 D.T.C.Huo, M.F.Yan, J.D.Wynn and D.P.Wilt, J.Electrochem. Soc., 136, (1989) 1828

3 S.J.Pearton, J.W.Lee, E.S.Lambers, C.R.Abernathy, F.Ren, W.S.Hobson and R.J.Shul, J.Electrochem. Soc., 143, (1996) 752

Bibliography

Chapter 1

J. P. Hirtz, M.Razeghi, M.Bonnet and J.P.Duchemin, in GaInAsP Alloy Semiconductors, edited by T.P Pearsall, Wiley, 1982

V. Swaminathan and A.T.Macrander, Materials Aspects of GaAs and InP Based Structures, Prentice-Hall, 1991

S. Adachi, "Material parameters of InGaAsP and related binaries,"J. Appl. Phys. ,vol. 53, number 12, pp 8775-8792, Dec. 1982

O.Madelung, Semiconductors - Group IV Elements and III-V Compounds, Springer-Verlag, 1991

Atul Mathur, Ph.D. Dissertation, University of Southern California, 1995

Atul Mathur, Julian Osinski, Piotr Grodzinski and P.D.Dapkus, "Comparative Study of Low-Threshold 1.3μm Strained and Lattice-Matched Quantum-Well Lasers," IEEE Phot. Tech. Lett., vol. 5, no. 7, pp. 753-755, July 1993

Brakett "DDWM network, principals and application"IEEE J. Select. Areas Communication, vol 9,pp. 948-964 1990

Midwinter , "Photonics in swithching, background and components" Academic Press, Inc., San Diego, CA 1993

T.Miya, Y.Terunuma, T.Hosaka and T.Miyoshita, Eleec. Lett. 15, (1979) 106

A.Sugimura, K.Daikoku, N.Imoto and T.Miya, IEEE J.Quan. Elec., 16, (1980) 215

G.P.Agrawal and N.K.Dutta, "Long Wavelength Semiconductor Lasers", Van Nostrand Reinhold, 1993

S. Dubovitsky, A. Mathur, W. Steier and P. D. Dapkus: "Gain Saturation Property of a Polarization Insensitive Semiconductor Amplifier Implemented with Tensile and Compressive Strain Quantum Wells." IEEE Phot. Tech. Letters 6, 176-178 (1994)

D. Tishinin, K. Uppal, I. Kim and P. D. Dapkus, "1.3μm Polarization Insensitive Amplifiers with Integrated Mode Transformers" PTL, vol. 9,No 10, October 1997 pp.1337-1339

S. Dubovitsky Ph.D dissertation, USC 1994

L.C.Su, I.H.Ho and G.B.Stringfellow, J.Cryst. Growth, 146, (1995) 558

H. Zhao, M.H. MacDougal, K. Uppal, Y. Cheng, G.M. Yang, and P.D. Dapkus, Journal of Quantum Electronics 1, (1994) 196

J.Diaz, I.Eliashevich, K.Mobarhan, E.Kolev, L.J.Wang, D.Z.Garbuzov and M.Razeghi, IEEE Photon. Tech. Lett., 6, (1994) 132

G.Zhang, J.Nappi, H.Asonen and M.Pessa, IEEE Photon. Tech. Lett., 6, (1994)1

J.Diaz, I.Eliashevich, X.He, H.Yi, L.Wang, E.Kolev, D.Garbuzov and M.Razeghi, Appl. Phys. Lett., 65, (1994) 1004

H.Tanaka, Electron.Lett., 29, (1993) 1611

A.Mathur, J.S.Osinski, P.Grodzinski and P.D.Dapkus, IEEE Photon. Tech. Lett., 5, (1993) 753

D.Coblentz, T.Tanbun-Ek, R.A.Logan, A.M.Sergent, S.N.G.Chu and P.S.Davisson, Appl. Phys. Lett., 59, (1991) 405

E.S.Koteles, D.A.Owens, D.C.Bertolet, J.Hsu and K.M.Lau, Surface Science 228, (1990) 314

R.Bhat, Semicond. Sci. Technol., pp. 984-993, 8, 1993

D. Rafizadeh, J.P.Zhang, S.C. Hagness, A. Taflone, K.A.Stair, and S.T.Ho: "Waveguide Coupled AlGaAs/GaAs Microcavity Ring an Disk Resonators with High Finesse and 21.6-nm Free spectral Range" Optical Letters vol. 22, No16, August 1997, pp.1244-1246

J. Foresi,B. Little, G, Steinmeyer, E. Thoen, S.Chu, H. Haus E. Ippen, L. Kimerling, and W. Greene: "Si/SiO_2 Micro-Ring Resonator Optical Add/Drop Filters"LEOS1996 CPD22-2

B.E. Little, S.T. Chu, H.A.Haus, J. Forresi, and J.P.Laine: "Microring Resonator Channel Dropping Filters" Journal of Lightwave Technology, vol 15 no 6, June 1997, pp.998-1005

S.T. Chu, J. Forresi, and J.P.Laine and B.E. Little "Wavelength Trimming of a μ-Resonator filter be means of a UV sensitive polymer overlay" PLT, vol 7 1998 pp 484-487

Chapter 2

Kushant Uppal PhD Dissertation University of Southern California 1997

J.Downes and D.A.Faux, J. Appl. Phys. 77, (1995) 2444

K. Uppal, D. Tishinin, I. Kim and P. D. Dapkus:" Study of 1.3μm tapered waveguide spot size transformers" JQE, Vol. 3 pp.975-980, 1997

T.L.Koch, U.Koren, G.Eisenstein, M.G.Young, M.Oron, C.R.Giles and B.I.Miller, IEEE Photon. Tech. Lett. 2, (1990) 88

C.Constantine, C.Barratt, S.J.Pearton, F.Ren and J.R.Lothian, Electron. Lett. 28, (1992) 1750

In Kim, D. Tishinin and P.D. Dapkus "Control of selective area growth and regrowth of InP on mesas by MOCVD using TBP"ICMOVPE IX, oral presentation.

K. Uppal, D. Tishinin and P. D. Dapkus: "1.3μm polarization insensitive tapered waveguide mode conversion structures with mixed quantum well active regions" LEOS 1996, oral presentation

T.Kambayash, C.Kitahara and K.Iga, Jpn. J.Appl. Phys., 19, (1980) 79

Atul Mathur, Ph.D. Dissertation, University of Southern California, 1995

Robert J.Lang, Anders G.Larsson and Jeffrey G.Cody, "Lateral modes of broad area semiconductor lasers:theory and experiment", IEEE J. Quant. Elec., vol. 27, no. 3, 1991

Siegman "Lasers" University Science book

G.P.Agrawal and N.K.Dutta, "Long Wavelength Semiconductor Lasers", Van Nostrand Reinhold, 1993

S.Kitamura, K.Komatsu and M.Kitamura, IEEE Photon. Tech. Lett., vol. 6, no. 2, pp 173-175, Feb. 1994

M.Joma, H.Horikawa, C.Q.Xu, K.Yamada, Y.Katoh and T.Kamijoh, Appl. Phys. Lett., vol. 62, no.2, pp 121-122, Jan. 1993

K.Magari, Mokamoto, H.Yasaka, K.Sato, Y.Noguchi and O.Mikami, IEEE Photn. Tech. Lett., vol. 2, no.8, pp 556-558, Aug. 1990

Chapter 3

K. Uppal, D. Tishinin, I. Kim and P. D. Dapkus:" Study of 1.3μm tapered waveguide spot size transformers" JQE, Vol. 3 pp.975-980, 1997

K. Uppal, D. Tishinin and P. D. Dapkus: "1.3μm polarization insensitive tapered waveguide mode conversion structures with mixed quantum well active regions" LEOS 1996, oral presentation

H.Okamoto, Y.Suzaki, Y.Tohmori, M.Okamoto, Y.Kondo, Y.Kadota, M.Yamammoto, K.Kishi, Y.Sakai, M.Wada, M.Nakao and Y.Itaya, Electron. Lett. 32, (1996) 1099

H.Kobayashi, M.Ekawa, N.Okazaki, O.Aoki, S.Ogita and H.Soda, IEEE Photon. Tech. Lett. 6, (1994) 1080

A.Kasukawa, N.Iwai, N.Yamanaka, Y.Nakahira and N.Yokouchi, Electron. Lett. 32, (1996) 1294

R.Zengerle, B.Jacobs, W. Weiershausen, K.Faltin and A.Kunz, J.Lightwave Tech., 14, (1996) 448

B.Mersali, H.J.Bruckner, M.Feuillade, S.Sainson, A.Ougazzaden and A.Carenco, J.Lightwave Tech., 14, (1996) 1865

P.Doussiere, P.Garabedian, C.Graver, D.Bonnevie, T.Fillion, E.Derouin, M.Monnot, J.G.Provost, D.Leclerc and M.Klenk, IEEE Photon. Tech. Lett. 6, (1994) 170

D. Tishinin, K. Uppal, I. Kim and P. D. Dapkus, "1.3μm Polarization Insensitive Amplifiers with Integrated Mode Transformers" LEOS 98, oral presentation MP1

H.C.Casey, M.B.Panish and J.L.Merz, J.Appl. Phys., 44, (1973) 5470

A. Mathur and P. D. Dapkus : "Polarization insensitive strain quantum well medium for laser and optical amplifiers" Appl. Phys. Letters 61(24), 2845- 2847 (1992)

K Uppal, D. Tishinin and P. D. Dapkus: " Characterization of mixed quantum well structures" J. Apply. Physics 81(1) pp. 390-393 1997

R. Zengerle and W. Weiershausen: " Tapered two-layer InGaAs/InP waveguides for highly efficient chip coupling to single mode fibers" Optics Communications 115, 453-460 (1995)

Kelly, Lealman , Rivers, Perry and Silver : "Polarization insensitive, 25 db gain SOA withot antireflection coating. " Electronic Letters, Vol. 32, pp. 1835-1837, 1996

Gallant, Tilton, Bossert and Dente :"optimized single-layer antireflection coating for semiconductor laser" IEEE PTL, vol 9, pp.300-3002, 1997

Ramadas, Garmire, Ghatak, shenoy " Analysis of absorbing and leaking waveguides: a novel method", Optic Letters, vol 14, pp. 376-378, 1989

Fan, Riantm Verdiell and Dagenias: " Real-time insuty monitoring of Ar coating for SOA by ellipsomtry", IEEE PTL, vol.4, no9, September 1992

D. Zhu "Novel optical switches based on TW SAO" dissertation, 1997

S. Dubovitsky, A. Mathur, W. Steier and P. D. Dapkus: "Gain Saturation Property of a Polarization Insensitive Semiconductor Amplifier Implemented with Tensile and Compressive Strain Quantum Wells." IEEE Phot. Tech. Letters 6, 176-178 (1994)

A. Mathur and P. D. Dapkus : "Polarization insensitive strain quantum well medium for laser and optical amplifiers" Appl. Phys. Letters 61(24), 2845- 2847 (1992)

Chapter 4

D. Rafizadeh, J.P.Zhang, S.C. Hagness, A. Taflone, K.A.Stair, and S.T.Ho: "Waveguide Coupled AlGaAs/GaAs Microcavity Ring an Disk Resonators with High Finesse and 21.6-nm Free spectral Range" Optical Letters vol. 22, No16, August 1997, pp.1244-1246

J. Foresi, B. Little, G, Steinmeyer, E. Thoen, S.Chu, H. Haus E. Ippen, L. Kimerling, and W. Greene: "Si/SiO_2 Micro-Ring Resonator Optical Add/Drop Filters"LEOS1996 CPD22-2

P. D. Dapkus, D. Tishinin, and In Kim "Active and Passive Microdiscs Coupled to Waveguides for WDM Applications" LEOS 99

B.E. Little, S.T. Chu, H.A.Haus, J. Forresi, and J.P.Laine: "Microring Resonator Channel Dropping Filters" Journal of Lightwave Technology, vol 15 no 6, June 1997, pp.998-1005

D. V. Tishinin, I. Kim, A. E. Bond, C.K. Lin, and P. D. Dapkus, "Novel fabrication process for vertical resonant coupler with precise coupling efficiency control," LEOS 11th Annual Meeting, (Institute of Electrical and Electronics Engineers, New York, 1998) Orlando, FL, December, 1998; paper TuK5.

B.E. Little, S.T. Chu, H.A.Haus, J. Forresi, and J.P.Laine: "Microring Resonator Channel Dropping Filters" Journal of Lightwave Technology, vol 15 no 6, June 1997, pp.998-1005

D. Tishinin, P. D. Dapkus, A. E. Bond, I. Kim, C. K. Lin and J. o'Brien "Vertical resonant couplers with precise coupling efficiency control fabricated by wafer bonding" PTL Vol.11. pp.1003-1006, 1999

Chu and Chaundhuri "A finite-difference time-domain method for design and analysis of guided-wave optical structures" J. Lighwave Tech. Vol. 7, pp. 2033-2038, 1989

E.I. Chen, N. Holonyak, J.M. Ries: "Planar Disorder-Defined and Native-Oxide-Defined Photopumped AlAs-AlGaAs Superlattice Minidisk Lasers" Journal of Applied Physics, vol 79, issue 11, June 1996, pp.8204-8209

Little, Haus, Foresi, Kamerling and Ippen:"Wavelength switching and routing using absorption and resonance" IEE PTL, vol. 10, No 6, July 1998

Chapter 5

In Kim, D. Tishinin and P.D. Dapkus "Control of selective area growth and regrowth of InP on mesas by MOCVD using TBP"ICMOVPE IX, oral presentation.

Won-Jin Choi " Design and fabrication of novel InGaAs and al Ga InP quantum well lasers by MOCVD" Ph.D. Thesis dissertation 1999.

K. Uppal, D. Tishinin, I. Kim and P. D. Dapkus:" Study of 1.3μm tapered waveguide spot size transformers" JQE, Vol. 3 pp.975-980, 1997

D. Tishinin, P. D. Dapkus, A. E. Bond, I. Kim, C. K. Lin and J. o'Brien "Vertical resonant couplers with precise coupling efficiency control fabricated by wafer bonding" PTL Vol.11. pp.1003-1006, 1999

D. Tishinin, P. D. Dapkus, A. E. Bond, I. Kim, C. K. Lin and J. o'Brien "Vertical resonant couplers with precise coupling efficiency control fabricated by wafer bonding" PTL Vol.11. pp.1003-1006, 1999

Chao-Kun Lin, Sangwan Ryu, Won-Jin Choi, and P. D. Dapkus, "Wafer Bonded Bottom-Emitting 850 nm VCSEL's on GaP substrates", IEEE Photonics Technology Letters, August 1999.

B. Liu, A. Shakouri, P. Abraham, B. G. Kim, A. W. Jackson, and J. E. Bowers, "Fused vertical couplers," Appl. Phys. Lett. Vol 72, no. 21, pp 2637-2638 (1998).

B. Liu, A. Shakouri, P. Abraham, Y. J. Chiu, S. Zhang, and J. E. Bowers, "Fused InP-GaAs vertical coupler filters," IEEE Photon. Technol. Lett, vol. 11, pp 93-95, Jan. 1999

Fen, Lothian, Kuo, Hobson and Lopata " BCl3/N2 dry etching of InP, InGaAs and InAlAs" J. Vac Technol. B14(3) May 1996

Aaron Eugene Bond " Photonic and electronic Devices for high Performance Smart Pixels" Ph.D. Thesis dissertation 1999.

K Uppal, D. Tishinin and P. D. Dapkus: " Characterization of mixed quantum well structures" J. Apply. Physics 81(1) pp. 390-393 1997

A. Mathur and P. D. Dapkus: "Polarization insensitive strain quantum well medium for laser and optical amplifiers" Appl. Phys. Letters 61(24), 2845- 2847 (1992)

E.I. Chen, N. Holonyak, J.M. Ries:" Planar Disorder-Defined and Native-Oxide-Defined Photopumped AlAs-AlGaAs Superlattice Minidisk Lasers" Journal of Applied Physics, vol 79, issue 11, June 1996, pp.8204-

D. Tishinin, I. Kim, A.E. Bond, C. Lin, J. o'Brien, and P.D.Dapkus "Novel Fabrication Process for Vertical Resonant Coupler with Precise Coupling Efficiency Control" LEOS 98. oral presentation, Tuk5

Chapter 6

D. Tishinin, K. Uppal, I. Kim and P. D. Dapkus, "1.3μm Polarization Insensitive Amplifiers with Integrated Mode Transformers" PTL, vol. 9,No 10, October 1997 pp.1337-1339

D. Tishinin, K. Uppal, I. Kim and P. D. Dapkus, "1.3μm Polarization Insensitive Amplifiers with Integrated Mode Transformers" LEOS 98, oral presentation MP1

D. Tishinin, P. D. Dapkus, A. E. Bond, I. Kim, C. K. Lin and J. o'Brien "Vertical resonant couplers with precise coupling efficiency control fabricated by wafer bonding" PTL Vol.11. pp.1003-1006, 1999

D. Tishinin, I. Kim, A.E. Bond, C. Lin, J. o'Brien, and P.D.Dapkus "Novel Fabrication Process for Vertical Resonant Coupler with Precise Coupling Efficiency Control" LEOS 98. oral presentation, Tuk5

Little, Haus, Foresi, Kamerling and Ippen :"Wavelength switching and routing using absorption and resonance" IEE PTL, vol. 10, No 6, July 1998

Fen, Lothian, Kuo, Hobson and Lopata " BCl3/N2 dry etching of InP, InGaAs and InAlAs" J. Vac Technol. B14(3) May 1996

Appendix A

S.Adachi, H.Kawaguchi and G.Iwane, J.Materials Science, 16, (1981) 2449

D.T.C.Huo, M.F.Yan, J.D.Wynn and D.P.Wilt, J.Electrochem. Soc., 136, (1989) 1828

S.J.Pearton, J.W.Lee, E.S.Lambers, C.R.Abernathy, F.Ren, W.S.Hobson and R.J.Shul, J.Electrochem. Soc., 143, (1996) 752